PATTERNED FABRICATION OF POLYANILINE NANOSTRUCTURES FOR ULTRASENSITIVE BIOMOLECULE DETECTION

by

Jiyong Huang

B.S. in Pharmaceutical Engineering, Beijing University of Chemical Technology, 2005

M.S. in Pharmaceutical Engineering, Beijing University of Chemical Technology, 2008

Submitted to the Graduate Faculty of

The Swanson School of Engineering in partial fulfillment

of the requirements for the degree of

Doctor of Philosophy

University of Pittsburgh

2014

UNIVERSITY OF PITTSBURGH

SWANSON SCHOOL OF ENGINEERING

This dissertation was presented

by

Jiyong Huang

It was defended on

November 22, 2013

and approved by

William Stanchina, Ph.D., Professor, Department of Electrical and Computer Engineering

Hong Koo Kim, Ph.D., Professor, Department of Electrical and Computer Engineering

Zhihong Mao, Ph.D., Associate Professor, Department of Electrical and Computer Engineering

Xinyan Tracy Cui, Ph.D., Associate Professor, Department of Bioengineering

Dissertation Director: Minhee Yun, Ph.D., Associate professor, Department of Electrical and Computer Engineering

PATTERNED FABRICATION OF POLYANILINE NANOSTRUCTURES FOR ULTRASENSITIVE BIOMOLECULE DETECTION

Jiyong Huang, Ph.D.

University of Pittsburgh, 2014

With more number of individuals becoming health conscious, the use of biosensors for medical diagnosis is rapidly growing. So far, many efforts have been made to meet this increasing demand. This work presents several routes to improve the biosensors performances and builds a sophisticated platform for sensing application.

Single polypyrrole nanowire-based sensors were fabricated using a one-step electrochemical deposition method. A shadow mask was introduced to protect the biosensors from O_2 plasma for the microfluidics integration. The results of nanowire resistance and fluorescence intensity indicated that the shadow mask played a key role in protecting the biosensor. The microfluidic aptasensors were consequently developed. The sensor demonstrated excellent specificity and sensitivity with faster response and rapid stabilization times.

High yield polyaniline 1D nanowires and 2D nanobelts were fabricated by combining nanofabrication techniques and a chemical synthesis method. The PANI patterns possess good uniformity in morphology and electrical properties. The biosensors were found very sensitive to BNP targets, showing a response ~17% for 100 fg/mL BNP and a wide sensing range from 25 fg/mL to 5 pg/mL. Despite the reduced sensitivity compared to that in PBS, distinguishable changes in the FET sensors were observed over a range from 100 fg/mL to 5 pg/mL in serum. Significantly, the investigation about the Debye length opened an approach for further sensing

performance improvement. Within the sub-threshold regime of the NWs, the sensor responses exhibited about 4 times greater than that in their linear region.

Studies concentrated on the 2D PANI nanobelts revealed that they have similar rough surface and FET behavior to PANI-NWs. This suggested that the 2D PANI nanobelts would have comparable performances to 1D PANI-NWs as biosensors. A biosensor system based on the PNAI nanobelts was developed. The biosensors exhibited a good specificity and showed a linear range for BNP in buffer from 50 to 200 pg/mL. The demonstration of detecting BNP levels in human serum further confirmed that the sensor is capable of monitoring BNP in real samples. Those findings suggested that this biosensor system has a great potential for clinical use in future.

TABLE OF CONTENTS

LIST OF TABLES

LIST OF FIGURES

PREFACE

This Ph.D. dissertation contains the result of research undertaken at the Electrical and Computer Engineering in the University of Pittsburgh. These years at PITT have been a challenging journey, with both ups and downs. Fortunately, I was not alone on this road, but accompanied by professors, colleagues, families, and friends who are always willing to encourage, help, and motivate me. For this, I would like to kindly thank them.

I am sincerely thankful to Professor Minhee Yun at University of Pittsburgh for the opportunity to perform research at the department of electrical and computer engineering. With Professor Yun as an advisor, I had his support to work on many stimulating research projects. I want to thank committee members Prof. William Stanchina, Prof. Xinyan Cui, Prof. Zhihong Mao, and Prof. Hongkoo Kim for their time as well as invaluable comments and suggestions. Special thanks go to all the people who have worked with me over the years: Dave Sanchez, Yushi Hu, Dave Perello, Yiwen Xu, Innam Lee, Raymond Kovacs, Raghav Khanna. I sincerely appreciate their generous help and support.

Thanks and love to my parent, and my sisters, for their encouragement and support. Thanks to my parent-in-law and all my other relatives. I especially want to thank my wife, Lin, for always giving me the most needed warmth and comfort.

1.0 INTRODUCTION

Biosensors are biomolecular analytical devices that consist of biological recognition elements in direct contact with signal transducing elements. Such configuration enables the rapid and convenient conversion of the biological recognition events to detectable signals.[1] With the discovery of novel materials and the development of advanced and exquisite micro-/nano-fabrication tools, such as nanoimprint lithography, electron beam lithography, focused ion beam lithography, new routes has been opened up in the field of biosensors in the past decades.[2, 3] In fact, the scientists and researchers have been investigating a multitude of nanosacle biosensors and developing new strategies to apply them in ultrasensitive biosensing use.[4, 5] Examples of such biosensors include optical,[6-8] mechanical,[9, 10] electrochemical,[11] and electrical[12] biosensors. Among these biosensors, nano-scale electronic biosensors offer superior advantages, such as high sensitive to targets, high resolution for localized detection, compatible with standard large scale semiconductor processing, real-time and label-free detection in a nondestructive manner.

Among many different materials such as semiconductors, metal oxides, and carbon nanotube, CPs have shown great promise as a material for sensor application.[13, 14] Their excellent chemical and tunable electrical properties[15] along with biocompatibility[14-16] and benign electrochemical[17, 18] or chemical[19] synthesis route offer several advantages over other materials. When integrated as a semiconducting channel in an FET, change in the surface potential caused by specific binding of targeted charged analyte to a biorecognition molecule on the surface

causes change in the electrical properties of the CPs. However, the use of CPs nanowires for biosensing application has been limited due to their incompatibility with traditional micro-fabrication processes such as lithography due to its possible thermal damage during these processes. Hence, it is necessary to develop new fabrication method that allows high throughput production of CPs.

Recently, there has been an increasing interest to integrate advanced biosensors into lab-on-a-chip systems by introducing microfluidics.[20] The microfluidic devices have advantage including laminar flow, low consumption of costly reagents, minimal handling of hazardous materials, short reaction time required for analysis, multiple sample detection in parallel, portability, and versatility in design.[21] Furthermore, as the increasing demand on direct diagnosis of blood samples, microfluidic devices are employed to separate the red blood cells to eliminate their negative effects. Therefore, developing microfluidic devices with multiple functions would be a future trend because it is capable of simplifying the disease diagnosis procedure.

The early detection and diagnosis is one of the key challenges in cardiac vascular diseases control and prevention. Proper and effective clinical treatments are directly linked with the success of early detection of cardiac diseases, which enable to reduce the suffering and cost to society associated with the diseases.[22] B-type natriuretic peptide (BNP) is one of the most important cardiac markers for the prediction and diagnosis of heart failure. It is well known that when a patient's heart failure symptoms begin or worsen, the ventricles in the heart secrete BNP, causing an elevated level of the marker in the blood. In general, the greater the BNP level in the blood, the more severe the condition. The blood BNP concentration under normal conditions is ~20 pg/mL (6 pM), and it increases to ~2 ng/mL (600 pM) for patients diagnosed with severe congestive heart failure. Because this concentration is extremely low in blood, conventional BNP

detection techniques thus usually requires expensive instruments such as a photomultiplier or excitation light source. Hence sensitive yet expensive, specific yet complicated biosensors are highly demanded for fast detection of cardiac diseases in early stage.

In this chapter, various novel types of high sensitivity nano-sensors categorized by different signal detection strategies and the fabrication methods for nanowires are reviewed at first. The recent progress on CPs biosensors and miniaturized system for sensors are also introduced. Although many new nano-sensor platforms are not fully optimized for manufacturing scale up and commercial use, they can provide alternative and irreplaceable diagnostic models. The developments of FET biosensors for BNP are presented as well.

1.1 BIOSENSOR CATEGORIES

Generally, biosensors are categorized by the types of transducers they used, which convert the biochemical interactions into measureable signals. Optical, mechanical, electrochemical, and electrical transducers are typically used in biosensors. The transduction efficiency providing by the transducers determines many of the analytical characteristics of the biosensors, such as the signal stability, reproducibility, detection limit, and in many cases the operational stability and selectivity. Different transducers have different detection performance. Hence, different biosensors are introduced according to their transducer types in this section.

1.1.1 Optical Transducer

Optical detection principle relies on the unique interactions between nanomaterials and light waves. The sensitivity is highly dependent on the optical phenomena being detected. Surface plasmon resonance (SPR) is a standard method to monitor the interactions between proteins and substrate. It measures the changes in the refractive index of certain types of metal thin films when target molecules bind to the surface. When the surface is excited by electromagnetic radiation, a coherent oscillation of the surface conduction electrons occurs, which results in resonance related to its environment.[23] Most recent methods allow limits of detection at about 25 ng/mL and a dynamic range of 2 logs.[6] However, SPR generally has poor resolution and specificity due to bulk solution interference and is difficult to be applied for high throughput screening.

A unique property of SPR occurs when the light interacts with metal particles that are smaller than the wavelength of light, like nanoparticles (NPs). The plasmon oscillates locally around the NP, known as the localized surface plasmon resonance (LSPR). LSPR sensors are sensitive to the size, shape, and environment of metal NPs when their local refractive index changes.[8] The small refractive index changes cause to changes in the extinction spectra of the NPs, which can be used to detect biomarker molecular recognition events. LSPR nanosensors have been developed into a multi-arrayed biochip with limits of detection of 100 pg/mL.[7] However, the development of LSPR nanosensors requires highly uniform nanomaterials to produce a narrow LSPR peak.

Surface-enhanced Raman scattering (SERS) of single molecules is a major detection signal of interest in nanosensors because metal or core-shell NPs offer large Raman scattering enhancement factors. Important works by Nie and colleagues have explored the SERS field in

nanotechnology[24] as well as for in vivo cancer detection.[25, 26] However, the Raman scattering enhancement effect is dependent on the NP spatial location with respect to the target biomarker as well as among each other.

1.1.2 Mechanical Transducer

Mechanical detection principle is based on the ultrasensitive detection of extremely small mechanical forces on the molecular scale. Nanomechanical sensors can measure transport and affinity on the molecular scale as well as forces, mass changes, and displacements. Mass resolution of mechanical devices is proportional to the total mass of the device. Thus as mechanical sensors turn to the nanoscale, the mass resolution greatly increases. Detection of biomolecules in vacuum[27] and in fluid[28] has been reported. However, fluid detection, which is an ideal condition for biomolecular, is a major obstacle for mechanical nanosensors. The sensitivity of the mechanical sensors is greatly reduced by viscous damping in fluid. Suspended cantilever resonators are a unique alternative for biomarker detection in fluid, because particles can be weighed in real time as they flow through the channel.[28]

The main device in mechanical nanosensors is the microcantilever. When the analyte molecules attach to the immobilized receptors on the surface of a cantilever, the cantilever undergoes two responses to measure the displacement. Firstly, the resonance frequency of the cantilever shifts due to mass increase or decrease from molecular interaction. Secondly, the cantilever bends because of surface stress by the adsorption of the molecules. The bending and resonance frequency shifts are measurable using established techniques such as optical beam deflection, piezoelectricity and capacitance.[9] However, detection specificity of microcantilevers is very low.

Mechanical nanosensors are still limited for clinical applications. The sensitivity and selectivity of nanomechanical sensors are dependent on the uniformity of cantilevers and surface coating efficiency. Additionally, efficient mechanical sensing requires sensitive instrumentation to reduce background noise, which can be costly.[10]

1.1.3 Electrical Transducer

Electrical detection is a rapidly developing field with simple and low-cost fabrication techniques. Nanosensors by electrical detection, typically nano field-effect transistors (FETs), offer simple, direct, and real-time measurements as well as portable capabilities. FET-based electrochemical nanosensors utilize nanowires, nanoribbons, and nanotubes to measure the change in conductance or resistance induced when the target molecule binds to the receptor. [29, 4]

Silicon nanowires are commonly utilized because of their high sensitivit. Lieber and co-workers in 2001 demonstrated the first use of Si nanowires for direct, sensitive, and real-time detection in aqueous solution.[30] This proof-of-concept Si nanowire FET sensor detected protein concentrations as low as 10 pM.[31, 32] Zheng et al. developed multiplexed electrochemical biosensor using Si nanowire field effect devices.[32] The nanowires are functionalized in arrays, giving about 200 individual sensors, to detect multiple protein markers in undiluted serum. When the protein binds to the receptors, the change in the conductance of the specific nanowire is detected. Arrays of different types of doped Si nanowires were used in order to distinguish protein binding signals from noise. This was the first demonstration of high sensitivity electrical nanosensors using Si nanowire arrays.

Carbon nanomaterials are also being employed for FET nanosensors, specifically carbon nanotubes (CNTs).[4] High sensitivity has been reported using CNTs for DNA detection.[5] Cai et

al. developed an array of CNTs with a molecular imprinted polymer coating on the CNT tips to detect proteins using electrochemical impedance spectroscopy (EIS).[11] A key feature in this experiment was the coating of nonconductive polyphenol on the tips of the CNT arrays. The protein of interest was initially trapped in the polyphenol and then removed, leaving an imprint of the protein on the CNT surface. Because of this confining area, high specificity is achieved. Furthermore, this method can be applied for detecting different conformations of proteins. The primary detection mechanism is due to the change in permittivity and resistivity in the surface materials in response to protein capture. The detection sensitivity is dependent on the impedance, which was found to be the highest at the CNT tips because of the faster electron transfer along the CNT tip than the sidewall.

A major limitation of electrochemical biosensors is the inability to detect molecules in high salt solutions.[28, 32] Because electronic detection is based on charge, salt buffers can screen the signal and affect the sensitivity of biosensors. For example, nanowire FETs require a salt concentration less than 1 mM to prevent screening of the signal. One strategy to overcome this salt concentration is to purify the sample upstream of the nanosensors. Stern et al. designed a microfluidic purification system and demonstrated its use by detecting two cancer antigens from a whole blood sample.[12] This remarkable detection under complex physiological conditions is achieved, not because of the FET device, but by the purification chip. The chip captures various types of biomarkers from blood and releases the markers into purified buffer for further electrical deteiton. Pre-processing prevents high salt concentrations from interfering with the electronic signal.

Although electrical sensing can take advantage of nanofabrication techniques, additional design is necessary to reduce the high salt conditions that biosensors are operated. Nanomaterials

can offer high sensitivity thus nanowires, nanoribbons, and nanotubes have been utilized in electrical nanosensor. The challenge in electrical nanosensors is that the high salt concentration of samples can screen signals and reduce sensitivity.

1.2 NANOWIRE FABRICATION TECHNIQUES

Among several of nanoarchitectures, nanowire (NW) is a typical nanostructure that has been attracting considerable attention. NWs are one-dimensional structures where the magnitude of the material is confined to scales of less than 100 nm in two dimensions. NWs have a vast range of potential applications, including electronic, biological, energy, and magnetic devices. NWs can be fabricated by either bottom-up or top-down process. In bottom-up processes, nanostructures are assembled from their subcomponents in an additive fashion. While top-down fabrication strategies use sculpting or etching to carve nanostructures from a bulk material in a subtractive fashion. The demand from industry market has motivated research in NWs for the past number of decades. The massive competition for a share of the global market has driven the expansion of the NW research area, resulting in the evolution of new fabrication techniques, innovative processes, and creative advancements in semiconductor NW device design. To date, many NW fabricate methods have been well developed, such as optical lithography, e-beam lithography, nanoimprint lithography, scanning probe based techniques, tempmate-guided growth approaches. In this section, new NW fabrication methods with high yield and high density is reviewed, including nanoimprint lithography (NIL), superlattice nanowire pattern transfer (SNAP), nanoskiving, nanomolding in capillaries (NAMIC), lithographically patterned nanowire electrodeposition (LPNE), and self-assembly methods.

1.2.1 Nanoimprint Lithography

Nanoimprint lithography (NIL) is a process in which a mold is pressed into a deformable material to form a pattern. The material is then hardened thus when the mold is removed, the topography of the mold is transferred into the material. Its low cost, simplicity, and high fidelity make it attractive for a wide range of applications. NIL has been used to pattern structures for applications such as magnetic disk memory, biosensor microarrays, and microfluidic channels.[33, 34] NIL provides several advantages over alternative optical lithographic techniques. First, NIL is a mechanical process thus its resolution is not limited by the diffraction of light as in optical photolithography. Secondly, NIL tools do not require complex optics and sophisticated light sources, these tools are typically less expensive than optical systems.

NIL was first demonstrated in 1995.[35] The process used a silicon stamp to pattern a thermoplastic polymer at elevated pressure and temperature. In this technique, a mold is pressed into a thermoplastic film while the film is heated above its glass transition temperature. When a high pressure applied, the heated viscous material flows and fills the mold. The pattern is then cooled, and the mold is removed to leave the pattern on the film. Early demonstrations of this technique faithfully transferred 25-nm dot patterns.

Soft lithography generally refers to imprint techniques with a soft (elastomeric) polymer as the template, such as poly(dimethylsiloxane) (PDMS). With soft lithography, a liquid precursor is molded against a patterned master and then cured into a soft stamp. These techniques are typically used to transfer patterns into organic or functional materials, or to transfer an "ink," such as a self-assembled monolayer (SAM) or biomaterial, onto a substrate. Because elastomeric stamp is flexible, soft lithography can also be used to transfer patterns into

nonplanar surfaces. A number of permutations of soft lithography using a soft elastomeric stamp have been developed.[36-38]

Step and Flash Imprint Lithography (S-FIL) is a room temperature and low-pressure imprint technique. In S-FIL, the imprint material is a photocurable, low-viscosity monomer solution and the template is transparent. After the imprint material is dispensed on the substrate, the template is brought into close proximity to the substrate, and the imprint material flows to fill the template pattern through capillary action without the application of elevated pressure and temperature. After exposed to UV light through the transparent template, an inverse replica of the template pattern is obtained when the mold is removed. The S-FIL process was developed in 1999 and was commercialized in fewer than five years.[39]

For NIL techniques, there are few issues need to be addressed in future. The reductions of imprint template and process are needed to improve the uniformity of the imprinted patterns and to increase the wafer yield. The resolution of the imprint templates are not yet very high and thus limited the resolution of patterns.

1.2.2 Superlattice Nanowire Pattern Transfer

The superlattice nanowire pattern transfer method (SNAP)[40] provides an alternative to other nanowire fabrication methods with its own unique advantages. Namely, SNAP can be harnessed to produce large arrays of many types of NWs. The SNAP technique resides between NW materials growth methods and traditional top-down patterning methods.

The fabrication process for SNAP Pt NW arrays is illustrated as follows. First, a custom grown superlattice is cleaved into 2 mm wide and 5 mm long “masters”. One of the 2 mm wide edges is an atomically flat plane. A comblike structure is generated by differentially etching the

superlattice using a dilute etch solution. Pt metal is then deposited onto the superlattice edge at an angle depending upon the pitch of the superlattice. Those Pt NWs are then transferred as an ink by gently dropping them onto a substrate coated with a thin layer of heat-curable epoxy. The epoxy coats the thin film from which the final NWs will emerge. This dropping step may be controlled using a custom-built chuck. The epoxy formulation is critical for ensuring a high process yield. The epoxy/master is heat cured, and the metals NWs are released from the superlattice using a wet chemical etch, thus forming an array of Pt NWs.

SNAP NWs have many advantages. First they inherit their own properties from the thin film substrate from which they are made. This means, for example, that p-type and n-type Si NWs can be readily prepared side by side and that p-n diodes are readily obtained. Some NW materials are uniquely available using SNAP, including insulators and certain metals. Second, the width and pitch of SNAP NW arrays are translated from the precisely controlled film thicknesses and spacings of the superlattice template. Third, SNAP NWs may be a millimeter long or longer. Long NWs can exhibit unique physics, and they enable the construction of relatively large scale NW circuits.

1.2.3 Nanoskiving

"Nanoskiving" is the name that the research group of G. Whitesides given to a technique for the fabrication of nanostructures that combines the deposition of thin films on flat or patterned polymeric substrate using physical vapor methods with sectioning by an ultramicrotome.[41] The first step utilizes an epoxy substrate obtained by curing an epoxy pre-polymer against a flat or patterned PDMS stamp.[42] Current deposition techniques make it possible to form films with nanometer thickness on the surface of this epoxy. They embed the resulting structure in more

epoxy and generate an epoxy block containing an embedded thin film. An ultramicrotome sections this block to produce slabs with thickness about 30 nm. After sectioning, the slabs typically float on the surface of water filling the sample-collecting reservoir of the microtome. The epoxy sections can be transferred onto a solid substrate, and the epoxy is removed by oxygen plasma leaving freestanding nanostructures. The dimensions of the structures are determined by the topography of the substrate, the thickness of the deposited film, and the thickness of the epoxy slab generated by sectioning.

Nanoskiving, on the other hand, still have many issues. Many important procedures in nanoskiving, especially sample mounting and aligning, are currently done exclusively by hand, thus the generation of high-quality sections requires an experienced microtome user. The development of an automated microtome instrument would be required to eliminate the influence of the user on the quality of the section. The sectioning procedure can cause to artifacts and defects in the nanostructures. Brittle materials, such as SiO_2, tend to crack and form small segments during sectioning. The sample can compress during sectioning, causing deformation of the nanostructures and variation of the true thickness of individual nanostructures.[43]

1.2.4 Others

Penner *et al.* have recently described a new method for patterning electrodeposited metal nanowires on glass using photolithography.[44] That method, called lithographically patterned nanowire electrodeposition (LPNE), involves the photolithographic fabrication of a sacrificial template on the glass surface composed of photoresist and a metal film. They demonstrated that LPNE provides the means for patterning noble metal nanowires with lateral dimensions down to 18 nm on glass surfaces.[45] These nanowires can be 1 cm or more in total length. In their report,

LPNE is used to produce nanowires of gold, platinum, and palladium on various films. Moreover, LPNE method enables the fabrication of potentially useful nanowire architectures including crossed nanowire networks and nanorod arrays.

Rotello *et al.* reported the use of nanomolding in capillaries (NAMIC) to pattern small gold nanoparticles into stable 1D NP arrays.[46, 47] The covalent linking of Au NPs on the substrate provides 1D arrays having a uniform layer of NPs on the surface with high stability to organic solvents and water. Additionally, owing to the robust chemical immobilization, the patterned Au NPs can be further modified and potentially can be used for biosensor applications.

Self-assembly has been the subject of intense research as a result of the ability of these macromolecules to create dense arrays.[46] The self-assembly process is facilitated by various annealing techniques.[48, 49] Harris *et al.* demonstrated a simple and efficient method for doubling the density of line structures templated by block copolymers (BCP) self assembly. In annealed BCP films containing two layers of parallel horizontal cylinders. Cylinders of the upper layer form over the interstices of the cylinders in the underlying lower laye.[50] While each layer of cylinders has a pitch of *L*, if the matrix between the cylinders is removed, the three-dimensional assembly of parallel cylinders collapses to form an array of parallel cylinders with half the original pitch (*L/2*).[51]

Yun and co-workers[52] demonstrated a versatile concept for fabricating single polymer and metal nanowires in 2004. They showed that single nanowires could be electrodeposited between lithographically patterned gold electrodes on a wafer surface. The application of a controlled current between these two electrodes in an aqueous solution at one of these electrodes initiates the growth of the nanowire in the direction of the second electrode across the gap. Nanowires with minimum widths in the 70 nm range and low contact resistance were achieved in

their work. A recent innovation in the nanowire growth process is the addition of a third electrical contact to this apparatus.[53] This third contact is obtained by patterning the two gold electrodes on a silicon wafer covered with a thin gate oxide. The application of a gate voltage to the silicon back gate during the electrodeposition modifies the morphology of the nascent nanowire during growth, producing a higher degree of wire width uniformity and the possibility to reproducibly obtain nanowires with diameters less than 50 nm.

1.3 CONDUCTING POLYMERS

The emergence of a new class of materials called the CPs opens up exciting new applications in several fields including bioelectronics. CPs contain monomers capable of acquiring positive or a negative charges through oxidation or reduction which in turn contributes to the electrical conductivity in CPs. Some examples of CPs are polyacetylene (PA), polypyrrole (PPy), polythiophene (PT) and polyaniline (PANI). CPs also have highly flexible chemical structure that can be modified to acquire desired electronic and mechanical properties. Since the CPs have the ability to efficiently transfer electrons produced by biochemical reactions, they have been used extensively in biosensors in the form of transducer. They are also known to be compatible with biological molecules in neutral aqueous solution. For the same reason, CPs have attracted much attention as a suitable matrix for entrapment of biomolecules. In this section, the state-of-art of CPs based sensors developed for biomedical applications are reviewed.

Clark and Lyons[54] developed the first biosensor device almost 50 years ago by integrating enzyme and glucose oxidase to an electrode. Many efforts have been made in the development of biosensors for use in diagnostic detection in past decades. Moreover, recent

advances in lab-on-chip devices have stimulated demand for portable, highly sensitive, real-time, and precise analytical tools for easy detecting analytes such as glucose, cholesterol, antibodies, nucleic acids, hormones, drugs, viruses, and so on.

Since the discovery of metallic polymer,[55] CPs have been extensively used as transducers in biosensors to measure and amplify signals.[56] Both CPs and CPs-nanocomposite materials have been used as transducers. Some of the most commonly used CPs for development of different types of electrochemical biosensors are: PANI, PPy, and PT. Their properties adjustable transport properties, and chemical specificities makes conducting polymers attractive candidates for applications in electrochemical sensing.[57]

Initial research efforts on biosensors predominantly consist of enzymatic biosensors. Another class of sensors known as affinity biosensors (immunosensors, DNA sensors, and receptor sensors) have also become increasingly popular due to their potential to sense biomolecules at extremely low concentrations.[56] Consequently, the immobilization of bioactive molecules in or on the transducer becomes to be a key aspect for obtaining highly efficient affinity biosensors.[58] The modification of biomolecules can be achieved by non-covalent interaction and covalent linkages. To date, both covalent and non-covalent modifications of the biomolecules have been extensively explored and reviewed in detail.[56, 59, 60]

Based on the mechanism used for signal detection and measurement, biosensors can be divided into several categories: amperometric, potentiometric, conductometric, optical, and calorimetric. The most common types of transducers are amperometric and potentiometric. Amperometric biosensors measure the current produced by oxidation or reduction processes happening in the bio-recognition layer. Investigations into amperometric biosensors based on polymeric nanotubes[61] and nanofibers[62] have opened up new frontiers for electrochemical

biosensors. For example, Ekanayake *et al*.[61] developed PPy nanotube arrays enzymatic biosensor for sensing glucose. PPy was deposited on a platinum plated nano-porous alumina substrate which enhanced adsorption of the enzyme-glucose oxidase and provided an increased surface area for the sensing reaction. Potentiometric biosensors use ion-selective electrodes or gas sensing electrodes as physical transducers to measure electric potential due to concentration changes of analytes-of-interest. For example, urea is detected by ureases via the production of NH_3 which, in turn, interacts with PPy to produce an electric potential. A number of pH-sensitive polymers have been synthesized for potentiometric detection of analytes or ions-of-interest in solution.[63] In short, CP-based biosensors are likely to address the issues of biocompatibility for continuous monitoring of biological metabolites and drug dosages, and the possibility of in vivo sensing.[64]

1.4 MINIATURIZED SYSTEM

Biosensors are more preferred as a clinical diagnostic tool than other methods partially because of real-time measurement, rapid diagnosis, multi-target analyses, and reduced costs.[65] As advances in molecular biology have led to our better understanding of potential disease-related protein biomarkers, biosensors became a promising technology for early diagnosis.[66-68] Recently, there has been an increasing interest to integrate advanced biosensors into lab-on-a-chip systems by introducing microfluidics.[20] The lab-on-chip systems have advantages including low consumption of costly reagents, minimal handling of hazardous materials, short reaction time required for analysis, multiple sample detection in parallel, portability, and versatility in design.[21]

The miniaturized systems are also considered as powerful tools for whole blood separation in clinical applications. Recent studies have found that the separation of plasma from blood cells is often critical to eliminate the interference of blood cells (primarily red blood cells), thereby increasing assay sensitivity and reliability. The existence of red blood cells in human blood is a important issue for the performance of most of the biosensors, thus the separation of whole blood within the miniaturized systems is necessary for clinical diagnosis. Many efforts have been made in the studies of utilizing miniaturized systems for blood separation. Separation of plasma on microfluidic devices has been demonstrated using different techniques and platforms, including employing filter trench,[69, 70] using the lab-on-a-CD platform,[71] and exploiting the Zweifach-Fung effect.[72]

Lee *et al.* reported a two-step, self-contained, and self-powered integrated microfluidic blood analysis system (SIMBAS).[70] The system integrates whole-blood plasma separation from red and white blood cells with multiple immunoassays. They utilize the physical properties of PDMS in combination with the microfluidic channel resistance to propel fluid into and through the channels. After removing the device from its vacuum pouch or container, the user simply dispenses the sample droplets onto the multiple inlets of the device and degas-driven flow propels the sample into the device. As the whole-blood passes over the filter trench, blood cells sediment gravitationally thus are filtered while plasma flows into the channel. Finally, plasma-based proteins are detected as the plasma flows across the biomarker detection zone.

Centrifugal microfluidic platforms are of particular interest for assay integration as their artificial gravity field intrinsically implements a pumping force. Haeberle *et al.* present a novel decanting process for the extraction of plasma from the cellular constituents.[71] The blood sample defined between hydrophobic stop and overflow channel flows from the metering chamber *via*

the drain channel into the decant structure. A shock interface separating plasma from the cellular pellet builds out in all parts of the network and proceeds radially outwards at a certain speed. The filling height of the decant chamber rises at counter-current speed before the plasma overflows into the plasma collection chamber. The speed of the filling height in the cell reservoir is adjusted by the hydrodynamic resistance of the drain channel, therefore, only purified plasma advances to the plasma reservoir.

Aran *et al.* have developed a high throughput membrane-based cross-flow microfiltration microdevice to extract 100% cell-free plasma from blood over a wide range of hematocrit concentrations.[69] A membrane based filtration approach was used in this project. The mass flux between microfluidic channels can be precisely controlled by incorporating membranes with various pore sizes in between the channels. The separation membrane is directly bonded as a laminated structure with aligned microfluidic channels so it can operate at high pressures over an extended period of operation (over 4 h).

Yang *et al.* developed a microfluidic device for continuous, real time blood plasma separation for the application of the online monitoring of inflammatory responses.[72] In their report, plasma separation is accomplished by a simple microfluidic network based on the Zweifach-Fung effect. When erythrocytes (red blood cells) flow through a bifurcating region of a capillary blood vessel, they have a tendency to travel into the daughter vessel which has the higher flow rate leaving very few cells flowing into the lower flow rate vessel. The critical flow rate ratio between the daughter vessels for this cell separation is approximately 2.5 when the cell-to-vessel diameter ratio is of the order of one. The reason for this phenomenon is that cells are drawn into the higher flow rate vessel because they are subjected to a higher pressure gradient. In

addition, the asymmetric distribution of shear forces on the surface of the cell produces a torque on the cell, pulling it towards the faster flow rate vessel.

To become useful diagnostics tools in POC settings, microfluidic systems would require further improvement by integrating the sample preparation, possibly including on-board reagent storage, incorporation of multiplexed biomarker detection on a single device, and minimization of the number of user steps required to perform an assay, without compromising device functionality or assay sensitivity. Some of the most important improvements will include simplifying the microfluidic design, reducing the amount of external support equipment required, the number of on-chip components (such as valves), the number of fabrication steps, and the range of different materials used. These steps would reduce the cost of manufacture while increasing device reliability.

1.5 BIOSENSOR FOR BNP BIOMARKER

Nowadays, BNP has become to one of the most important cardiac markers for the prediction and diagnosis of heart failure since the first discovery of BNP in 1988. In general, the measurement of BNP concentration in blood needs huge and expensive equipment such an excitation light source or photomultiplier. Recently, Yukari et al.[73] reported a highly sensitive and low-cost immunoassay method for BNP measurement, but the detection limit for BNP (20-40 pg/mL) was still insufficient to detect the basal level of blood BNP. A year later, Osamu et al.[74] developed a novel miniaturized enzyme immunosensor for BNP detection using microfluidics combined with a portable SPR system. The sensor can determine BNP with high sensitivity. In addition, the detection limit and assay time are greatly improved. A detectable

concentration range of 5 pg/mL-100 ng/mL by monitoring the SPR angle shift was achieved, which covers the required detection range for the BNP concentrations found in blood.

In 2008, a two-dimensional cross-linked polysiloxane Langmuir-Blodgett film has been reported to be useful as a permselective layers in amperometric BNP biosensors.[75] The use of monolayers of proteins, nucleic acid bases, redox-active molecules, and synthetic polymers for the construction of biosensors. The chemisorption-desorption process of thiol monolayers was utilized for the measurement of cardiac biomarker. The dynamic range for BNP was found from 40 to 200 pg/mL and the total assay time was 70 min.

A silicon nanosensor technology based on electrical impedance measurements has been developed for the detection of BNP.[76] Nanoporous alumina was integrated with silicon microelectronics to generate robust ultra-porous devices for rapid proteomic diagnostics of clinical samples. The nanosensor miniaturizes the high-density, low-volume multiwell plate concept. This technology has the capability to achieve near real-time detection a dynamic range of 1 ag/mL to 10 μg/mL for BNP.

Despite very sensitive biosensors were built for the BNP detection, it is suggested to monitor the BNP biomarker on a regular basis in blood or serum samples for those at an elevated risk of heart failure so that a negative event could be detected even before the patient actually started feeling badly. While these were few reports about the BNP measurement in blood or serum. Hence for this purpose, biosensors that can detect trace level of BNP in real blood or serum sample with fast response, low cost, and high reliability are highly desired.

2.0 ELECTROCHEMICAL DEPOSITED CONDUCTING POLYMER BIOSENSOR

2.1 INTRODUCTION

Advanced biosensors based on nanostructured materials for point of care diagnosis are in high demand in recent years. Devices made from conducting polymer nanowires,[14, 77] semiconductor nanowires,[32, 78, 79] and carbon nanotubes[80-82] have been used for the real-time detection of viruses, small molecules, and proteins because of their extraordinary electrical, mechanical, and thermal properties.[32] Although single-nanowire-based biosensors have achieved outstanding detection performances, there is still much room for further improvement in terms of the detection rate, sample volume consumption, specificity, fabrication complexity, and cost.

One strategy to significantly improve biosensors' overall performances is to incorporate them into microfluidics. Microfluidic devices have several advantages such as the reduced consumption of samples and reagents, comparatively fast and more sensitive reactions, and intrinsic compatibility.[83] So far, reversible sealing methods including mechanical fixation[84] and adhesive tape sealing[85] have been used to integrate pre-functionalized biosensor chips with microfluidic systems. However, reversible seals provided by simple van der Waals contact can only withstand fluid pressures up to ~5 psi. As a result, combining microfluidic systems with pre-functionalized single nanowire biosensors via irreversible sealing still poses a challenge.

Another strategy to improve the functionality of biosensors is to use aptamers as detection probes because they are highly specific to their targets. Antibodies have been extensively used as probes to detect targets such as prostate-specific antigen (PSA) and immunoglobulin (IgG).[32, 86, 87] Nevertheless, those probes can be easily denatured under severe conditions, and thus limit their use in practical applications. As an alternative probe, aptamers are more favorable because their target specificity and affinity are often superior to those of antibodies.[82] Aptamers are artificial oligonucleotides (RNA or DNA) that can be isolated from combinatorial nucleic acid libraries using *in vitro* selection methods.[88] As a result, aptamers can be synthesized at relatively low cost, and be easily engineered when necessary. When subjected to certain severe conditions, aptamers are stable or undergo reversible conformational change; under the same conditons proteins are irreversibly denatured. Because of these advantages, aptamers have been investigated and touted as novel probes for protein sensing with high specificity.[89]

In this chapter, we present aptasensors based on aptamers incorporated polypyrrole nanowires (PPy-NWs) for rapid and label-free detection of proteins within microfluidic systems. Immunoglobulin E (IgE) is used in this work to demostrate the rapid response and high specificity of the aptasensor. According to this principle, another aptasenor is developed to detect Mucin 1 (MUC1), which are known to be overexpressed in almost of all human epithelial cell adenocarcinomas, including lung,[90] prostate,[91] breast,[92] and ovarian.[93] The expression of MUC1 increases so much in many cases thus large amounts of the protein can be found in blood,[94] which makes the detection of MUC1 potentially useful for cancer diagnosis.

2.2 EXPERIMENTAL

2.2.1 Chemicals

Pyrrole (≥99.5%), NaCl, and bovine serum albumin (BSA) were purchased from Sigma Aldrich. IgE protein was obtained from Athens Research & Technology, and MUC1 protein was purchased from peptide synthesis facility of the University of Pittsburgh. Aptamers for IgE and MUC1 were synthesized by Integrated DNA Technologies (IDT; Coralville, IA, USA). Phosphate buffer solution (PBS, pH 7.4) was used to prepare the BSA and IgE solutions with different concentrations.

2.2.2 Preparation of Aptamer Incorporated PPy-NW

The aptamers incorporated PPy-NWs were electrochemically grown in patterned polymethylmethacrylate (PMMA) nanochannels between two Au electrodes on a wafer chip cutted from a whole 4 inch wafer (figure 2.1). An illustration of the preparation of aptamer incorporated PPy-NW is schematically shown in figure 2.2. A drop of electrolyte solution consisting of pyrrole monomer (5 mM), NaCl (10 mM), and aptamer (2 μM) was placed on the nanochannel between the electrodes. Then a constant current was applied between the Au electrode pair and the corresponding potential across the electrodes was monitored during the growth process. When the potential drops close to zero (normally around 500 μV), the nanowire is grown and connected between the electrodes (see figure 2.3a and b). After the nanowire preparation, the samples were rinsed with deionized water three times. The nanowires were then examined using fluorescence microscopy.

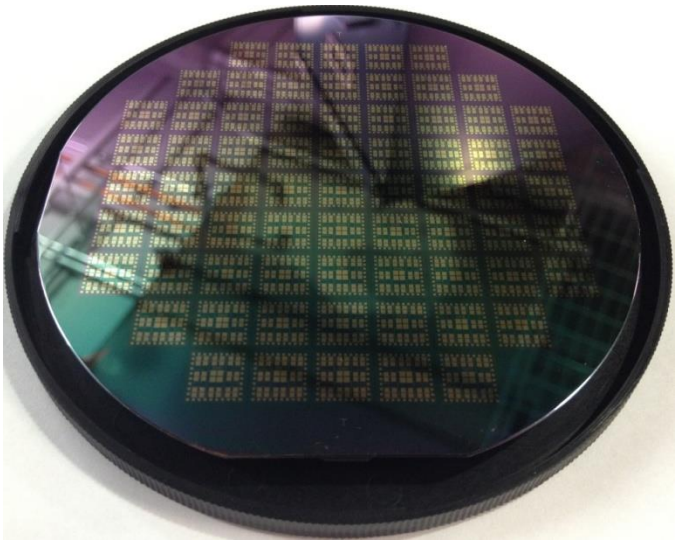

Figure 2.1. A whole 4 inch wafer containing 69 small chips.

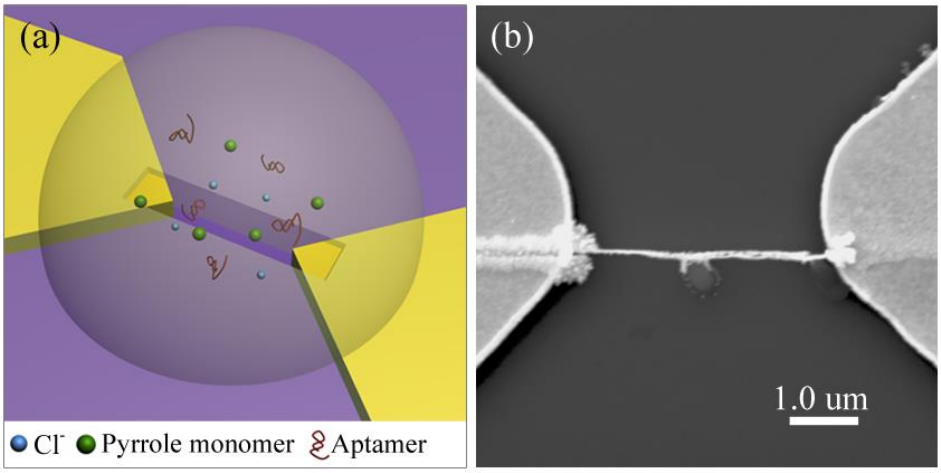

Figure 2.2. (a) Schematic illustration of the aptamer incorporation during the PPy-NW synthesis. (b) Scanning electron microscopy image of an aptamer incorporated PPy-NW grown between the gold electrodes pair.

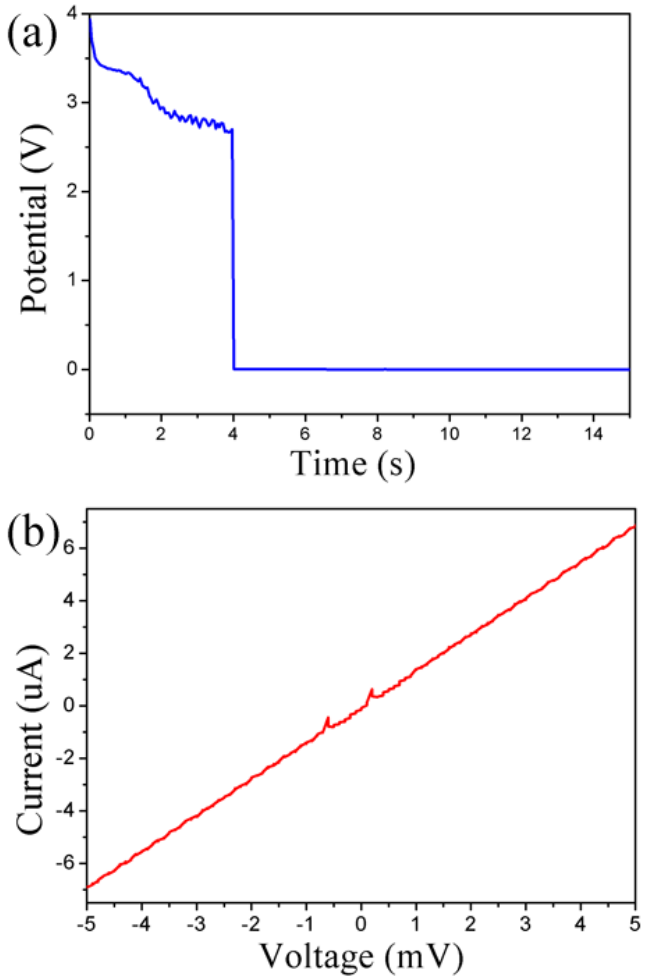

Figure 2.3. (a) Chronoamperometric curve of the electrochemical deposition of aptamer dopted PPy nanowire. The potential between the electrodes pair drops close to zero once the nanowire is grown. Typically the nanowire growth can be completed in 20 seconds. (b) The *I-V* curve of an aptamer doped PPy nanowire with a resistance measured as 715 ohms.

2.2.3 Integration of Microfluidic Aptasensor

A poly(dimethysiloxane) (PDMS) microfluidic structure with six channels was fabricated through a replica molding process with a SU8 master. PDMS was selected for this work because it is a biocompatible material.[95] The PDMS replica was treated with oxygen plasma for 1 minute,

and irreversibly sealed on the chip containing the aptasensors. A hole was punched through the PDMS on both ends of each microchannel and tubings were inserted into these holes to complete the microfluidic aptasensor.

2.2.4 Conductance Measurment

The real-time IgE detections in 10 mM phosphate salt buffer (PBS, pH=7.4) solution were performed at room temperature using the aptasensor with and without the microfluidic system. The PBS solution was placed on the aptasensor and then a constant current (100 uA) was applied across the nanowire. The conductance of the nanowire was monitored. When the conductance of the aptasensor stabilized in the PBS solution, the non-specific protein bovine serum albumin (BSA) solution was added, followed by several IgE solutions with different concentrations. The same procedures were performed for the IgE and MUC1 detections using aptasensors within the fabricated microfluidic system (figure 2.4) in this work.

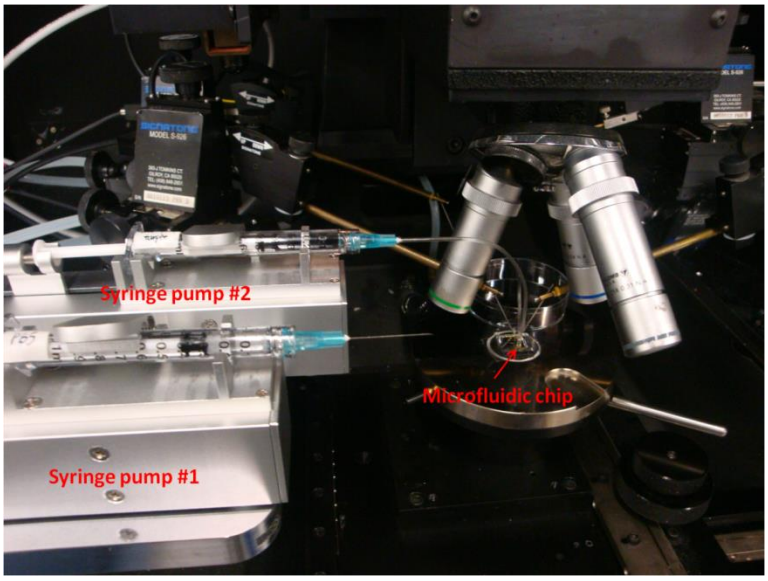

Figure 2.4. The microfluidic system. Two syringe pumps are used to flow the PBS and target solution. The solutions are injected in to the microfluidic channel through tubing.

2.3 RESULTS AND DISSCUSION

2.3.1 Fluorescence

To confirm that the aptamers were successfully incorporated into the PPy-NWs, fluorescent-dye-labeled (Fluorescein amidite, FAM) aptamers were used during the electrochemical deposition. The physically adsorbed aptamers were removed by rinsing the nanowires with deionized water for three times. As shown in figure 2.5, the PPy-NW was connected with the gold electrodes by two thick ends that ensured good contact. The fluorescence microscopy image (figure 2.5b) showed that the dye molecules were successfully entrapped in the PPy-NW. The nanowire exhibited green emission (bright region) with uniform distribution over its surface, which indicates that the aptamers were incorporated into the PPy-NW. Remarkably, clear fluorescence can be observed from most of the PPy-NWs incorporated with fluorescence-labeled aptamers, suggesting the excellent reproducibility of this aptamer incorporation approach.

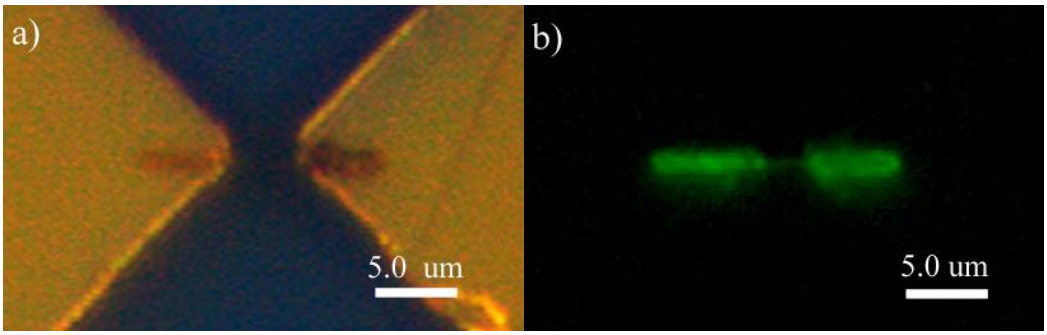

Figure 2.5. Optical (a) and fluorescence microscopy (b) images of an aptamer incorporated PPy-NW grown between the gold electrodes pair. The fluorescence image confirms that the aptamers have been successfully incorporated into the PPy-NW. Scale bars are 5.0 um.

2.3.2 IgE and MUC1 Detection

The normalized real-time response $[(G-G_0)/G_0]$ of the aptasensors and the control sample are shown in figure 2.6a. For the IgE aptasensor (without microfludic system), non-appreciable changes in the curve were found upon the addition of BSA (1.5 uM). In contrast, significant conductance increases were observed in the curve after the addition of IgE solutions. This observation indicates that the aptasensor has a good specificity to IgE protein. On the other hand, the negative control of PPy-NW (without aptamers) only showed negligible changes corresponding to BSA and IgE solutions, which further confirms the excellent specificity of the aptasensor. Stepwise conductance increases were shown in the same figure upon the addition of IgE solutions on this aptasensor. After the addition of a 0.1 nM IgE solution, the conductance of the aptasensor increased rapidly and then stabilized slowly within 200 seconds. As the IgE concentration was increased to 1 nM, 10 nM, 100 nM, and 1 μM, consistent increases in the aptasensor conductance of 1.10%, 1.46%, 1.69%, and 1.77% were observed respectively, using the baseline as a reference. This response increase is attributed to an increase in the negative charge density on the PPy-NW resulting from the specific binding event.[77] The PBS solution of pH 7.4 caused the IgE protein to be negatively charged because it is higher than the isoelectric point of the IgE protein (pI=5.2–5.8). Therefore, the specific binding of the aptamer and the negatively charged IgE protein would result in an increased negative charge density on the PPy-NW, which could lead to the conductance increase.

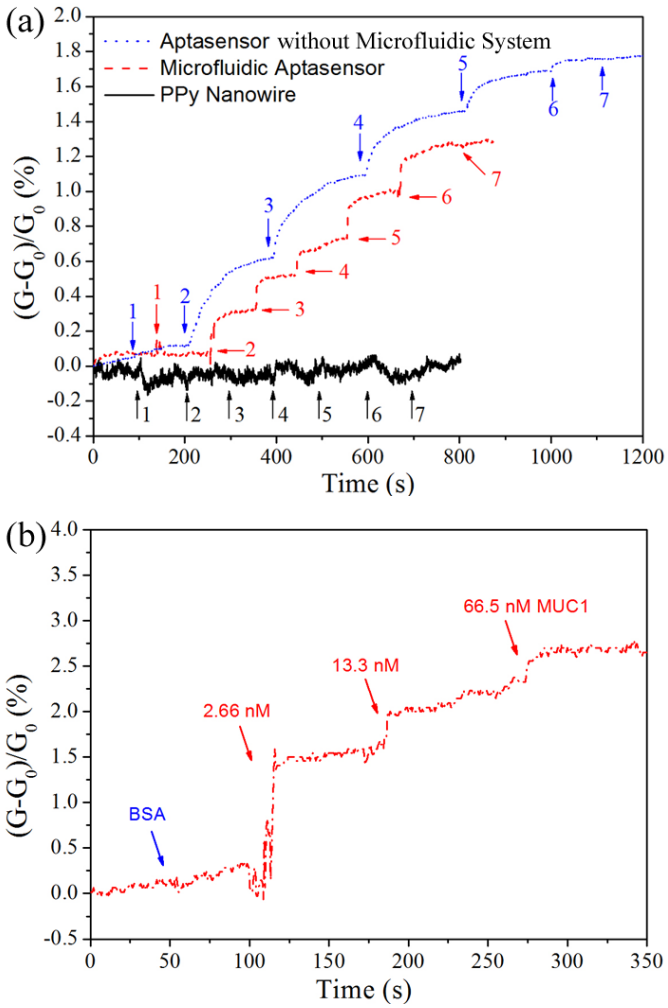

Figure 2.6. (a) Normalized real-time response of aptasensor, microfluidic aptasensor, and PPy-NW to BSA and IgE solutions. Arrows indicate the points of injecting protein solution [Aptasebsor and PPy-NW: 1&7. 1.5 μM BSA; 2-6. 0.1, 1, 10, 100, 1000 nM IgE. Microfluidic aptasensor: 1&7. 1.5 μM BSA; 2-6. 0.01, 0.1, 1, 10, 100 nM IgE.]. (b) Normalized real-time detection of cancer biomarker MUC1 using MUC1 specific aptamer incorpoarted PPy-NW sensor within the microfluidic system.

The obtained detection results (figure 2.6a dot-line; without microfluidic system) indicate that the aptasensor was almost saturated at 1 μM. Therefore, the IgE concentration was optimized from 0.01 to 100 nM for the microfluidic aptasensor. As shown in figure 2.6a, stepwise responses were also observed. The conductance of this microfluidic aptasensor changed rapidly and stabilized quickly (~20 s) after the IgE solutions were injected. A similarly enhanced

response was reported previously and attributed to the enhanced effects of diffusion and mass transport of the biomarkers within the microchannel.[83] From baseline, the conductance of this microfluidic aptasensor increased consistently from 0.32% to 1.26% as the IgE concentration increased from 0.01 to 100 nM. The signal-to-noise ratio was 3.6:1 at the lowest IgE concentration. So far, the reported detection limits for IgE are about 0.01 nM and 10 nM using conventional surface plasma resonance (SPR) measurements[96] and quartz crystal microbalance (QCM) biosensors[97] respectively, which are the same or higher than the value achieved in this work. However, rather than optical techniques, electrical detection possesses advantages including not only the portability, but also the independence from the optical path length, sample turbidity, extremely low cost, and low power requirements.

Another microfluidic aptasensor was then fabricated for the detection of cancer biomarker MUC1 using MUC1-specific-aptamer as the detection probe. As shown in figure 2.6b, time-dependent conducatance measurements recorded on the microfluidic aptasensor exhibited no change in conductance upon addition of 1.5 uM BSA. However, a significant increase in the conductance was observed after the injection of 2.66 nM MUC1 solution, demostrating the high specificity of this microfluidic aptasensor. As the concentrations of MUC1 were subsequently increased to 13.3 nM and 66.5 nM, the condunctance of the microfluidic aptasensor was increased to 2.25% and 2.8% respectively. As far as we are aware, the lowest detection concentration for the most popularly used CA 15-3 assay, which is a currently commercially available ELISA kit for the detection of MUC1, is estimated to be 800 nM of MUC1.[98] The results showed here indicates that the aptamer-based detection method within the microfluidic system is not only rapid but also sensitive, with a very low detection concentration of 2.66 nM MUC1.

2.3.3 Sensitivity

Figure 2.7a shows the sensitivities of the aptasensor and microfluidics aptasensor obtained from three NWs for each case. The aptasensor was very sensitive exhibiting $0.79 \pm 0.04\%$ change in conductance even at the IgE concentration of 0.1 nM (20 ng/mL), which is about 2 times greater than that obtained from an aptamer-doped PPy film.[89] On the other hand, the microfluidic aptasensor showed responses to IgE solutions within the range from 0.01 nM (2 ng/mL) to 100 nM (20 μg/mL), showing a $0.57 \pm 0.07\%$ change in conductance at the IgE concentration of 0.1 nM. Despite the small decrease in sensitivity of the microfluidic aptasensor, the reproducible responses of the microfluidic aptasensor remain within distinguishable level. Clearly, both high sensitivity and fast response are important for biosensors. For this microfluidic aptasensor, the sensitivity was decreased probably because of the degradation the biomolecules during the microfluidic device integration process (i.e. the sealing of PDMS replica on the chip). However, using microfluidic system in this experiment showed great improvement on the response time. Optimizing the microfluidic device integration process could increase the sensitivity of the microfluidic aptasensor in future.

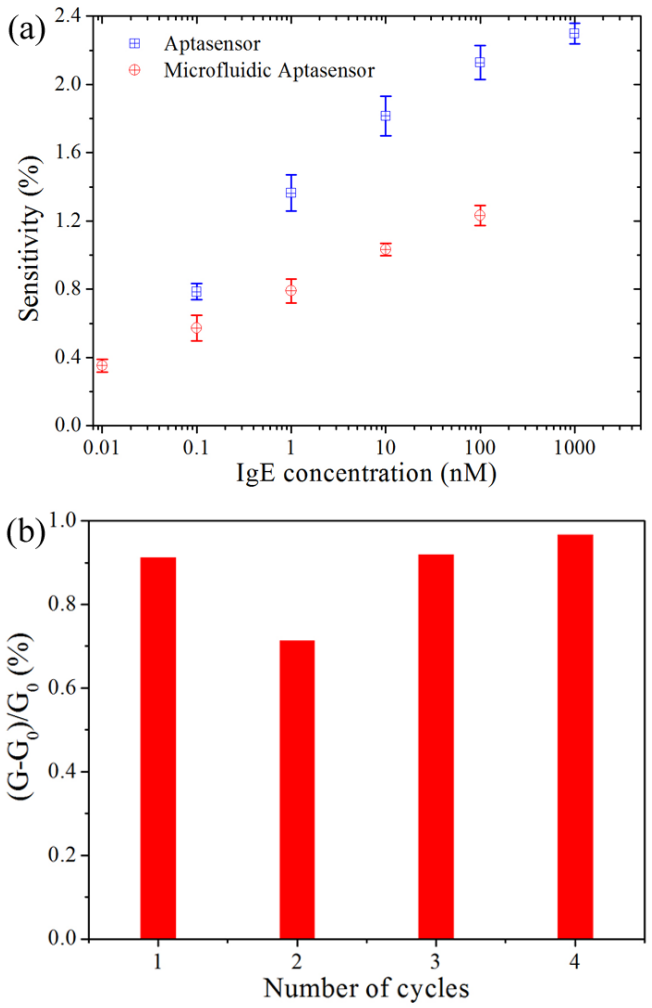

Figure 2.7. (a) The sensitivity of the aptasensor with and without microfluidic system as a function of IgE concentration, data were collected from three aptasensors for each case. (b) Regeneration of the aptasensor upon treatment with 0.01 M HCl. The data are collected with IgE concentration of 0.1 nM.

2.3.4 Reusablity

The possibility of reusing a sensor several times with or without a regeneration step is highly desirable, but typically difficult to achieve. For example, the dissociation of antibody-antigen complexes can usually be achieved by treating with acid solution. However, the antibodies are irreversibly damaged to some extent.[99] In contrast, the aptamers are almost capable of reversible

regeneration. The reversible conformational change of the anti-IgE aptamer was investigated with acid treatment. The used aptasensor was incubated in 1 μL of 0.01 M hydrochloric acid for 15 min and followed by thorough washing with 10 mM PBS buffer. As shown in figure 2.7b, the as-prepared aptasensor showed 0.91% response to the 0.1 nM IgE solution and the incubation restored the aptasensor functionality for up to three repeated measurements with no significant loss of sensitivity. This result indicates the good reusability of this aptasensor.

2.4 CONCLUSIONS

In conclusion, we have successfully demonstrated the Ppy-NW-based microfluidic aptasensor for rapid and real-time detection of IgE and MUC1 with high sensitivity and specificity. The one-step incorporation of biomolecules into the dimension-controllable conducting polymer nanowire eliminates post-synthesis surface modification and simplifies the device fabrication process. The fluorescence microscopic image confirmed the successful incorporation of the aptamers. This microfluidic aptasensor provided fast response and stabilization times. Furthermore, the functionality of this aptasensor can be simply restored by acid treatment with no majoy change in sensitivity. Importantly, the proposed method for aptasensor fabrication can be easily adapted for the development of various aptasensors based on different conducting polymers and different aptamers for specific targets. A microfluidic aptasensor for the detection of MUC1 was accordingly developed. This aptasensor acheived a very low detection concentration of 2.66 nM MUC1 in this research. These results indicates the possibility for developing rapid and sensitive biosensor devices for the detection of cancer biomarkers.

3.0 BIO-SHIELDING MASK FOR NANOWIRE-BASED MICROFLUIDIC BIOSENSOR

3.1 INTRODUCTION

Microfluidic devices are of considerable interest for biosensors because of several advantages that they provide: reduced consumption of sample, protection of the sensor by the microchannels from environment, and comparatively fast and more sensitive reactions.[83] Consequently, microfluidic devices have been used in various areas, such as biological and chemical analysis,[100] point-of-care testing,[101] clinical analysis,[102] and medical diagnosis.[103] Numerous examples found in the current literatures include the detection of pathogens using a microfluidic device,[104] the quantification of nucleic acid sequences by an electrochemical microfluidic biosensor,[103] and multiple ions analysis with a biosensor array microfluidic device.[105] While most microfluidic biosensors use fluorescence[100, 106, 107] or surface plasmon resonance[74, 108, 109] for signal generation, utilizing electrical detection systems offer the advantages of simplicity and high sensitivity.[103, 105]

Poly(dimethylsiloxane) (PDMS) based microfluidics are most favorable for microfluidic devices[95, 110] because the microfabrication in polymers is easy and relatively cheap. The basic microfabrication process of a PDMS based fluidic chip involves the patterning of the channel structure, the sealing of the open channel, and sensor fabrication.[111, 112] Typically, elastic PDMS

is used to replicate microchannels using inverse microfluidic structures from the mold (or master) which can be obtained by photolithography. It is easy to release the PDMS replica from the mold without damaging itself or the mold because of its low surface free energy and elasticity. Finally, enclosed microchannels can be obtained by sealing the PDMS replica to a flat surface.

PDMS can reversibly or irreversibly seal to itself or to other surfaces without distorting its shape.[113, 114] Usually, reversible seals provided by simple van der Waals contact can withstand fluid pressures up to ~5 psi.[114] To obtain seals that can hold higher pressures, oxygen (O_2) plasma treatment is usually employed. However, most microfluidic biosensor devices that use irreversible sealing require surface modification after device assembly because O_2 plasma treatment can damage the detection elements. In particular, it is necessary to prevent damages on the biofunctionalized nanomaterial-based sensors for the integration of microfluidic devices using plasma treatment. Other methods such as mechanical fixation[104] and UV-curable adhesives[95] have been applied to avoid the deactivation of biomolecules immobilized on these nanomaterial-based sensors. But these reversible sealings are not able to withstand high fluid pressures thus limiting their applications. As a result, assembling a PDMS replica to a pre-functionalized chip via irreversible sealing is an important challenge for nanomaterial-based microfluidic biosensors.

In this chapter, we present a low-cost and facile approach that can protect the pre-functionalized biosensor throughout the irreversible sealing process. Inspired by the nanofabrication approaches that utilize masks to make patterns on substrates,[115, 116] we employ a shadow mask to cover the substrate and prevent the damage to biomolecules that would typically occur during O_2 plasma treatment. The effects of shadow mask on the electrical measurement,

the fluorescence intensity, and the detection ability of as-prepared and O_2 plasma treated nanowire (NW) biosensor are evaluated. In addition, an integrated microfluidic biosensor device is demonstrated, which confirms our assumption that the utilization of shadow mask can protect the pre-functionalized sensor during the plasma treatment.

3.2 EXPERIMENTAL

3.2.1 Chemicals

Pyrrole, aniline, NaCl, bovine serum albumin (BSA), 1-ethyl-3-(3-dimethylaminopropyl) carbodiimide (EDC), and N-Hydroxysuccinimde (NHS) were purchased from Sigma Aldrich. Fluorescent-dye-labeled aptamer (5'-GGGGCACGTTTATCCGTCCCTCCTAGTGGCGTGCC-CC-3') was synthesized by Integrated DNA Technologies. Immunoglobulin E (IgE) was provided by Athens Research & Technology. Goat anti-rabbit immunoglobulin G (IgG) monoclonal antibodies (mAbs) and IgG protein were obtained from Invitrogen. Phosphate buffer solution (PBS, pH 7.4) was used to prepare the BSA, IgE, EDC, NHS, and IgE solutions with different concentrations.

3.2.2 Nanowire Preparation and Functionalization

Two different kinds of NWs were fabricated in this work for comparison. One was polypyrrole NWs that incorporated with aptamers (aptamer-PPy) during the NWs growth, and another one was polyanniline (PANI) NWs that surface modified by mAbs after the growth. The details of

the fabrication of addressable single polymer NW can be found in our previous reports.[52, 53] Pre-patterned polymethylmethacrylate (PMMA) nanochannels between the electrodes pairs were used to guide the growth of Aptamer-PPy NWs while a constant current were applied using a semiconductor analyzer (Agilent B1500A). The growth of the NW was monitored by the potential between the electrode pair. The NW growth is completed when the potential decreases to ~500 μV. The electrolyte solution consisting of pyrrole monomer (5 mM), NaCl (10 mM), and aptamer (2 μM) was used to prepare aptamer-PPy NWs. The obtained samples were rinsed with deionized water three times after the NWs preparation.

3.2.3 Oxygen Plasma Treatment and Microfluidic Integration

A PDMS microfluidic structure with six channels was fabricated through a replica molding process with a SU8 master (silicon elastomer base and curing reagent were mixed in a 10:1 ratio, degassed for 1 h, and then cured at 85℃ for 3 hrs). By hollowing out an aluminum plate, six cantilevers were created along the top and bottom sides of the shadow mask. Each cantilever can cover an area with a length of 6.2 mm and a width of 0.8 mm that is enough to protect the NW. The shadow mask was aligned and fixed on top of the silicon chip by stereomicroscopy before the plasma treatment. Figure 3.1a and b schematically show that the shadow mask can completely cover the NWs. The plasma treatments were performed using plasma cleaner (Harrick PDC-32G) for 1 min. For comparison, several samples were treated with O_2 plasma under the same conditions but without the shadow mask.

After the plasma treatment, the shadow mask was quickly taken off from the chip and the PDMS replica was then aligned and stacked on the silicon chip to form an irreversible sealing (figure 3.2). Holes were punched through the PDMS replica on both ends of each microchannel

using a 20-gauge needle and the tubings were inserted into the hole to complete the microfluidic device (figure 3.3a). The successful injection of fluid into the microfluidic channel through the tubing is shown in figure 3.3b.

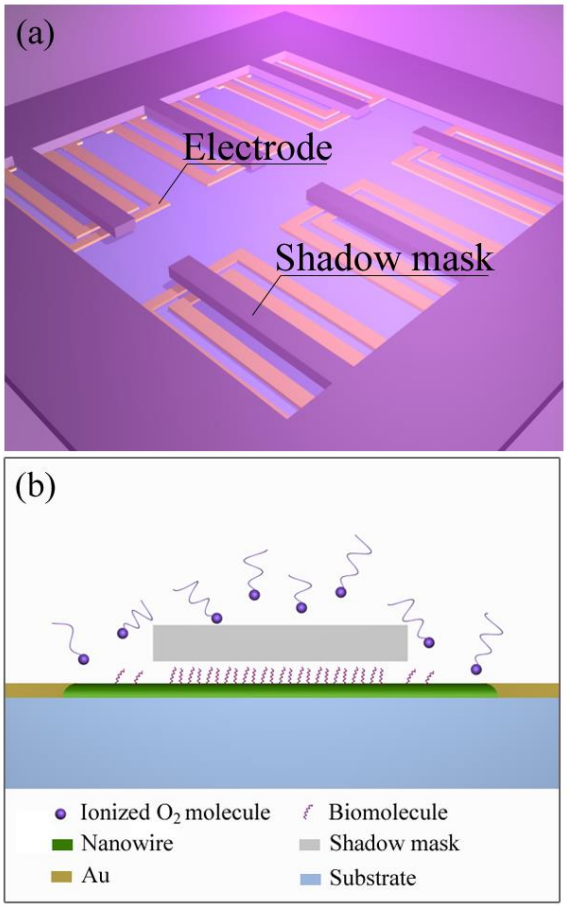

Figure 3.1. Illustration of the plasma treatment for pre-functionalized chip in the presence of shadow mask. (a) Schematic illustration of the O_2 plasma treatment of a shadow mask protected chip. (b) Enlarged side view. The bio-functionalized NW is protected by the shadow mask from the plasma.

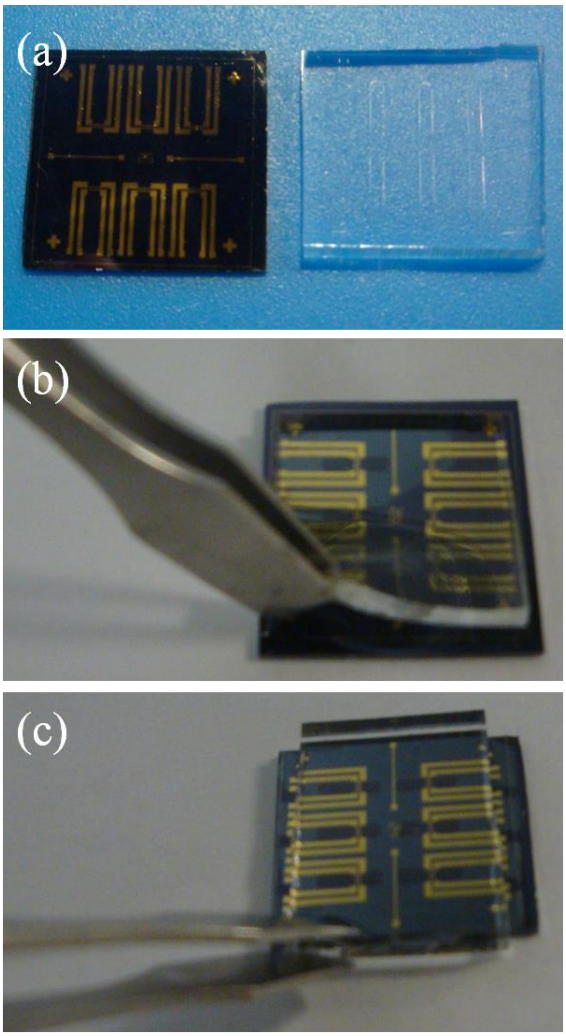

Figure 3.2. Irreversible sealing formed between the PDMS and silicon chip. (a) images of a silicon chip and a PDMS replica that contains six channels. (b) The PDMS can be easily peeled off from the chip if use mechanical attachment. (c) An irreversible sealing can be formed between PDMS and silicon chip after oxygen treatment.

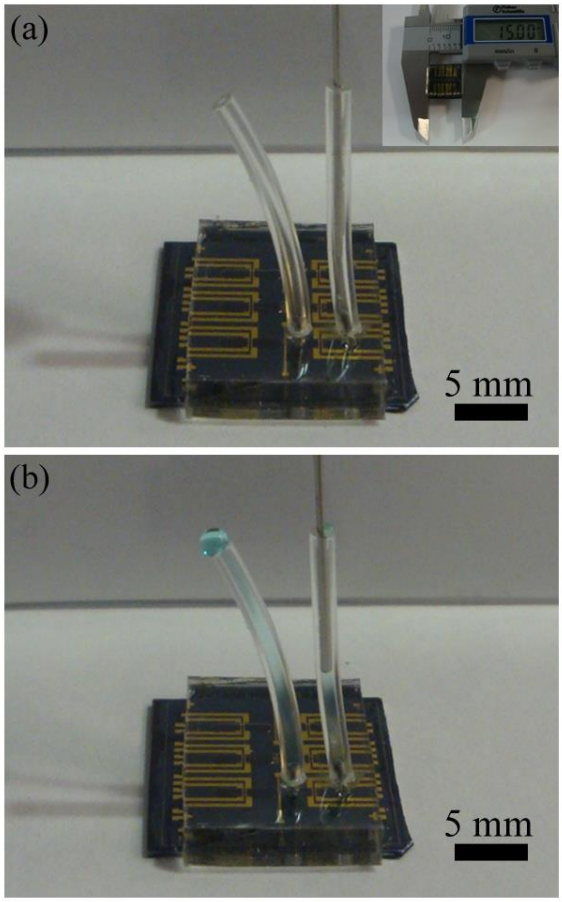

Figure 3.3. Demonstration of the microfluidic device integration. (a) The assembled microfluidic device with inlet and outlet (inset: the chip and the PMDS replica were permanently attached after plasma treatment). (b) The fluid can be successfully injected into the microfluidic channel.

3.2.4 Characterizations

To study the protection effects of the shadow mask on the NWs during the plasma treatment the resistance and fluorescence of as-prepared and plasma treated NWs were measured using a semiconductor analyzer and fluorescence microscope (Axioskop, Carl Zeiss). The fluorescence intensities of NWs samples were further examined using microspectrophotometer (CRAIC Technologies) at emission wavelength of 365 nm. All of these measurements were performed at room temperature.

3.2.5 Protein Detection

To determine whether the activity of the biomolecules can be preserved by the shadow mask after plasma treatment, the target protein detection of the as-prepared and plasma treated NWs were performed. Two different biosensors, one is Aptamer-PPy NWs and another one is surface modified PANI NWs, were used for the detection of IgE and IgG respectively. The proteins detections were carried out by dividing the NWs into two groups for each case: 1) as-prepared functionalized NWs (G-1) and 2) shadow mask protected samples treated with O_2 plasma (G-2). The conductance of the NWs was monitored by applying a constant current (100 μA) using a semiconductor analyzer. When the conductance of the NW was stabilized in the PBS solution, a droplet of non-specific protein bovine serum albumin (BSA) solution was added, and followed by several droplets of target protein solution with different concentrations.

The integrated microfluidic biosensor based on aptamer-PPy NWs was also developed for the detection of IgE protein. The BSA solution was first flowed into the microchannel and

then followed by several IgE solutions with different concentration. The same conductance measurement conditions mentioned above were employed.

3.3 RESULTS AND DISCUSSION

3.3.1 Resistance

The *I-V* curves of aptamer-PPy NWs with and without the protection of the shadow mask when treated by O_2 plasma are shown in figure 3.4. The measured resistances of the as-prepared NWs are about 200 Ω and 320 Ω. After the O_2 plasma treatment, the NW that exposed directly to the plasma was broken, showing no current in the *I-V* curve. On the other hand, the resistance of the shadow mask protected NW remains similar (~600Ω) to its resistance before the plasma treatment. It is well known that plasma has been widely used for surface cleaning: it utilizes energetic ionized gas molecules to bombard the surface. Therefore, without any protection, it is easy to create tiny breaks on NWs with O_2 plasma. These breaks can be prevented via the use of a shadow mask and is confirmed by the results demonstrated above.

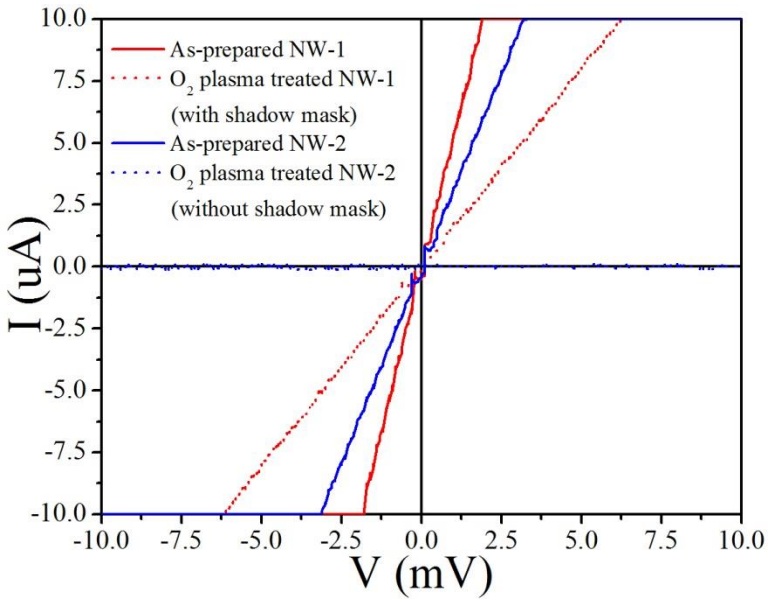

Figure 3.4. *I-V* curves of aptamer-PPy NWs before (solid lines) and after (dash lines) the plasma treatment with (red) and without (blue) the protection of shadow mask.

3.3.2 Fluorescence

Fluorescence images of the NWs functionalized with fluorescently labeled biomolecules were taken by fluorescence microscopy as shown in figure 3.5a. To some extent, the damages on the NWs caused by plasma treatment can be represented by their fluorescence intensity changes. It can be observed from the images that a clear bright line (aptamer-PPy NW) was broken into two short lines with reduced fluorescence intensity after the plasma treatment in the absence of the shadow mask. Conversely, the presence of shadow mask showed non-appreciable changes in fluorescence intensity after the plasma treatment. Quantitative characterization on the fluorescence of the NWs was further performed using a microspectrophotometer. The results are shown in figure 3.5b. The significant reduction in fluorescence intensity of the unprotected NW indicates that plasma treatment can easily damage the NW and the biomolecules. In contrast, only a small intensity reduction is observed for the shadow mask protected NW.

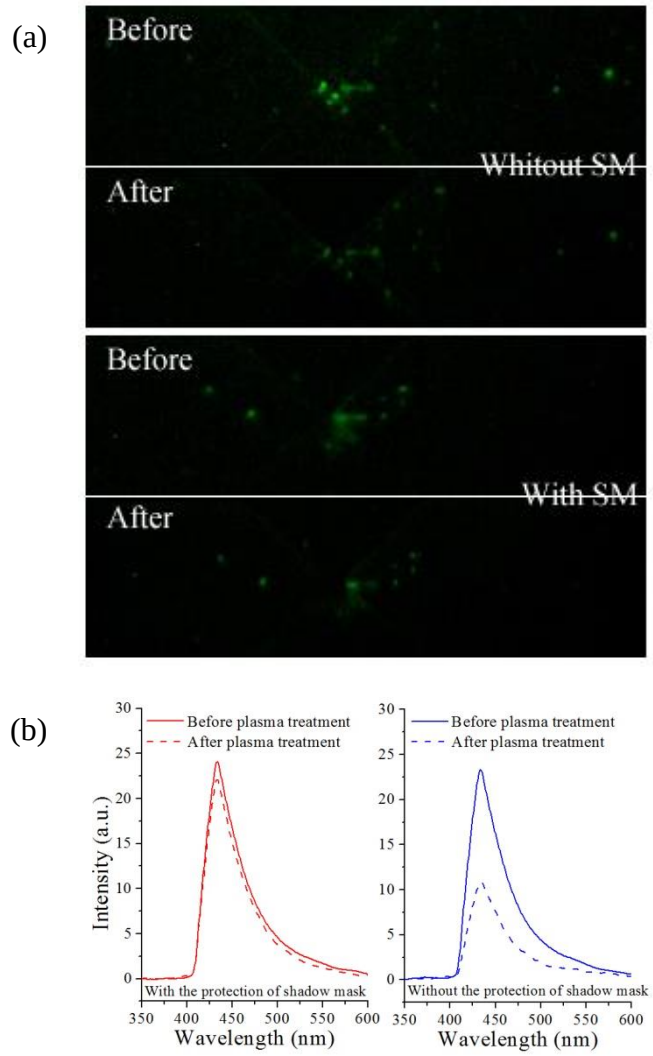

Figure 3.5. Fluorescence characterizations of the NWs. (a) Fluorescence images of aptamer-PPy NWs before and after the plasma treatment with and without the protection of shadow mask. (b) The fluorescence intensity of samples before (solid line) and after (dash line) plasma treatment with (red) and without (blue) the protection of shadow mask.

3.3.3 IgE Protein Detection

In order to determine whether the bioactivity of the biomolecules on the NWs can be preserved by using a shadow mask during the plasma treatment, the proteins detections were carried out with two groups of NWs including as-prepared functionalized NWs (G-1) and shadow mask protected samples treated with O_2 plasma (G-2). The IgE detection result (figure 3.6) shows that the sensitivity of the NWs in G-2 slightly decreased compared to the NWs in G-1. However, the measured values of G-2 remain within the distinguishable level for IgE detection. The result shows that the shadow mask plays an important protective role in preserving the bioactivity of the functionalized NWs from the O_2 plasma treatment.

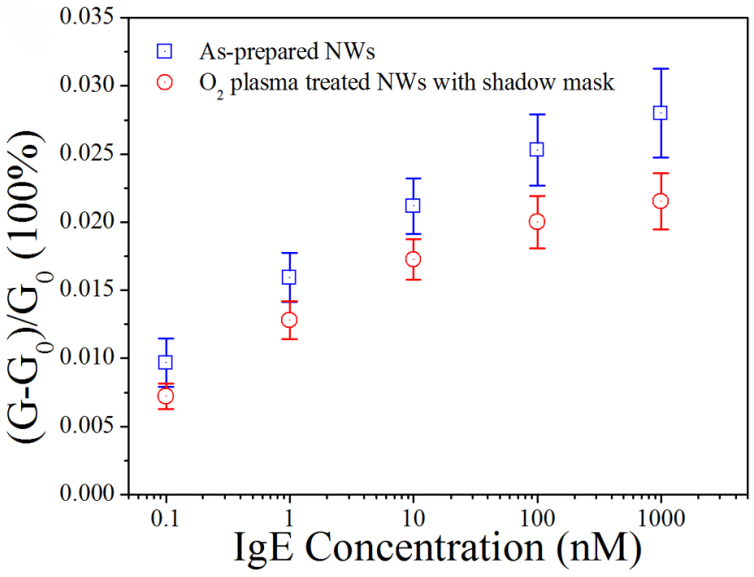

Figure 3.6. Comparison of IgE detection responses of PPy NWs before plasma treatment (G-1) and after plasma treatment with the protection of shadow mask (G-2).

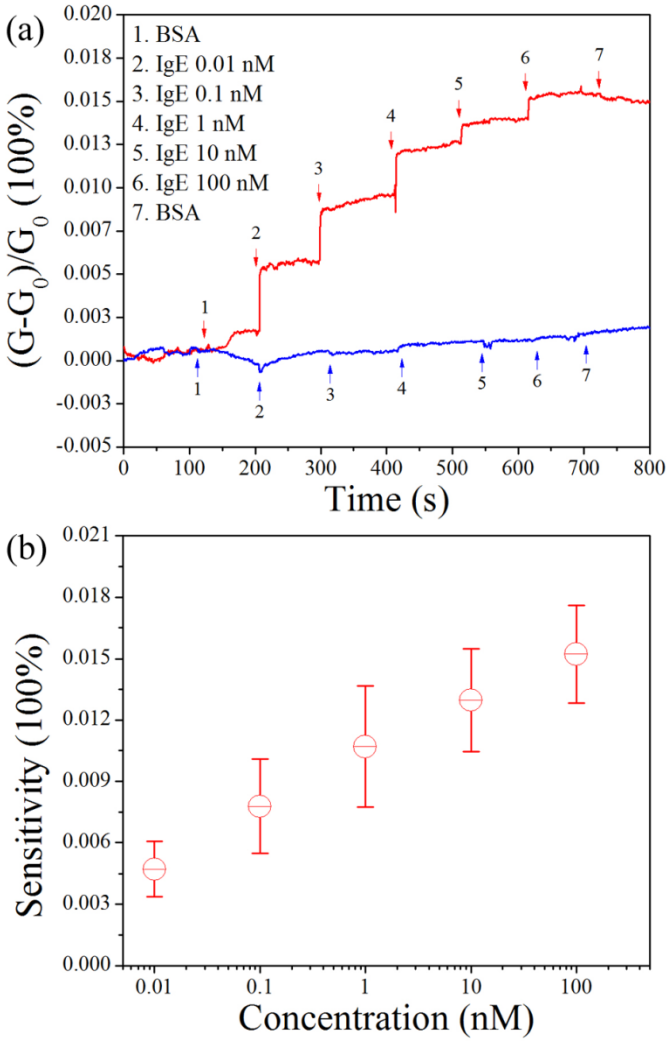

Figure 3.7. IgE detections using aptamer-PPy single NWs based microfluidic biosensors. (a) Normalized real-time response of microfluidic biosensor (red) and PPy NW (blue) to BSA and IgE solutions. Arrows indicate the points of injecting protein solution. (b) The sensitivity of the microfluidic biosensor as a function of IgE concentration.

3.3.4 Microfluidic Biosensor for IgE Detection

Finally, an integrated microfluidic biosensor device based on aptamer-PPy NWs was employed for IgE detection. As shown in figure 3.7a, a stepwise response was observed upon the injection of IgE solutions into the microchannel. As the IgE concentration increased from 0.01 to 100 nM,

the conductance of this microfluidic biosensor consistently increased from 0.58% to 1.56%. Remarkably, the response and stabilization times of this microfluidic biosensor was very fast (few seconds), which is desirable for biosensors. Moreover, the slight changes on the negative control of PPy NW corresponding to BSA and IgE solutions indicate an excellent specificity for this microfluidic biosensor.

The sensitivity of this microfluidic biosensor was calculated from three biosensors and shown in figure 3.7b. This microfluidic biosensor was very sensitive showing a ~0.5% change in conductance at the lowest IgE concentration of 0.01 nM (2 ng/mL). A dynamic range from 0.01 nM (2 ng/mL) to 100 nM (20 μg/mL) was obtained for this microfluidic biosensor. These results demonstrate the applicability of this microfluidic biosensor to detect IgE concentration below and above 1.2 nM (240 ng/mL) which has been established as the normal level of IgE in non-allergic adults.

3.4 CONCLUSIONS

We have successfully demonstrated that employing a shadow mask protects pre-functionalized NWs during O_2 plasma treatment and enables the integration of irreversible sealed microfluidic devices. Significant differences were observed between the bio-functionalized nanowire sensors that treated by O_2 plasma with and without using a shadow mask. In the absence of a shadow mask NWs are destroyed after plasma treatment as shown by the resistance increase and fluorescence intensity decrease. On the other hand, the shadow mask protected NWs maintained a low resistance and high fluorescence intensity post plasma treatment. The detection of IgE protein by aptamer-PPy further demonstrated that the shadow mask can preserve the bioactivity

of the functionalized NWs and that a microfluidic biosensor can be fabricated after the plasma treatment. The integrated microfluidic biosensor developed in this work exhibited fast response and rapid stabilization times. Significantly, this simple but novel approach provides an easy way to assemble irreversiblely sealed nanomaterilals-based microfluidic device without deactivating the pre-functionalized detection elements. Therefore this technique can be widely applied on nanomaterials-based microfluidics for the purposes of biomolecules detection and clinical diagnostics.

4.0 CHEMICAL SYNTHESIS OF PANI PATTERNS

4.1 INTRODUCTION

The development of science and technology of nanomaterials has created great excitements and expectations in the past decades. Nanomaterials can be classified according to the dimensionality (D) of their feature into 0D, 1D, 2D, and 3D nanostructures. 0D nanostructures including quantum dots, nanoparticles, nanosphere, isolated molecules and atoms are point structures with nanoscale in all dimensions.[117] 1D nanostructures such as nanotubes and nanowires are structures with non-nanoscale only in one dimension.[118, 119] 2D nanostructures, for example nanosheet, nanoplates, nanobelts, and nanodisc, are structures with nanoscale in one dimension.[120] Lastly, 3D nanostructures like nanotetrapods, nanoflowers, and nanocombs are arbitrary structures, which contain nanoscale features in any of three dimensions.[121]

The most important aspect of nanomaterials is their special properties associated with their small dimensions. A fundamental characteristic of nanomaterials is the high surface-area-to-volume ratio, which lead to a number of unique physical and chemical properties such as high molecular adsorption, large surface tension force, enhanced chemical and biological activities, large catalytic effects, and extreme mechanical strength.[122] The nanomaterials are thus highly useful for a wide range of nanotechnology fields especially in nanoelectronics and bioelectronics,[117, 118, 120-122] resulting in a dramatically fast growth in the nanosensors field.

Among varies of nanosensors, 0D (nanoparticles) and 1D (nanotube and nanowire) nanomaterials showed great performance improvements in terms of sensitivity and detection limit compared with thin films due to their high surface-to-volume ratio. However, when scale-down the thickness of thin films within nanoscale, the nanometers-thin films then become to 2D nanomaterials. This raises an interesting question: for the 1D and 2D nanostructutres which has better sensing performance if their surface-area-to-volume ratios are similar (or close). It is highly believed that the 2D nanostructure would possess comparable sensing performance to that of 1D nanowire. First of all, similar surface-area-to-volume ratio allows the 2D nanostructure to have similar binding sites density as the 1D nanowire. Therefore, ideally, similar target densities are expected to be bound on both nanostructures, leading to comparable effects on these two transducers. Secondly, the electrical properties of a 2D nanostructure and a 1D nanowire are expected to be close since both of these two structures are still at nano-scale. Thirdly, according to the biosensor sensing mechanism, the thickness of the nanomaterial strongly determines the sensor's response. Because the thickness for both 1D and 2D nanoctructures is the same, similar volume ratio between the volume that can be affected by surface potential change and the total volume of the material is expected. As a result, similar response change is likely to be achieved. It is of interest that if the 2D nanomaterials can exhibit similar performances to that of 1D nanomaterials because 2D materials offer many benefits in the emerging field of large-area and low-cost electronics.

Carbon is one of the most notable examples, which has all dimensionalities of 0D fullerene, 1D carbon nanotubes (CNTs), 2D graphene, and 3D graphite, diamond, and amorphous carbon.[123] In 1D structure, carbon atoms are arranged as single wall or multiwall carbon nanotubes (SWCNTs/MWCNTs). Because of their very small diameters and relatively

long lengths (up to several millimeter), CNTs are prototype hollow cylindrical 1D quantum wires. Depending on the atomic orientations along the tube axis, the CNTs exhibit unique electrical and mechanical properties. With those properties, CNTs have been the center of attention for the development of advanced electronics, sensors and fuel cell platforms in the past years.[123] Semiconducting CNTs can be used to build up FET devices that can work at room temperature and in ambient conditions. The majority of research towards biosensing involves the interactions of proteins with carbon nanotubes. For example, CNTs based sensor devices have shown the ability to detect gases such as NO_2, NH_3, H_2, CO, NO, CO_2, and O_2.[123] In addition, Li et al.[86] studied the complementary detection of prostate-specific antigen by using a CNTs based FET device. They found the limit of detection was ca. 500 pg/mL, or 14 pM, at a signal-to-noise ratio of 2. Many studies about CNTs FET biosensors showed that the detection limit of such device can be as low as hundreds picomoles.[124]

Carbon atoms also form a flat monolayer, tightly packed in a 2D honeycomb lattice, called as graphene.[123] Graphene exhibits exceptional strength and possesses many other novel electrical and optical properties that have scientists buzzing. The electronic, thermal, and mechanical properties of graphene make it attractive for a variety of potential applications, including sensors, electronics, energy storage, and solar. While not as matured, the field of graphene-based sensors is dramatically growing, and their electrical response to various chemical species is qualitatively similar to CNTs. Examples have been reported for the detection of both NO_2 and NH_3 with graphene-based devices.[123] The detection limits range between the parts per billion (ppb) and parts per million (ppm) levels. This sensitivity is comparable to CNT-based sensors. Furthermore, graphene-based FETs can be employed for biomolecule sensing. Chen and co-workers[125] reported that large-scale chemical vapor deposition (CVD) grown single- and few-

layer graphene films are highly sensitive to DNA hybridization. The sensor detection limit was found about 10 nM for single stranded DNA. Other studies demonstrated that graphene-based sensor devices were capable of detecting targets as low as few nanomoles,[126] which is comparable to that of CNTs-based sensors.

Silicon nanomaterilas have drawn tremendous attention as a promising transducer in biosensors as well. Due to their excellent semiconducting properties, most of the 1D SiNWs sensors are designed as field effect transistor sensors. An early measurement made by Cui et al. reported the real-time detection of streptavidin binding to biotin-modified SiNW FET.[30] They found out that biotin-modified SiNW FET was able to detect streptavidin at the concentration of 10 pM. Specific PNA-modified SiNW-FET sensors have recently been established to diagnose Dengus virus infection.[32, 127] The detection limit of this SiNW-FET biosensor was claimed to be 10 fM. With improved measurements approaches, Liber's group have found that the detection limit for SiNW-FET sensors can be as low as ~0.75 pM in the linear regime to ~1.5 fM in the sub-threshold regime.[128]

The silicon 2D thin films have been studied for biosensors use too. Conde and coworkers[129] reported the use of amorphous Si thin film ISFETs for the label-free detection of covalent DNA immobilization and hybridization. These thin-film transistors can be turned on through a voltage applied to an electrolyte in contact with its dielectric layer, and remain functional after the functionalization of its surface with DNA. The amorphous Si ISFETs were shown to be sensitive to different levels of hybridization. A sensitivity of approximately 50 nM has achieved for the sensor device. The comparison between 1D and 2D silicon materials reveals that the detection limits for 1D SiNWs are typically lower than that of 2D Si thin films, but the

2D Si thin film still showed good sensing performances exhibiting detection limit in nanomoles scale.

In addition, metal oxides have been intensively studied for sensor applications. A typical example is Zinc oxide (ZnO). Many 1D ZnO based biosensors have been reported. Wang et. al.[130] have demonstrated a probe-free and highly sensitive 1D ZnO FET biosensor for detecting biologically and chemically charged molecules. The principle of the srnsor relies on the nonsymmetrical Schottky contact under reverse bias. Owing to the nonsymmetrical Schottky contact configuration, this ZnO sensor had much higher sensitivity than that of the ohmic contact configuration because a few molecules at the junction region can tune the "gate" that effectively changes the conductance. A low detection limit of 2 fg/mL has been demonstrated for hemoglobin with a wide dynamic range from 2 fg/mL to 20 ng/mL.

ZnO 2D nanostructures like thin film, network also have been utilized for biosensor uses. A zinc oxide nanostructured thin film with rough surface has been reported for the detection of cholesterol.[131] Amperometric and photometric studies reveal that the 2D ZnO sensor was highly sensitive to cholesterol over a wide concentration range from 0.12-12.93 mM (5-500 mg/mL). This high sensitivity was attributed to the large surface area of ZnO thin film for effective loading of the cholesterol receptors. Malhotra and colleagues demonstrated a hexagonal ZnO nanocrystalline film for the detection of *M. tuberculosis*.[132] The 2D ZnO thin film exhibited an extremely low detection limit of 1 pM, and a wide detection range from 1 pM to 1uM. This low detection limit was achieved due to the high surface roughness (~3.51 nm) of the 2D ZnO film, which ensured a large surface-to-volume ratio for the sensor.

A summary of typical 1D and 2D materials based biosensors is listed in table 1. These sensors rely on either electrochemical or electrical detection principle. Interestingly, both of the

1D and 2D nanomaterials have excellent sensor performances, showing very low detection limit and wide detection range. Despite that the 1D nanomaterials slightly have better performance than that of 2D nanomaterials in general, 2D nanomaterial biosensors still possess low detection limit at or even less than nanomoles scale, which is comparable to that of 1D nanomaterials. As discussed previously, one key characteristic of nanomaterials is their small dimension. Such small size thus offers very high surface-to-volume ratio, leading to a number of unique physical and chemical properties. Therefore, even with different dimensionality, 2D nanomaterials still have similar or close surface-to-volume ratio with 1D nanomaterials. As a result, the 2D nanomaterials are capable of exhibiting comparable performance to 1D nanomaterials as sensors.

Table 4.1. A summary of 1D and 2D nanomaterials for sensor uses.[32, 127, 129, 130, 132-137]

	Material	Analyte	Detection Details
1D	SWCNT	CgA	100 pM-1 nM
	SWCNT	CEA	10 ng/ml
	SiNW	PSA, CEA	75 fg/ml, 100 fg/ml
	SiNW	Mucin-1	75 fg/ml
	ZnO	Hemoglobin	2 fg/ml, 2 fg/ml-20 ng/ml
2D	Graphene	Glucose	20 pM
	Graphene	Cholesterol	0.5 nM
	Si thin film	DNA	50 nM
	ZnO thin film	DNA	1 pM
	Gold nanoshell	CACNA1F	10 ng/ul

Conducting polymers are an important type of versatile materials for sensing application because they not only possess unique properties but also can be used as immobilization matrices, receptors and in biosensors. In recent years, studies focused on conducting polymer biosensors have shown a trend towards the development of nanostructured conducting polymer biosensors, owing the ability to change the sizes and structures, and hence the properties, of these nanomaterials.

1D conducting polymers, such as nanowires and nanotubes, have attracted a great deal of interest for the design of biosensors. A conducting PANI nanotube array based ultra-sensitive biosensor has been developed for DNA hybridization detection. It demonstrated an extremely high sensitivity of 1.0 fM and good hybridization specificity even at the ultralow concentration of 37.59 fM.[138] Besides, a nanogapped microelectrode-based biosensor array for ultra-sensitive electrical detection of microribonucleic acids (miRNAs) has been realized by the target-guided deposition of PANI nanowires as the in situ signal amplification.[139] The target miRNA can be quantified in a range from 10 fM-20 pM with a detection limit of 5.0 fM.

The 2D conducting polymers biosensors have been reported in literatures as well. For example, an organic thin film transistor glucose sensor with a channel consisting of glucose oxidase immobilized by a spin-coating technique on poly (3,4-ethylenedioxythiophene-poly (styrene-sulfonate) (PEDOT-PSS) conducting polymer film has been reported to have a rapid response time (within 20 s). But the detection limit for the sensor was about 1.1 mM under optimized testing conditions. Moreover, a nanostructured conducting polymer layers based glutamate biosensor for the in vivo measurement of glutamate release stimulated by cocaine was reported.[140] The glutamate micro-biosensor demonstrated a detection limit of 100 nM, a response time less than 10 s, and a wide linear range between 0.2 and 100 uM.

Notably, a unique property for conducting polymers is that they can be easily fabricated via chemical approaches. Therefore the surface roughness of the conducting polymers can be controlled by the synthesis methods. Then it is of interest to compare the sensing performance for the 1D and 2D nanomaterials with similar surface roughness, surface-area-to-volume ratio, and physic properties. As shown in previous, for same materials, the sensors constructed from their 1D and 2D nanomaterials have similar behavior. Therefore comparable sensing

performance is expected for both 1D and 2D conducting polymer nanomaterials. This motivated us to fabricate PANI with the 1D and 2D nanostructures. Because the surface roughness of PANI can be well-controlled, it is highly believed that the 2D PANI nanomaerials would exhibit similar performance to that of the 1D nanomaterial as sensors. In this chapter, the fabrication and characterization of 1D and 2D PANI nanomaterials are studied and their physic properties are compared.

4.2 EXPERIMENTAL

4.2.1 Fabrication of PANI Patterns

The whole PANI patterns fabrication procedure is schematically illustrated in figure 4.1. Au electrodes were patterned and outlined on a wafer by a standard photolithography and lift-off process. The polymethylmethacrylate (PMMA) nanochannels with widths ranging from 200 nm to 50 nm can be created between Au electrode pairs by e-beam lithography. Detailed device fabrication procedures have been presented by our group previously.[52, 53] In this chapter, 100 nm PMMA channels were used as an illustrative case. Before the chemical synthesis, the wafer patterned with PMMA nanochannels was treated with oxygen plasma for 30s to remove the residue inside the nanochannels and to improve the wettability of the surface. This process enhances the adhesion between the PANI film and SiO_2 layer which is a very important factor in later lift-off process. A dilute polymerization method[141, 142] was employed to coat a uniform PANI thin film on the whole wafer. In a typical procedure, a prefabricated wafer was immersed in 180 mL of 0.5 mol/L aqueous $HClO_4$ solution. Aniline monomer (0.91 mL) was then added

into the $HClO_4$ solution and stirred for 30 min at ~0-5 ℃ (ice bath) to form a uniform mixture. In a different beaker, the oxidant, $(NH4)_2S_2O_8$ (APS), was dissolved in 20 mL of aqueous $HClO_4$ solution (the molar ratio of aniline/APS is 3) and cooled to ~0-5 ℃. The polymerization was initiated by combining the two solutions. The mixture was stirred for 4 hrs at ~0-5 ℃ to accomplish the formation of PANI thin film (figure 4.2). After the polymerization, the wafer was taken out from the solution and washed with deionized water to remove adhering PANI precipitate. The green color shown on the wafer upside indicates that a thin layer of PANI film was successfully coated on its surface. Then the PANI coated wafer was dried in vacuum. Finally, the PANI film coated wafer was immersed in acetone for 5 min to dissolve the PMMA layer, and the PANI patterns were obtained by cleaning the wafer with ultrasonication for a few seconds and rinsing it with deionized water 3 times. After the lift-off process, the PANI patterns samples were stored for future use under vacuum conditions.

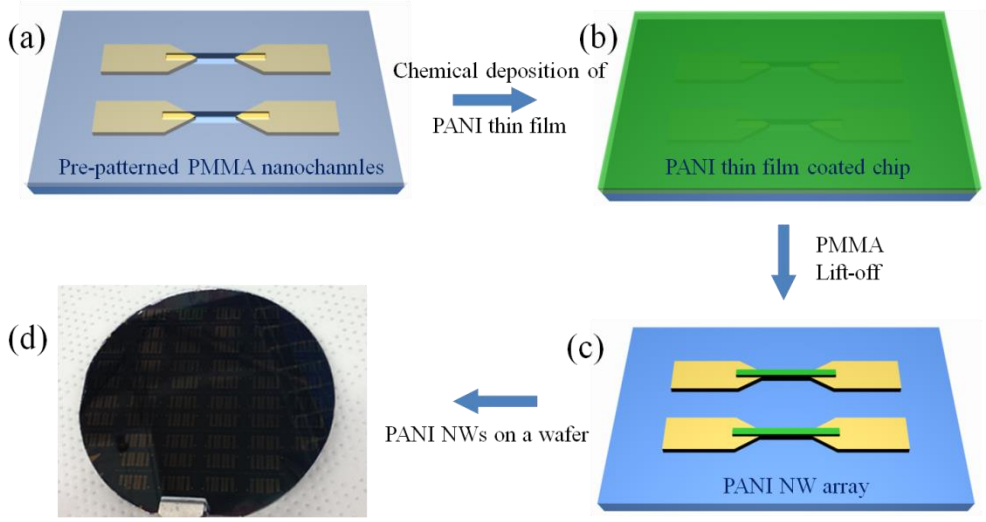

Figure 4.1. Schematic illustration of the fabrication process for 1D PANI-NWs. (a) pre-patterned PMMA nanochannels on a 4-inch wafer. (b) Chemical synthesis of PANI thin film. Polymerization condition: [aniline]=5 mM, [aniline]/[APS]=3, $[HClO_4]$=0.5 M, temperature=~0-5 ℃ (ice bath), stirring of the reaction mixture and reaction time=4 h. (c) PANI thin film coated wafer after the chemical polymerization. (d) PANI-NW arrays after the lift-off process.

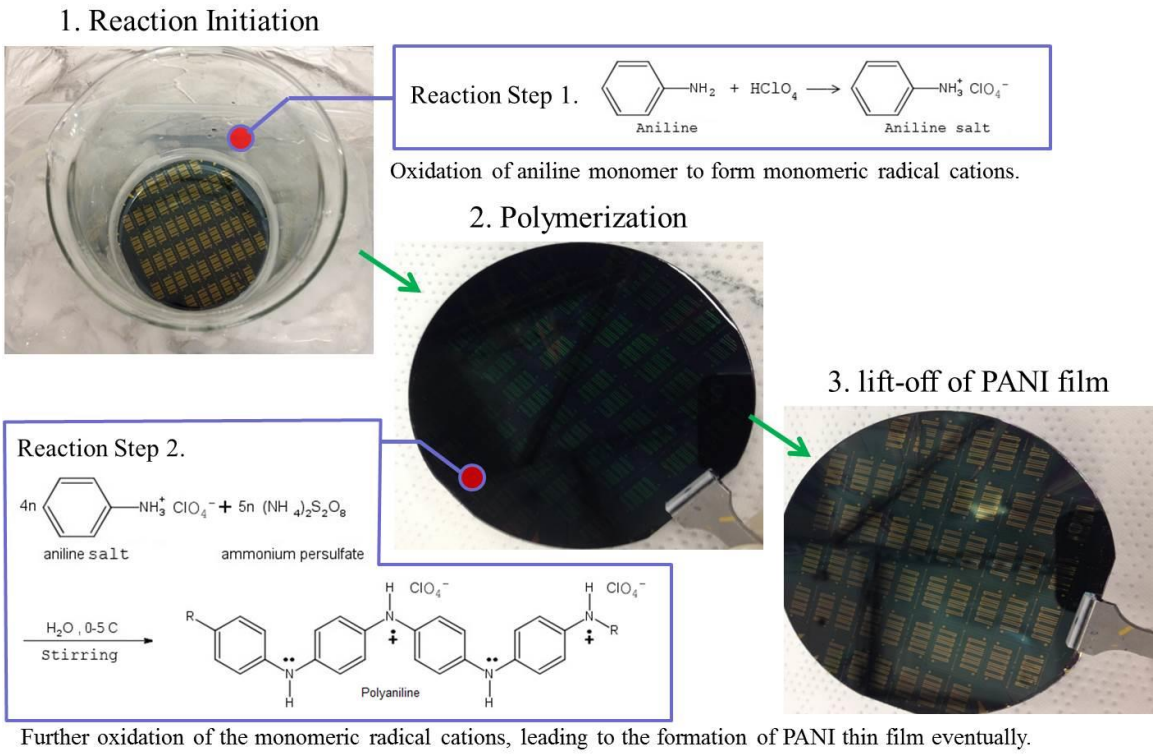

Figure 4.2. The PANI polymerization steps and mechanism.

4.2.2 PANI Patterns Fabrication Optimization

The fabrication method of the PANI NW is the same method introduced in the previous section except the improvement of the lift-off process with a bi-layer photoresist. In the lift-off process for PANI coated e-beam lithographically patterned PMMA nano-channels, retention could occur resulting in the unwanted PANI remaining on wafer. This usually happens when the PMMA is completely covered by PANI film, leaving no gap in the PANI coating for the solvent to penetrate and dissolve the PMMA. To address this and improve the uniformity of the PANI nanowire dimensions, a bi-layer photoresist lift-off process was introduced in the patterning of PMMA nano-channels as shown in figure 4.3. LOR is not photosensitive but is freely soluble in conventional aqueous developers, which makes it an ideal bottom layer. Typically, LOR was

applied on the wafer by spin coating at 4000 rpm for 45 seconds, and baked on hot plate at 195 ℃ for 9 minutes. The PMMA was spin coated on top of the LOR and baked in the oven for 30 minutes. After e-beam patterning, the patterns were developed in MIBK/IPA developer for 60 seconds, the wafer was rinsed with DI water and blown dry with N_2. Afterward, the LOR layer was etched in diluted AZ-400K developer (AZ-400K:H_2O=1:4) for 60 seconds to create an undercut and the wafer was rinsed with DI water and blown dry with N_2 gas. The undercut structure enabled a cleaner lift-off of the PANI film leaving uniform PANI nanowire on the wafer.

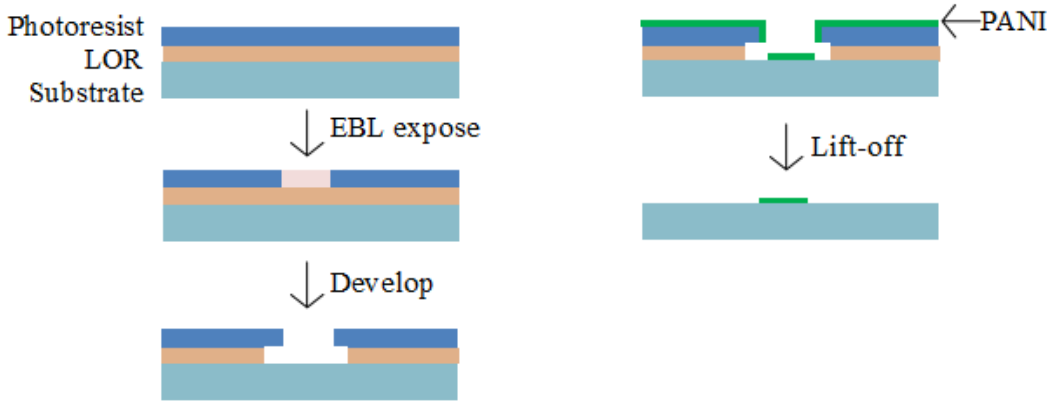

Figure 4.3. Schematic illustration of bi-layer lift-off process.

4.2.3 Characterizations

Optical microscopy and scanning electron microscopy (SEM) were used to examine the PANI-NWs and the electrical properties were measured using a semiconductor device analyzer. The chips containing PANI-NWs were place on a probe station, on which the Au electrodes were connected to semiconductor device analyzer by sharp probes. The resistances of these PANI-NWs were measured at first when they were taken out from vacuum. Then these PANI-NWs

were immersed in to HCl (0.1 M) solution for a short time, and after that, their resistances were measured again.

4.2.4 Biofunctionalization

To prove that the antibody can be successfully immobilized onto the PANI-NWs, a fluorescence labeled antibody was used to functionalize the PANI-NWs. The antibodies were covalently bonded to the PANI-NWs in the presence of 1-ethyl-3-(3-dimethylaminopropyl) carbodiimide (EDC) and N-hydroxysuccinimide (NHS).

Entrapment during polymer synthesis and covalent attachment post polymerization are the two most widely used methods of biofunctionalizing a conducting polymer. The major disadvantages of the entrapment method are a loss of biological activity due to the adverse synthesis conditions and inaccessibility of the biomolecule as it is buried inside the polymer matrix. Covalent functionalization, on the other hand, immobilizes the biomolecule on the polymer surface making it fully accessible for interaction with its complementary target giving higher sensitivity and a faster responding biosensor. For covalent immobilization of biomolecules to conducting polymers, EDC and NHS have been widely employed. Figure 4.4 and 4.5 shows the functionalization and reaction mechanism for covalent biomolecule binding on PANI by EDC/NHS. Briefly, EDC/NHS is first attached to the secondary amine groups on the PANI nanowire or carboxylic groups on the biomolecules and the other end of the linker molecule is attached to the amine groups of the biomolecules or the secondary amine groups on the PANI nanowire surface.

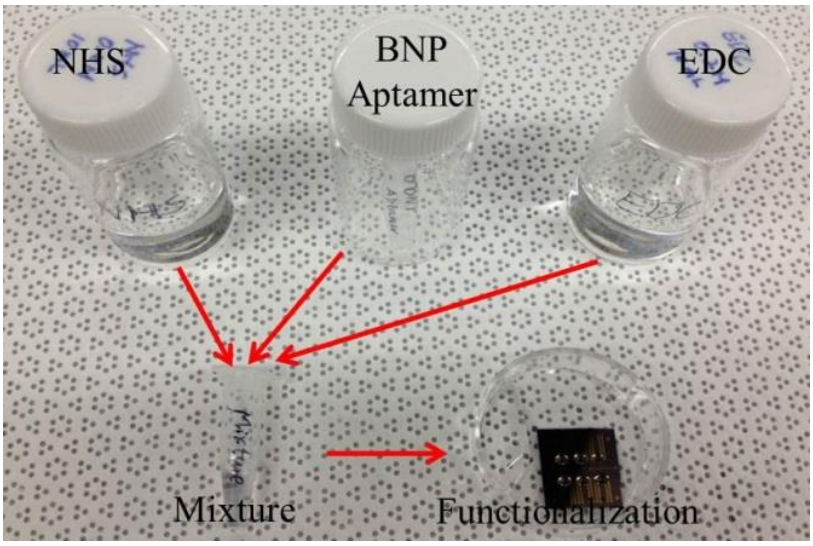

Figure 4.4. The immobilization of aptamers or antibodies onto the surface of PANI nanowires.

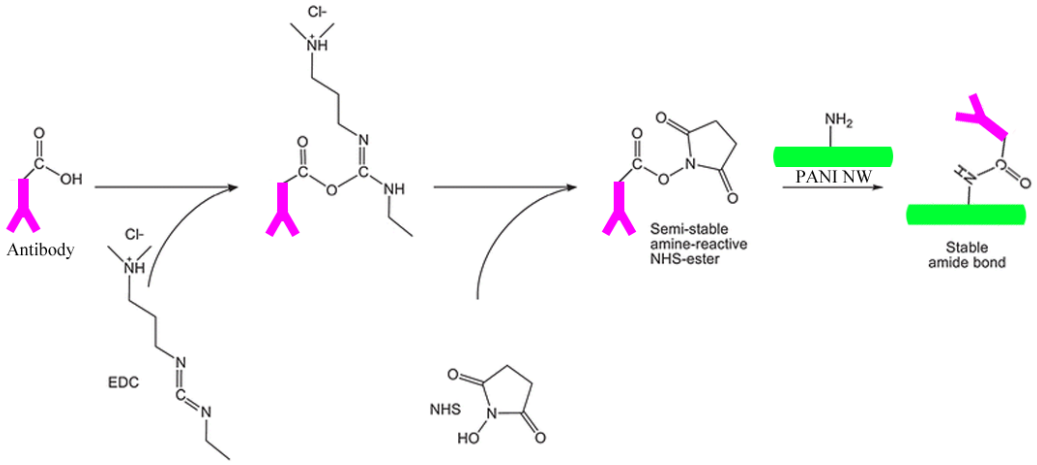

Figure 4.5. The mechanism of using EDC/NHS as linker reagents for the immobilization of antibodies onto the surface of PANI nanowires.

A PBS solution containing 0.1 M EDC, 0.1 M NHS, and 100 μg/mL of the antibody was added onto the PANI-NWs for 3 hours at room temperature for the immobilization. The PANI-NW was then thoroughly rinsed with PBS to remove physically adsorbed antibodies after the immobilization. To prevent possible nonspecific adsorption of other biomolecules to the PANI-NWs, PBS solution containing 200 μg/mL bovine serum albumin (BSA) was then dropped onto

PANI-NWs for 30 minutes to block the free sites on their surface. After the immobilization of antibody, the PANI-NWs were checked by fluorescence microscopy. The functionalization of CK-MB antibody was also executed using the same procedure.

4.2.5 Field-effect Transistor Measurements

Similar to conventional three-probe FET structure, the single nanowire FET structure was established by using two Au electrodes as source and drain electrodes, and instead of using conventional gate, an additional Au electrode was employed as the gate electrode (figure 4.6). For the FET measurements, the gate voltage (V_g) provided by the power supply was applied to the conducting gate, which is separated from the source and drain electrodes, to modulate the current flow through the nanowire. The source-drain voltage (V_{sd}) generated the source-drain current, which is enhanced or quenched upon application of a given gate voltage.

For the biomolecules detection, the entire area of the sensing device was covered with a phosphate buffer saline (PBS) solution containing biomarkers. A chip containing several nanowires was placed on a probe station and connected to a semiconductor device analyzer (Agilent Technologies B1500A) through three probes. A probe was attached to the source, drain, and gate electrodes. The source-drain voltage and gate voltage were provided and controlled by the semiconductor device analyzer, which also collected the source-drain current during the measurements. Typically, the gate voltage was swept from 0.5 V to -0.5 V with a 5 mV sweeping step and the source-drain voltage was scanned from 0 V to 0.5 V with a step of 0.1 V. A baseline of the FET sensor was first acquired by adding a PBS solution onto the sensor, and then the detection signal was obtained by adding PBS solutions containing the target biomarker.

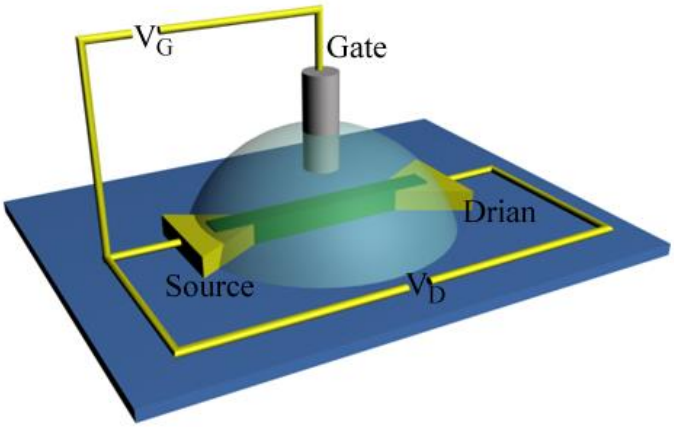

Figure 4.6. Schematic illustration of the PANI-NWs FET measurement with an electrolyte-gate configuration, in which Pt wire is employed as the gate electrode.

4.3 1D PANI NANOWIRES

4.3.1 Morphology

An optical microscope was employed to examine the samples. Figure 4.7a shows the optical micrograph of a PANI thin film coated slide cut from a whole wafer. The slide contains four small chips, and each chip has 16 pre-patterned PMMA nanochannels and 8 Au electrode pair arrays. After the lift-off process the PANI thin film is removed leaving 1D PANI-NWs on the patterned area. Compared to figure 4.7a, the color of the slide changes (figure 4.7b), indicating the completion of the lift-off process. Magnified optical micrographs of the PANI-NWs from different places on one chip are shown in figure 4.7c. Eight PANI-NW arrays (16 PANI-NWs) are fabricated on the chip, and three of them are shown in the figure.

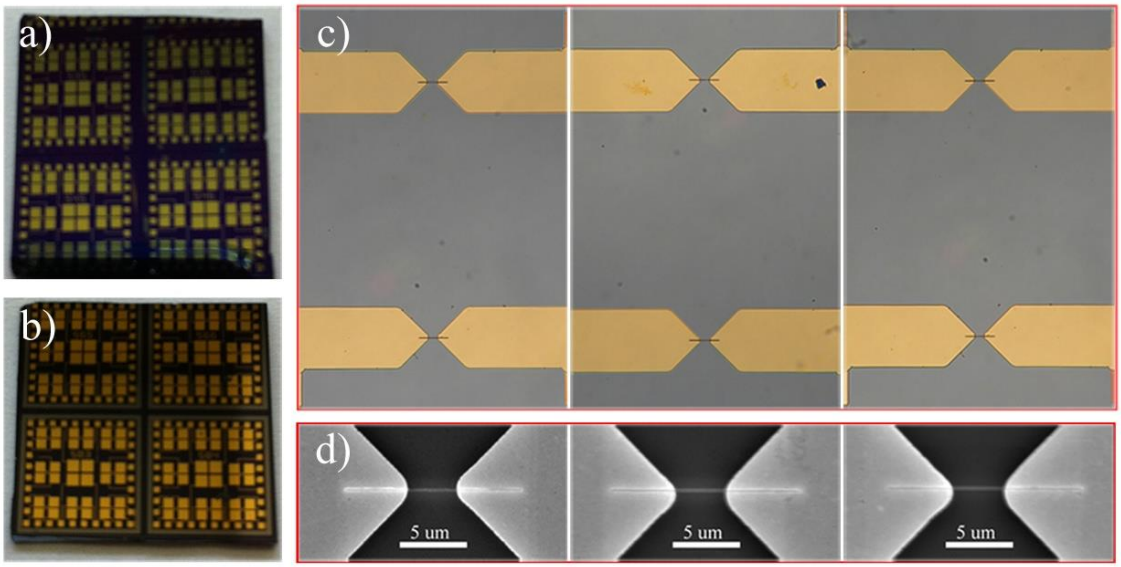

Figure 4.7. (a) Image of a PANI thin film coated slide. (b) Image of a slide after the lift-off process. The different colors showing in (a) and (b) indicates the successful completion of the lift-off process. (c) Optical microscopy images of the PANI-NWs from one chip. (d) SEM images of the PNAI-NWs from different positions of one chip.

Close examination of the PANI-NWs by scanning electron microscopy (SEM) reveals that these PANI-NWs are straight and well-defined. As shown in the SEM images (figure 4.8), the width and the length of the PANI-NWs are about 100 nm and 12 um respectively, which are the same as the dimensions of the PMMA channel. It is important to note that, the heights of the PANI-NWs are determined by the PANI synthesis time and the dimension of the PANI-NWs can be controlled by the pattern sizes and chemical reaction time. Remarkably, the chemical synthesis and lift-off treatment are parallel procedures, thus many wafers can be processed at the same time, which allows high throughput for the production of PANI-NWs.

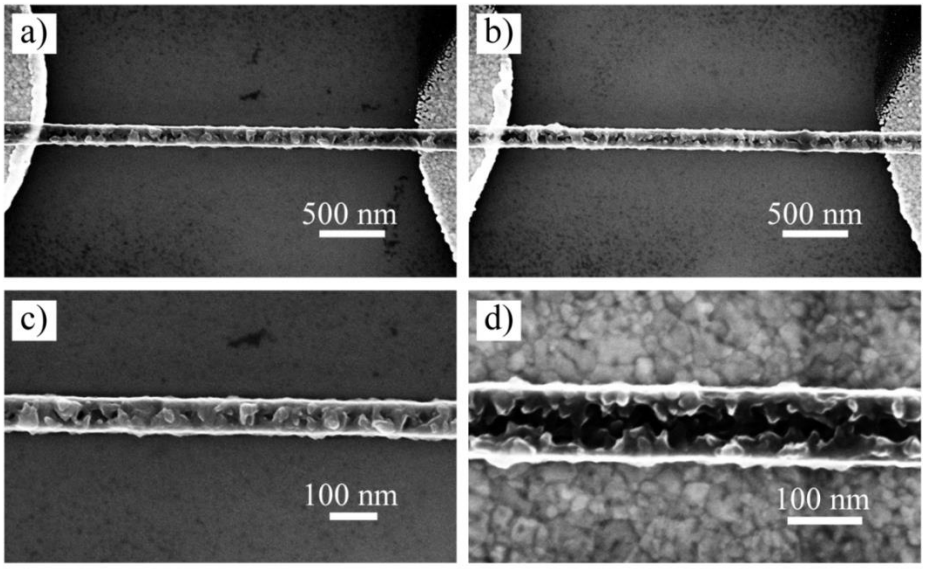

Figure 4.8. SEM images of the PANI-NWs. (a) and (b) SEM images of two different PANI-NWs from same chip. Good uniformity in the dimension of these PANI-NWs can be clearly observed. (c) and (d) The hierarchical structure of the PANI NW are clearly shown in the high magnification SEM images.

The structure of the PANI NWs can be observed in the high magnification SEM images shown in figure 4.8. The SEM images show that the PANI-NWs have two structures including a primary structure (nanowire) and a secondary structure (nanofiber). A top view of the PANI-NWs shows that there are many nanofibers along the NW. The average length of these nanofibers is estimated about 30 nm with diameters of 5 to 15 nm. The diameter of the tip of the individual nanofiber is a few nanometers. Interestingly, the close inspection of the PANI-NWs shows that the nanofibers are grown toward the central axis of the nanowire. This unique hierarchical structure provides much larger specific areas than conventional nanowire structures, thus it is expected to exhibit superior performance in many applications.

Atomic force microscopy (AFM) images (figure 4.9) of a single PANI-NW further confirm its concaved shape. Because of the AFM tip convolution, the NW in the AFM images looks wider than that in SEM images. However, these AFM images still qualitatively reveal the

concaved-shape of the NW. Because of this unusual shape, the NW exhibits a high surface area to volume ratio, which is especially desired in NW-FET biosensors. In general, the detection principle of nanowire-based FET biosensors relies on the field gating effect of charged molecules on the carrier conduction inside the NW. Therefore it is naturally expected that the higher sensitivity could be achieved when a higher surface area to volume ratio between the part of the NW gated by surface charges and the whole body of the NW is obtained. A recent report demonstrated that the sensitivity of NW-FET sensors can be exponentially enhanced in the sub-threshold regime where carriers in NWs have long screening lengths and the field effect of surface charges can gate the whole NW, fully utilizing the high surface volume ratio of NW.[128] In light of this advancement, another potential approach to utilize a higher portion of the NW would be to alter the shape of NW to create more effective surface area. Therefore the higher surface volume ratio of the PANI-NWs owing to their concaved-shape is conducive to increase the portion of the NW that can be gated by the surface charges.

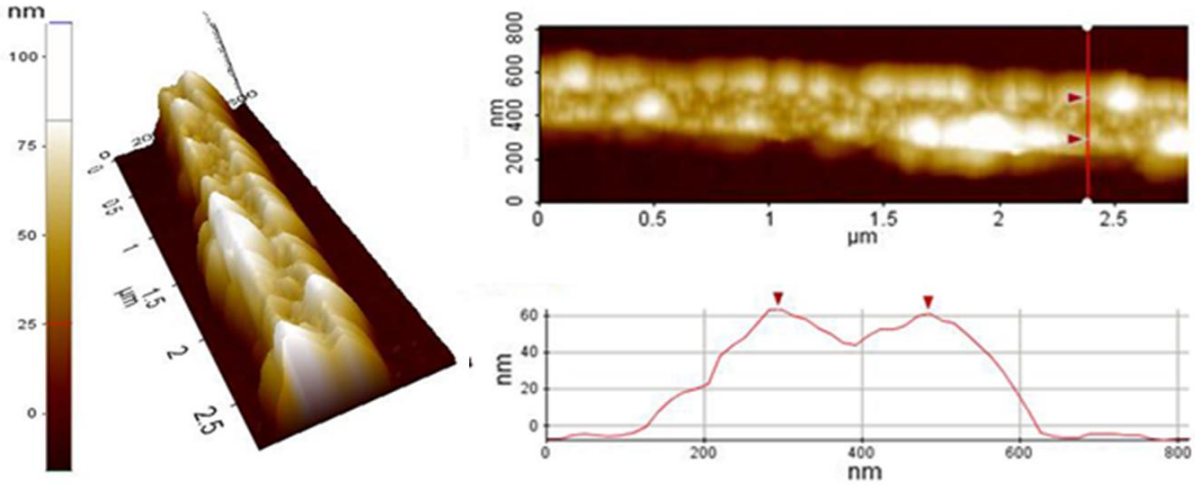

Figure 4.9. AFM images of a single PANI-NW, which details the concave shape of the NW.

For PANI-NWs, its primary structure is defined by the PMMA patterns which are obtained by nanofabrication techniques. On the other hand, its secondary structure is achieved by

a chemical reaction. The combination of nanofabrication and chemistry allows the formation of this unique hierarchical structure. The growth mechanism for the PANI nanofibers has been proposed by other groups,[141, 142] which is similar to a model introduced by Liu *et al*.[143, 144] to address the stepwise electrochemical polymerization of PANI-NW arrays. The solid substrates and bulk solution are two potential nucleation sites for the growth of PANI in chemical oxidative polymerization. These two sites compete with each other thus showing different nucleation rates for PANI. As reported, the polymerization time for PANI is strongly dependent on the concentration of reagents (e.g. aniline monomer, oxidant, and dopant).[145, 146] When concentrated aniline (or oxidant) is used, the nucleation of PANI in bulk solution is at a similar or faster rate than that on solid substrates. In contrast, for dilute concentrations of aniline (or oxidant), heterogeneous nucleation happens first on solid substrates since less energy is required. As a result, most active nucleation sites are generated on the solid substrates at a relatively faster rate when the polymerization is initiated. These active sites would further minimize the interfacial energy barrier for the following growth of PANI on the substrates. Meanwhile, after induction, PANI also simultaneously forms in the bulk solution. The polymerization in the bulk solution consumes some reactive aniline cation-radicals and oligomeric intermediates and in turn suppresses the growth rate of PANI on the solid substrates. The slow polymerization on the substrates only allows PANI to grow from the active nucleation sites generated in the initial stage of polymerization.

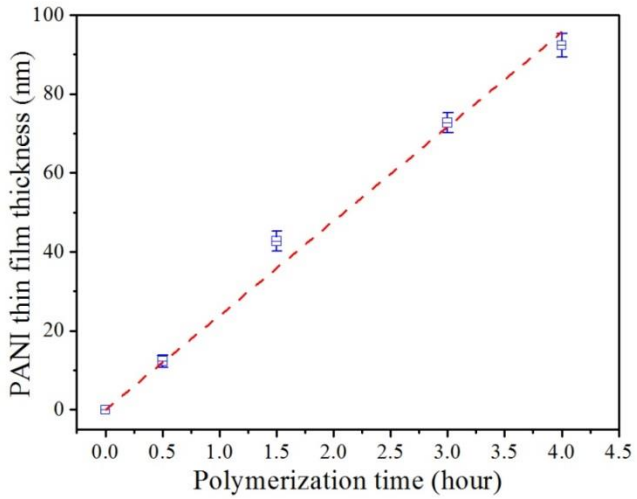

Figure 4.10. PANI thin film thickness versus polymerization time. The film thickness depends linearly on the polymerization time. The thickness of the PANI film was measured by atomic force microscopy (AFM) with non-contact mode. The standard error in each polymerization time was calculated from three samples.

Significantly, an advantage of this chemical synthesis method is the capacity to control the thickness of the PANI film in a simple way. The relationship of the PANI film thickness measured by AFM and the polymerization time is represented in figure 4.10. The linear regression line (dashed line) indicates that the growth rate of the PANI film was kept approximately constant (~24 nm hr^{-1}). Thereby, it is convenient to estimate the thickness of PANI film according to the synthesis time or to obtain PANI thin film with expected thickness by controlling the polarization time.

4.3.2 Patterning Improvement

The NW uniformity on a 4 inch wafer is critical to the quality of the patterned PANI-NWs. Thus the NW shape was examined using microscopy. The PANI-NWs and their position on a wafer are shown in figure 4.11. A total of five positions and of ten PANI-NWs were examined. All

straight and narrow PANI-NWs are well-patterned in between the Au electrode pairs, showing excellent shape uniformity.

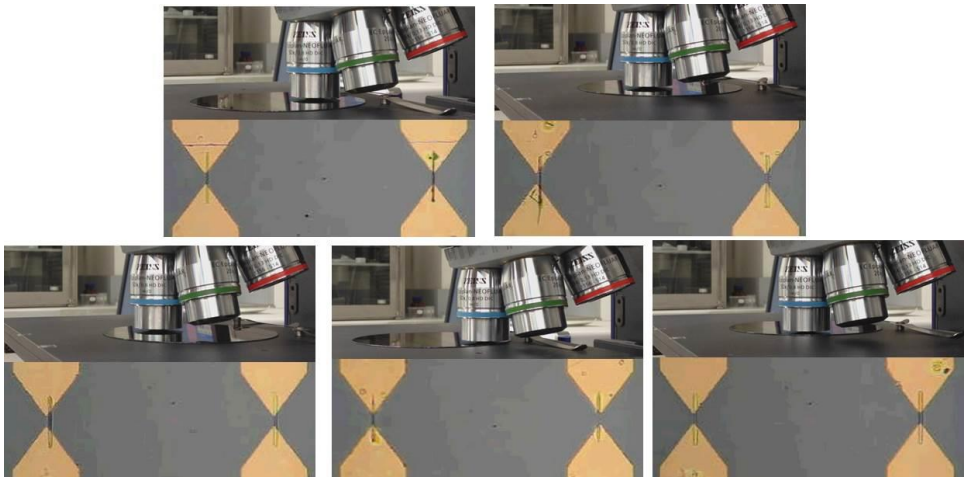

Figure 4.11. Microscopy images of PANI-NW arrays at different positions on a 4 inch wafer. These NWs possessed very good shape uniformity.

Beside the good uniformity achieved by the bi-layer photoresist lift-off process, a good insulation for the FET device was also obtained. Previously, the lack of a bottom layer photoresist caused the gold contacts to be directly exposed to the electrolyte solution when performing the measurements resulting in a very strong leakage current between the gate and source electrodes. Using the bi-layer photoresist lift-off process, only the top layer resist was removed after the lift-off, leaving the bottom photoresist on the surface of the whole wafer. Hence the bottom photoresist played an important role for the electrical isolation among the gold contacts and the solution (figure 4.12). This new device configuration limited the leakage current to a great extent, giving better *I-V* profiles for the PANI-NWs and allowing greater device performance.

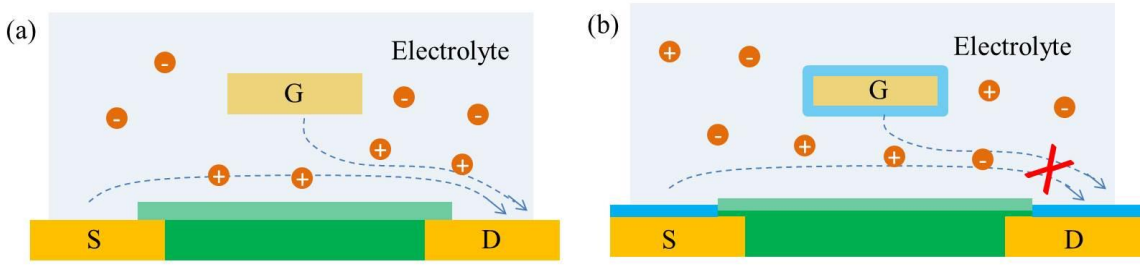

Figure 4.12. (a) Possible current leakages through the electrolyte. (b) The current leakages are limited by excellent insulations.

4.3.3 Uniformity

The uniformity of the PANI-NWs was investigated using a SEM and a semiconductor device analyzer. Rather than the conventional definition for uniformity, which is concerned more about the size of the object, the uniformity of the PANI-NWs includes two aspects: their dimensions and their electrical properties. As shown in figure 4.13, two PANI-NWs from different places on one chip have almost the same size and morphology, showing an excellent uniformity. It is also important to note that even for a single PANI-NW, its width is uniform from one end to the other. Although the fabrication of NWs on large areas can be achieved by many methods, such as self-assembly, nanoimprint lithography, lithographically patterned nanowire electrodeposition, *etc*, uniformly sized structures are rarely obtained. For example, the polymer nanowires formed by self-assembly exhibit low uniformity for single wires because a less controllable solvent annealing is involved in the patterning process,[51] and the metal nanowires fabricated by lithographically patterned nanowire electrodeposition (LPNE)[45] are not straight due to the influence of the contamination on the photolithography. In contrast to these methods, well-controlled e-beam lithography patterning and lift-off techniques, and well-established chemical

polymerization are employed in this report, thus enabling the achievement of highly uniform PANI-NWs.

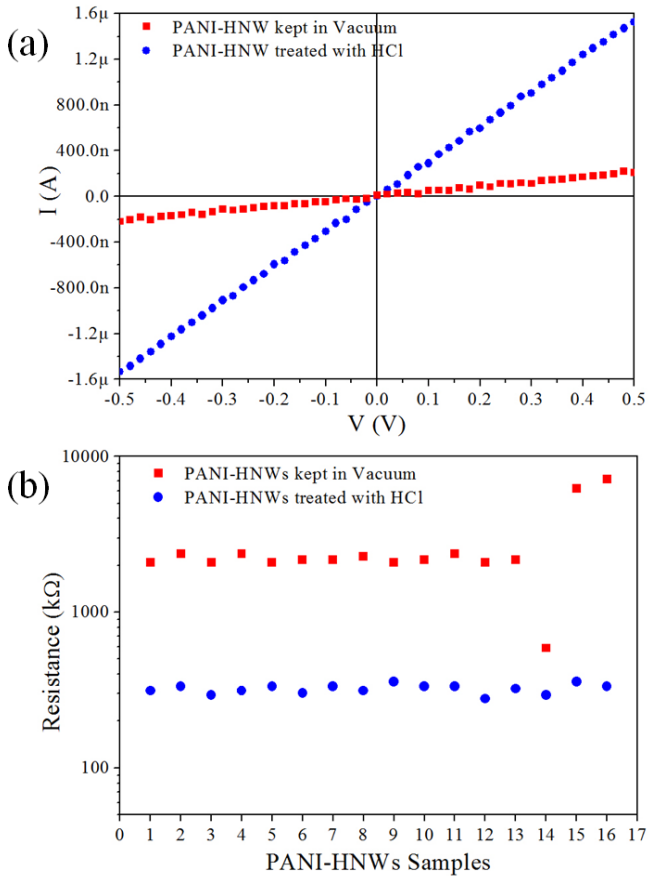

Figure 4.13. (a) *I-V* curves of PANI-NWs kept in vacuum (square) and treated with HCl (circle). (b) Measured resistances of 16 PANI-NWs kept in vacuum (square) and treated with HCl (circle).

Beside their uniform size, the PANI-NWs also exhibited uniform electrical properties. The resistances of 16 PANI-NWs from one chip were measured and are shown in figure 4.13. The first resistance measurements were performed right after the PANI-NWs were removed from a vacuum condition. Then the second resistance measurements for the same samples were carried out after they were treated with 0.1 M HCl solution for five minutes. All of these PANI-NWs were electrically continuous over their entire length no matter if they were kept in a vacuum or treated with HCl solution. After being removed from the vacuum, 13 out of 16 PANI-NWs

showed similar resistances with an average of 2.2 MΩ. After being treated with HCl solution, the resistances of all the 16 PANI-NWs fell into a small range with an average of 320 KΩ. The decrease in the resistance of these PANI-NWs after the acid treatment is caused by the protonation of the PANI.[147] These results indicate that the PANI-NWs have excellent uniformity including not only their sizes but also their electrical properties, which is strongly desired for nanoelectronic device applications.

4.3.4 Fluorescence

The fluorescence microscopy images (figure 4.14) show that the fluorecence labeled antibodies are immobilized onto the surface of PANI-NWs. The nanowires exhibited a red flourescene (bright region) with uniformly distributed over their surface. Remarkably, clear fluorescence can be observed from most of the modified PANI-NWs, suggesting the excellent reproducibility of this covelent surface modification approach.

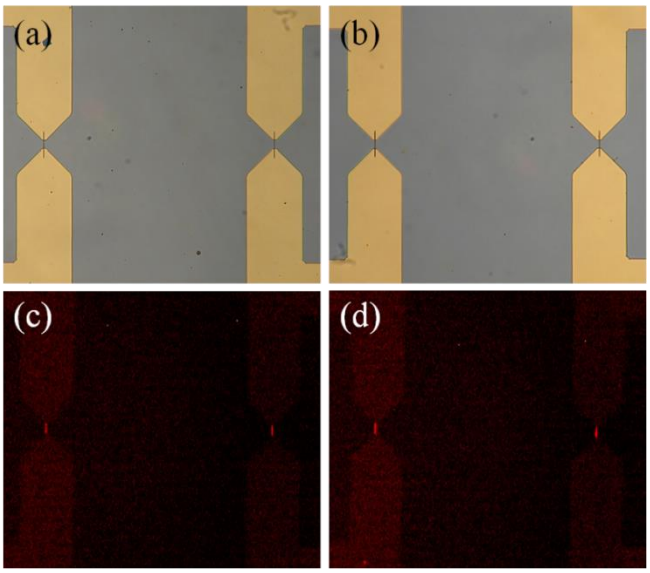

Figure 4.14. Microscopy images (a) and (b) and fluorescence images (c) and (d) of PANI-NWs fabricated by chemical synthesis.

4.3.5 Detection of CK-MB Biomarker

As discussed before, the PANI-NWs have very large specific areas and exhibit excellent uniformity which are advantageous for biosensor applications. The PANI-NWs FET biosensors were demonstrated. Since PANI-NWs are patterned on prefabricated Au electrode pairs, no device post fabrication steps are required. Because detections of most biomolecules are performed in an electrolyte environment, an electrolyte-gate is then employed. Similar to a conventional three-probe FET structure, two Au electrodes serve as source and drain electrodes, and instead of using conventional gate, a platinum (Pt) wire is employed as the gate electrode. The electrical measurements are performed in phosphate buffer saline (PBS) at ambient conditions.

The drain current (I_d) versus drain voltage (V_d) characteristics of a PANI-NW FET obtained as a function of different gate voltages (V_g) are shown in figure 4.15a. The value of I_d rises upon increasing negative V_g to a positive V_d. This phenomenon is consistent with prior measurements performed on polyaniline nanowires.[148, 149] Under similar conditions, but applying a positive V_g, a very weak gate modulation for this PANI-NW FET is observed which indicates that the n-channel transport mechanism does not function in the PANI-NW FET in PBS solutions. These results indicate that the PANI-NW is an excellent p-type material.

To realize a PANI-NW-based biosensor, a creatine kinase (CK)-MB antibody is selected as the bio-recognition element for the proof-of-concept demonstration of detecting CK-MB biomarker by a PNAI-HNWs FET biosensor. CK-MB is a standard cardiac biomarker for the diagnosis of acute myocardial infarction (AMI).[150] Detailed immobilization procedures can be found in our previous reports.[151]

Figure 4.15b shows the PANI-NWs FET sensor responses to the introduction of CK-MB and BSA collected at V_d=0.4 V and V_g=-0.4 V in ambient conditions. As expected, addition of the BSA to the sensor only caused a minor response even though a relevant high concentration of BSA solution (50 ng/mL) was used. This result shows that this biosensor does not respond to a non-specific target, thus exhibiting a very good specificity. In contrast, the introduction of the specific target CK-MB led to a significant increase in drain current (about 10% change referring to the base line) within a very short response time (40 s) despite the concentrations of CK-MB being very low (1 ng/mL). This drain current increase is possibly attributed to a chemical gating effect on the PANI-NW resulting from the specific binding event.[152] The PBS solution of pH 7.4 caused the CK-MB molecules to be negatively charged because it is higher than the isoelectric point of the CK-MB (pI=5.2–5.8). Therefore, the specific binding of the CK-MB and its antibody could induce a chemical gating effect, which in turn leads to the increase in drain current. As the concentration of CK-MB increased to 5 ng/mL and 50 ng/mL, the drain current of the sensor correspondingly increased by 17% and 29%, respectively. Remarkably, the clinical cutoff level for CK-MB is about 3.5-10 ng/mL,[153] which falls into the detection range of this PANI-NWs FET sensor, thus demonstrating that this sensor is a promising candidate for clinical use.

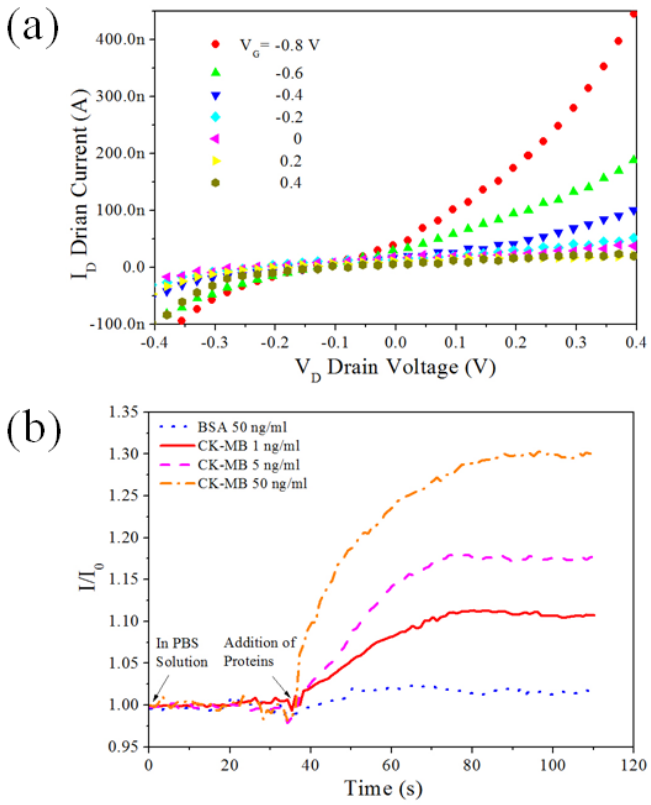

Figure 4.15. (a) I_d-V_g at different V_d for PANI-NWs FET. (b) Real-time detection results of CK-MB using PANI-NWs FET biosensor.

4.4 2D PANI NANOBELTS

4.4.1 Morphology

The patterning process for 2D PANI nanobelts was similar to what was used for the fabrication of PANI-NWs except the photolithography steps. The electrode layout was simplified, which has a common source and common gate for the sensor device. The gaps between the source and drain electrode were designed to be 10, 50, and 100 microns. Although the length and width of

the 2D PANI are at the micro-scale, the PANI thickness was still kept ~100 nm by controlling the PANI thin film deposition time.

Five kinds of patterns with different dimensions (length/width=10, 5, 1, 0.2, 0.1) were patterned on the electrodes for the purpose of studying the optimal pattern for sensor devices fabrication and tests. The microscopy images of patterned 2D PANI nanobelts are shown in figure 4.16. The PANI nanobelts were patterned between the source and drain electrodes with very sharp edges and well-controlled dimensions. This pattern technique ensured excellent contacts between the wire and the electrodes. The low magnification microscopy images of the PANI nanobelts in figure 4.17 clearly show the good shape uniformity of the patterns for each dimension.

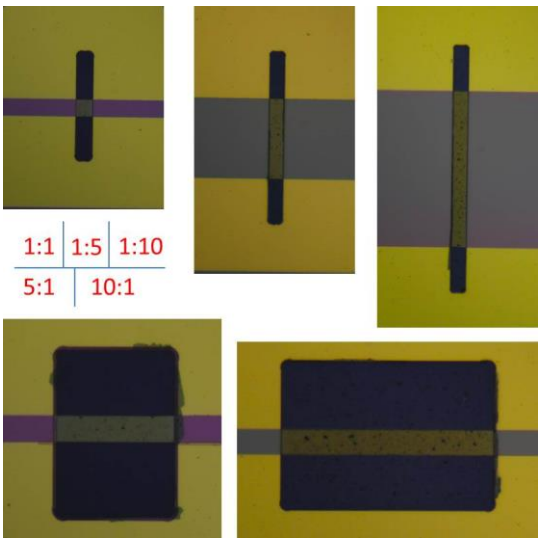

Figure 4.16. Five different dimensions (L:W=10, 5, 1, 0.2, 0.1) of the PANI patterns were designed to optimize the fabrication process and the following sensing tests.

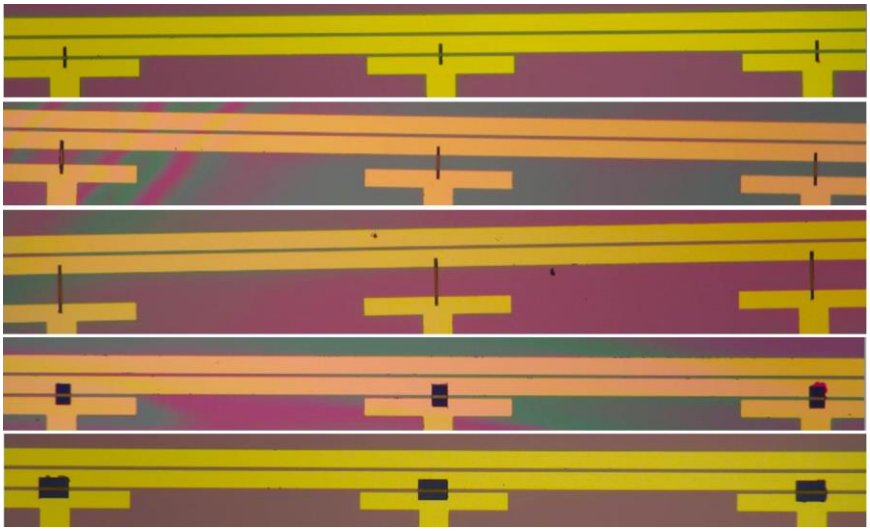

Figure 4.17. Low magnification microscopy images of the patterned PANI nanobelts, which showed a good uniformity of the patterns.

The details of the nanobelts surface can be observed from the SEM in figure 4.18. As shown, the nanobelts had very bright edges which suggest that the edges were thicker. Close examination of the PANI nanobelt revealed that there were many white dots on its surface. The SEM image of the surface at high magnification showed that the PANI nanobelt surface was as rough as the surface of PANI-NWs. The rough surface was achieved by the PANI thin film deposition method as explained previously. Significantly, the rough surface is advantageous to the sensor devices because it allows ultrahigh surface area to volume ratio and abundant surface area for the binding of biomolecules.

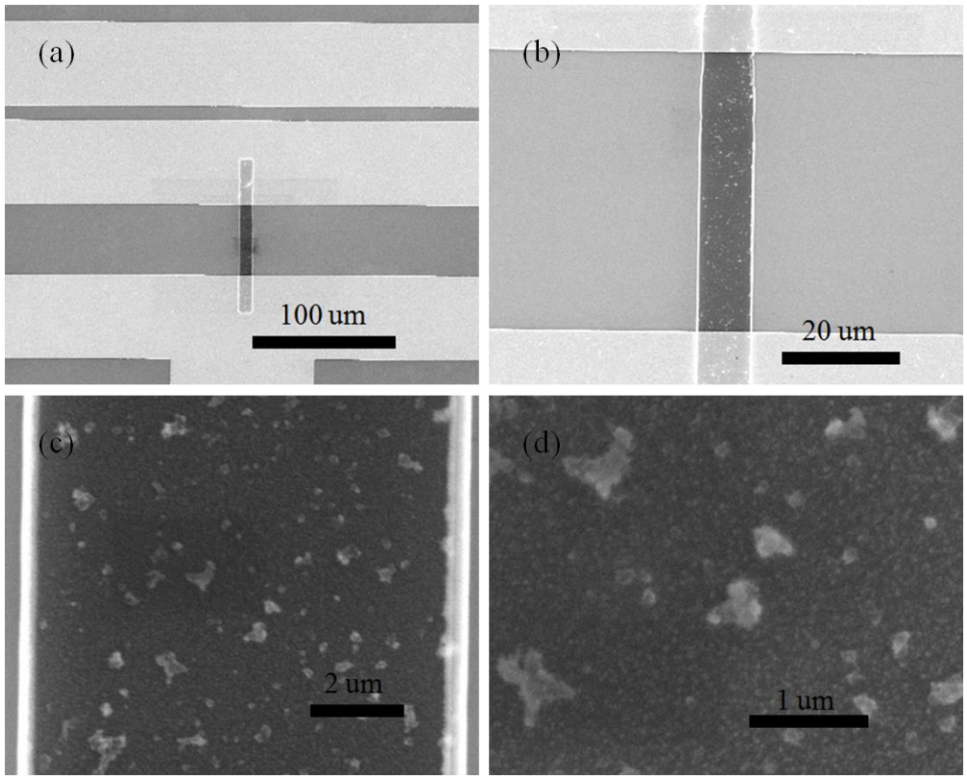

Figure 4.18. SEM images of a photolithographically patterned PANI nanobelt.

The topography of the 2D PANI nanobelt surface was studied by AFM at non-contact mode. It can be clearly observed that the film thickness was about 100 nm. The thickness is consistent for PANI-NWs fabricated under the same conditions. The AFM image (figure 4.19) also showed that the edges of the PANI nanobelt were higher than its other parts. The edges were about 600 nm height. The rough surface of the PANI was also observed from the AFM image. The diameter of grains on the PANI nanobelt surface was about 10 nm. These results confirm that the 2D PANI nanobelts have a rough surface and a high surface to volume ratio. These features were also observed from the 1D PANI NWs. Hence it is natural to expect that the 2D PANI nanobelts based sensors would have comparable performance to PANI-NWs sensors.

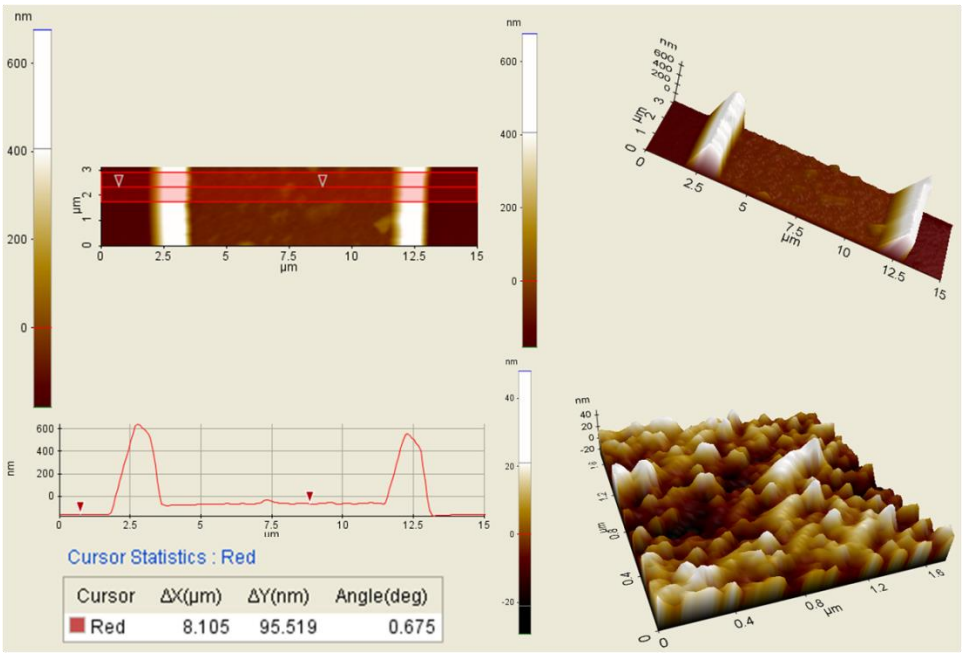

Figure 4.19. The AFM images of a 2D PANI nanobelt patterned by photolithography process.

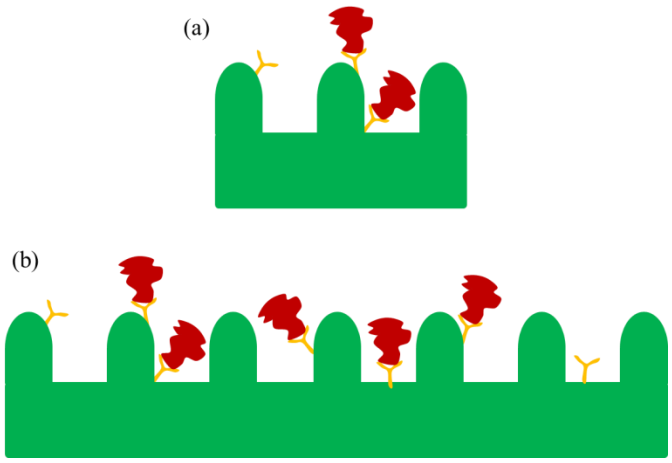

Figure 4.20. The rough surfaces of the (a) 1D PANI-NW and (b) 2D PANI nanobelt provide abundant sites for the functionalization of antibody, giving similar antibody density on both wires. Therefore, the 2D PANI nanobelts are expected to have comparable sensing performance than the nanowires.

In fact, the rough surface of the PANI film is one significant feature that could give the 2D PANI nanobelts similar performance as the PANI-NWs. For both PANI nanostructures, only the upper surface of PANI is exposed to the solution and can be modified with antibodies. The

rough surface provides a large amount of binding sites for antibodies. Since the same functionalization method was used, the 2D PANI nanobelts should have similar antibody densities to the PANI-NWs (figure 4.20). Therefore, for the same target concentration, the 2D PANI nanobelts are able to capture more targets because more antibodies are available. As a result, this compensates for the effect of the dimension of the PANI nanobelts in some extent and gives the 2D PANI nanobelts comparable performance with the PANI-NWs.

4.4.2 Resistance

The resistances of the 2D PANI nanobelts were measured with a probe station and semiconductor analyzer. The resistances of PANI nanobelts with 10×10 um dimension are shown in figure 4.21. Five different nanobelts from different parts of a wafer were measured. The resistances of these wires were about ~6 kΩ. The resistances of PANI nanobelts with other dimensions were listed in table 4.1. As shown, the resistances of PANI nanobelts with the same dimensions at different spots on the wafer were identical, indicating the good uniformity of these wires.

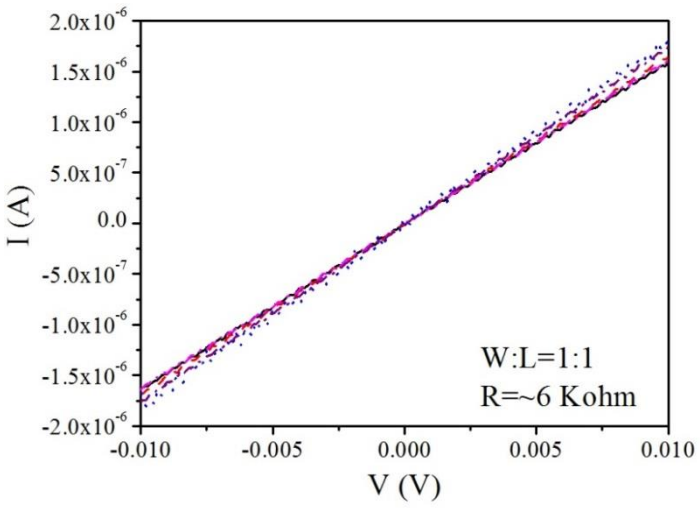

Figure 4.21. The resistance of five 10×10 um PANI nanobelts on a 4 inch wafer.

Table 4.2. The resistances of PANI nanobelts with different dimensions at different positions on a wafer.

W:L (Kohm)	10:1	5:1	1:1		1:5	1:10
			Left	Middle		
Top	1.56	0.8	6.0	6.12	22.06	38.46
Middle	1.48	0.82	5.88	6.0	21.43	41.10
Bottom	1.47	o.83	6.06	5.77	20.98	38.96

4.4.3 FET Measurements

The FET measurements of these 2D PANI nanobelts were performed using an electrolyte-gate configuration descried previously. The drain current (I_d) versus gate voltage (V_g) characteristics of a PANI nanobelt FET obtained as a function of different drain voltages (V_d) are shown in figure 4.22a. The value of I_d increased upon increasing negative V_g at positive drain potentials. Notably, higher drain currents can be obtained as the drain potential becomes more positive. As shown, the nanobelt was off when the gate bias was more positive than -0.6 V. As the gate bias went more negative than -0.6 V, the drain currents from the nanobelt were exponentially

increased. This phenomenon is consistent with the prior measurements performed on PANI NWs. The threshold voltage was about -0.6 V for the PANI nanobelt. In addition, no current leakages were found from these results, indicating that the additional PR layer played an important role in eliminating the leakage. These results confirmed that the 2D PANI nanobelts are an excellent p-type material.

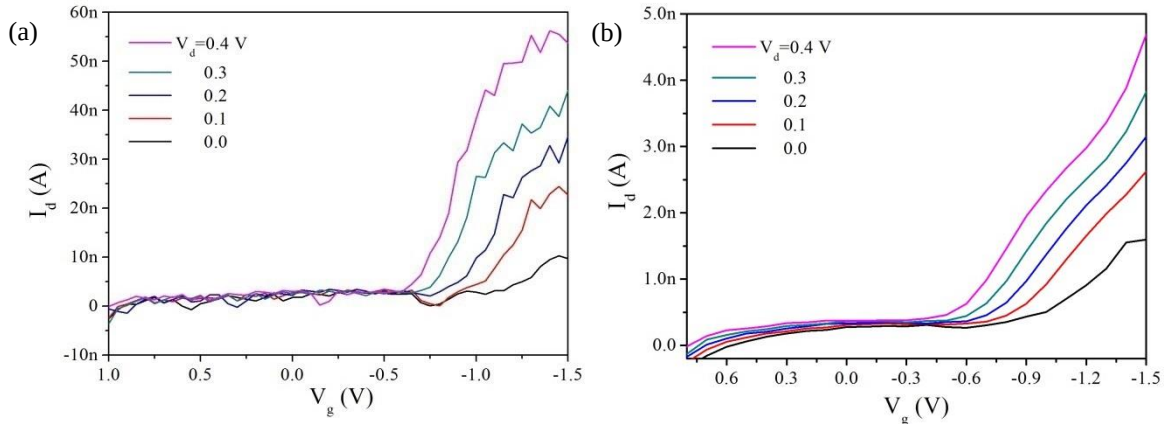

Figure 4.22. I_d-V_d curves of a (a) 2D PANI nanobelt and (b) 1D PANI nanowire in 0.1x PBS solution. The 2D PANI nanobelt showed comparable FET behavior with the nanowire.

The *I-V* curve of a PANI-NW in 0.1x PBS solution is also given in figure 4.22b for comparison. Clearly, at the same measuring condition, the PANI-NW had less drain current. For a FET device, its drain current in the linear region is proportional to W/L, where W and L are the width and length of the gate electrode, respectively. Therefore, the drain current of PANI-NW was less than that of the 2D PANI nanobelts in the linear region because the PANI-NW has smaller W/L ratio. Compared to the drain current of the PANI-NW, the 2D PANI nanobelts had relatively larger drain currents but still on the order of nano-amps. This comparison reveals that the 2D PANI nanobelt maintains a good field-effect transistor.

4.5 CONCLUSIONS

In conclusion, we presented a novel approach that combines top-down (nanofabrication) and bottom-up (chemistry) techniques to enable the simple and facile fabrication of PANI patterns with high throughput and uniformity. The chemical synthesis and subsequent lift-off process facilitate the mass production of PANI patterns on large areas. The lithography technique is not only capable of controlling the dimension of the PANI patterns but, also enables excellent uniformity seen in the shapes of the patterns. These PANI patterns also showed very good uniformity in their electrical properties. The FET studies on these PANI-NWs indicated that they are an excellent p-type material with an electrolyte-gate configuration. A proof-of-concept demonstration of this electrolyte-gate PANI-NWs FET sensor for the detection of CK-MB was also performed. This sensor showed very specific and rapid responses to the target with a very low detection level of 1 ng/mL. Importantly, the clinical cutoff level of CK-MB falls into the detection range of this sensor, demonstrating the potential use for clinical diagnosis. The method introduced here explores advantages of nanofabrication and chemical synthesis, and provides an easy way to produce hierarchical nanowires with controlled dimensions, and can potentially be applied to prepare other hierarchical nanostructures.

The fabrication of 2D PANI nanobelts using a photolithography technique was achieved to reduce the cost for device manufacturing. These PANI nanobelts possessed excellent uniformity. The study of the morphology and topography of the nanobelts with SEM and AFM showed that these wires have very rough surfaces. As a result, the 2D PANI nanobelts are capable of providing large surface for the functionalization of antibodies. The resulting FET behavior of the 2D PANI nanobelts was similar to that of 1D PANI-NWs. Thus it is expected that the 2D PANI nanobelts would have comparable sensing performance to that of PANI-NWs.

5.0 ULTRASENSITIVE PANI FET SENSORS FOR BNP DIAGNOSIS

5.1 INTRODUCTION

B-type natriuretic peptide (BNP) is one of the most important cardiac markers for the prediction and diagnosis of heart failure.[74] It is well-known that when a patient's heart failure symptoms begin or worsen, the ventricles in the heart secrete BNP, causing an elevated level of the marker in the blood. In general, the greater the BNP level in the blood, the more severe the condition. The blood BNP concentration under normal conditions is ~20 pg/mL (6 pM), and it increases to ~2 ng/mL (600 pM) for patients diagnosed with severe congestive heart failure.[154] The BNP concentration is extremely low in blood, so conventional BNP detection techniques usually require expensive instruments such as a photomultiplier or excitation light source. Recently, electrochemical and optical biosensors were used to measure BNP. An electrochemical enzyme immunoassay was reported for the detection of BNP with a detection limit of about 20-40 pg/mL, but the detection time took up to 2 hours.[73] One year later, a surface plasma resonance sensor system was developed by the same group for BNP detection.[74] While they reached a very low detection limit (~5 pg/mL), the SPR sensor requires sophisticated optical instruments which raises the cost for detection. Since it is suggested to monitor the BNP biomarker on a regular basis for those at an elevated risk of heart failure so that a negative event could be detected a

prior, biosensors that can detect trace levels of BNP in real time with a fast response and low cost are highly desired.

In past decades, diverse electrical biosensing architectures have been developed such as amperomertric, conductometric, and field-effect transistor (FET) biosensors. Among them, FETs have generated much attention because they offer rapid and sensitive detection of the interaction events between the target biological molecules and the receptors on its surface.[30] In a typical FET configuration, current flows along a semiconductor channel connected to the source and drain electrodes. The conductance of the semiconductor channel is tunable by controlling the bias on the gate electrode. In traditional complementary metal-oxide-semiconductor field-effect transistors (MOSFET), the conducting channel is implanted inside the bulk substrate and isolated from the gate electrode by a thin insulator layer. Conversely, in FET-based biosensors, the channel is in direct contact with the electrolyte or solution and that allows better control over the charges introduced onto the semiconducting channel surface. The net charges on the surface can change the surface potential on the semiconductor channel which can alter the channel conductance. This implies that FET-based biosensors might be very sensitive to the biological binding events on the channel surface. Therefore it is natural to expect that ultrahigh sensitivity of nanowire based biosensors could be achieved when the maximum effective charges on the channel surface and induced carrier density in the semiconductor channel are obtained.

These scenarios can be realized when the ion/charge screening effects are well controlled. Ion/charge screening effects have been qualitatively studied in chemistry and physics. The research has concentrated on the influence of the screening mechanisms of dissolved ions in electrolyte and the carrier density in the semiconductor channel. It was found that the effective surface bound charges in an electrolyte solution can be significantly affected by the electrical

double layer formed by the ions.[3] This effect has a significant impact on the sensing performance of FET biosensors and it is known as Debye screening on a certain length scale, termed as the Debye length (λ_D)[3,4] in solutions. For aqueous solutions at room temperature, this length is given by

$$\lambda_D = \frac{1}{\sqrt{4\pi\lambda_B \sum_i \rho_i Z_i}} \qquad (1)$$

where λ_B is the Bjerrum length of the medium, and ρ_i and Z_i are the density and the valence of the *i*-th ionic species. Another screening effect in the semiconductor is known as Tomas-Fermi screening (also call Debye length in semiconductor, Tomas-Fermi screening is used to distinguish the Debye length in electrolyte) has strong effect on the induced carrier density. This Tomas-Fermi screening length L_D is given by

$$L_D = \sqrt{\frac{\varepsilon_0 k_B T}{q^2 N_d}} \qquad (2)$$

where ε_0 is the dielectric constant, k_B is the Boltzmann's constant, T is the absolute temperature in kelvins, q is the elementary charge, and N_d is the density of dopants.

In this chapter, the use of PANI FET biosensors for BNP detection in buffer solution and real samples are investigated. The sensor performances in sensitivity, dynamic detection range, and response time are evaluated. The sensing mechanism for the PANI FET sensors is studied as well. As the impacts of Debye-length to the PANI FET biosensor performance are investigated in details. The tuned PANI Debye length greatly improves sensor performance. In order to improve the PANI patterning quality and insulation, a bi-layer lithography pattern technique is introduced. Furthermore, an integrated biosensor system is developed based on the PANI FET sensors. The system is carefully evaluated with the tests of real BNP samples.

5.2 EXPERIMENTAL

5.2.1 BNP Sensing Measurements

The detections of BNP biomarker in phosphate buffer saline (PBS, pH=7.20) were investigated by using the PANI-NW FET microfluidic biosensors. A microfluidic chip containing PANI-NWs was placed on a probe station and connected to a semiconductor device analyzer (Agilent Technologies B1500A) through three probes. A probe was attached to the source, drain, and gate electrodes. The source-drain voltage and gate voltage were provided and controlled by the semiconductor device analyzer, which also collected the source-drain current during the measurements. For typical FET measurements, the Au electrodes connected to the NW were utilized as source and drain electrodes, another Au electrode was used as the gate electrode. A PBS solution was flowed into the microfluidic channel at first. In the meanwhile, the drain current (I_d) of the NW was monitored by sweep the gate voltage (V_g) from 0.5 V to -0.5 V with a drain bias (V_d) of 0.5 V. Then another I_d-V_g measurement was performed after BNP solution was pumped into the microfluidic sensor. All the measurements were carried out at ambient conditions. For the BNP detections in whole blood samples, the BNP purchased from Sigma-Aldrich was spiked in normal human blood. The normal human blood was provided by the UPMC Cardiovascular Institute. An identical setup and method were used in the BNP detection in PBS solutions, however, the applied drain and gate voltages were altered.

5.2.2 Sensing Mechanism Measurement

Two PBS solutions with different pHs (7.2 and 4.75) were used for the study of the detection mechanism of PANI-NWs FET sensors. The same measurement procedure as the BNP detection was used. All the tests were taken in ambient conditions.

5.2.3 Debye-Length Tests

To investigate the effect of Debye length to the detection of BNP using our NW-FET sensor, the measurements were performed in dilutions of PBS. These dilutions were made relative to 1x PBS, which contains 150 mM NaCl, 3 mM KCl, and 10 mM phosphate salts. The calculated values of λ_D for the five diluted solutions 1x, 0.5x, 0.25x, 0.1x, and 0.05x PBS are 0.7 nm, 1.04 nm, 1.47 nm, 2.3 nm, and 3.3 nm, respectively. The NW-FET sensors were functionalized with a BNP aptamer. For the NW-FET measurements, the Au electrode pair connected with the NW was used as source and drain electrodes and another Au electrode was employed as the gate electrode. The drain current (I_d) was monitored by sweeping the drain voltage (V_d) from -1 V to 1 V with a gate bias of -0.25 V. The measurements were performed at ambient conditions.

5.2.4 2D PANI Nanobelts for BNP Sensing

A single chip containing 12 PANI nanobelts cut from a 4 inch wafer was shown in figure 5.1. A microfluidic replica with two microfluidic channels was placed on the chip with strong adhesion to seal the microfluidic and the chip. This completed the microfluidic sensor fabrication. The tests of the BNP detection using a potentiostat based biosensor system were carried out in

ambient conditions. The PANI belts were functionalized with BNP antibodies. And then 0.1x PBS, BNP in PBS with different concentrations, and nonspecific targets (Myo, CK-MB, etc.) solutions were used for the drain potential sweeping tests and the gate bias.

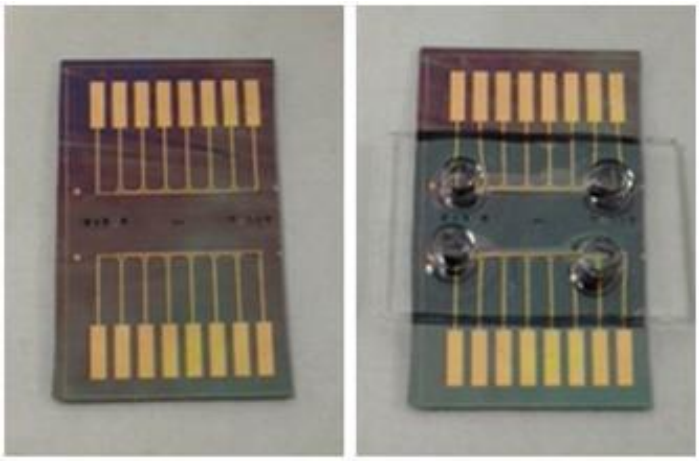

Figure 5.1. Microscopy Images of a 2D PANI nanobelts patterned chip and a microfluidic integrated sensor chip.

5.3 RESULTS AND DISCUSSIONS

5.3.1 BNP Detections in Buffer Solution

The BNP aptamers functionalized PANI-NWs were employed for the detection of BNP for demonstration. Figure 5.2 shows the real-time measurement of normalized responses (I_d/I_{d0}) from the surface modified PANI-NWs FET sensors responding to BNP with increasing concentration in PBS solutions. The specificity of the PANI-NWs was tested by introducing a 100 ng/mL bovine serum albumin (BSA) in PBS solution to the FET sensor. No significant change was observed from the curve shown in figure 5.2. In contrast, when BNP solutions were

added to the FET sensors, considerable changes were observed. These results indicate that the FET sensor has a very good specificity.

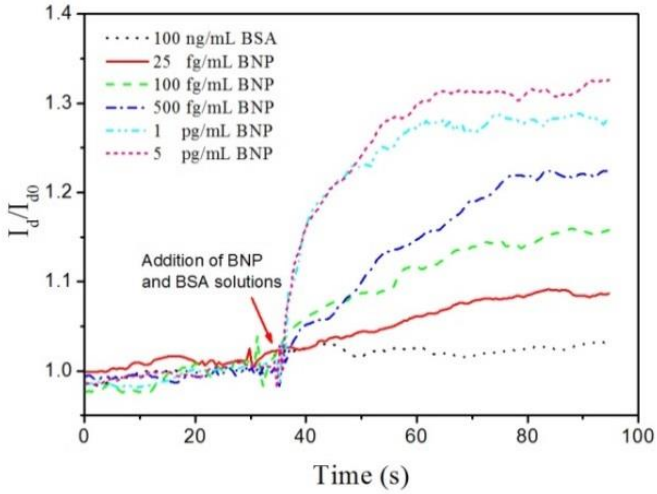

Figure 5.2. Real-time detection of BNP with increasing concentration in PBS solution using PANI-NWs FET biosensors (V_g=-0.5 V, V_d=0.5 V).

The binding of BNP through the strong interaction between BNP and its aptamer on the surface of the PANI-NWs resulted in the increase of I_d. The drain current began to increase right after the addition of BNP and rapidly reached a stable value within 1 minute. The lowest BNP concentration of 25 fg/mL was detected with a ~10% increase in I_d. When the BNP concentration was progressively increased to 100 fg/mL, 500 fg/mL, 1 pg/mL, and 5 pg/mL, consistent increases in I_d of ~17%, ~22%, ~28%, and ~32% were observed respectively.

Figure 5.3a shows the typical plot of the drain-source current versus gate voltage of the PANI-NWs FET in PBS buffer solution. The drain current I_d rises upon increasing negative V_g at positive drain-source voltage (V_d), indicating a p-type behavior of the PANI-NWs FET devices. Upon the addition of a high concentration of the nonspecific target molecule BSA, no I_d changes were observed, while the sensor showed significant increase in I_d upon the addition of BNP

solutions, indicating the good specificity of this sensor. When the BNP concentration was progressively increased, consistent increases in I_d were also observed.

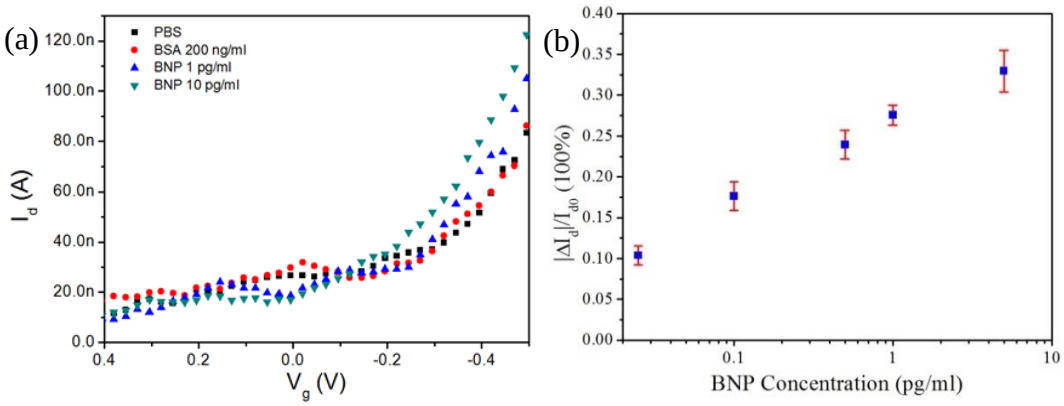

Figure 5.3. (a) I_d-V_g curves of the PANI-NWs to different solutions. It is clear that the sensor shwoed nearly non response to the non-specific target, but significant changes to BNP targets referring to the PBS background. (b) Plot of BNP concentration versus the current change, the data were collceted forn three samples for each concentration.

Figure 5.3b shows the plot of normalized changes of drain current as a function of the BNP concentration. The PANI-NWs exhibited a wide dynamic sensing range from 25 fg/mL to 5pg/mL. The lowest detectable BNP concentration of 25 fg/mL is much lower than that obtained by the surface plasma resonance sensor (5 pg/mL). This ultrahigh sensitivity and low detection limit can be ascribed to the unique concaved-shape of the PANI-NWs. First of all, the high surface area of the PANI-NWs can provide abundant active binding sites for the target molecule. Secondly, the concave-shaped PANI-NWs allow a higher portion of the volume of the NW to contribute to the signal change than conventional NWs, thus utilizing the high surface area to volume ratio.

5.3.2 BNP Detections in Real Samples

The use of the PANI-NWs FET sensors for detection of BNP in real samples was evaluated by measuring different BNP concentrations in human blood serum. Due to the property differences between the serum and PBS solution (e.g., salt concentrations, viscosity, and dielectric constant), the sensitivity and detection limit of the sensor can be affected. In these tests, to eliminate the influence of the salt concentration, instead of using PBS buffer solution as background, serum solution containing no BNP molecules was employed as the background baseline reference. The FET tests results were plotted in figure 5.4. It can be clearly observed that the drain current for the 1 pg/mL BNP serum solution was higher than the one for the serum solution. The current change at V_g=-0.4 V was about 18.8%. The same change was found for higher BNP concentration, which had a bigger change (~24.3%) on the drain current as well.

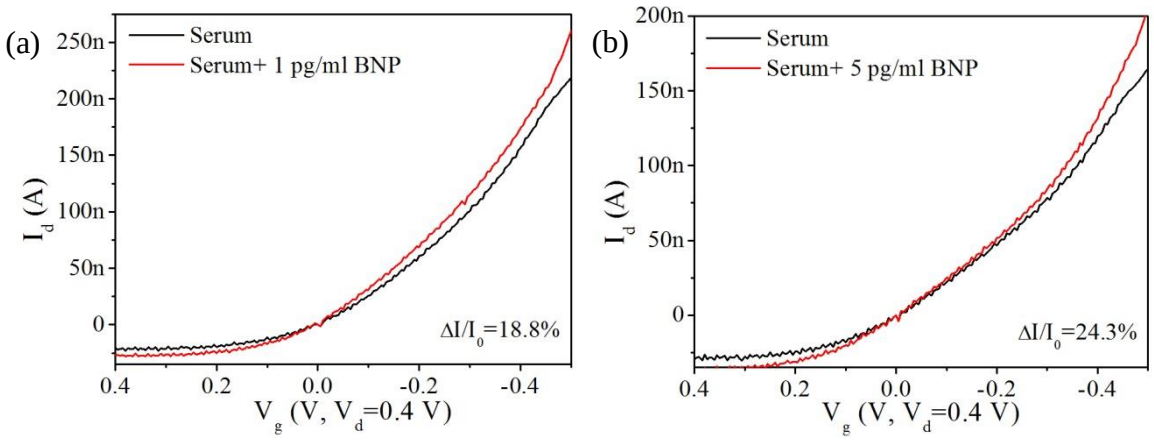

Figure 5.4. Typical I_d-V_g curves of PANI NW FET sensors in responding to BNP in serum solutions. Drain voltage was set as 0.4 V. The changes in the drain curent for (a) 1 pg/mL and (b) 5 pg/mL BNP are about ~18.8% and ~24.3%. All the measurements were performed in ambient conditions.

Serum samples with different BNP concentrations were tested to study the relationship between the BNP concentration and the sensor response. The PANI-NWs FET sensors showed ~4% increase in I_d at the BNP concentration of 100 fg/mL. Despite the reduced sensitivity compared to that obtained in the PBS solution, distinguishable changes in the FET sensors were observed over a wide range from 100 fg/mL to 5 pg/mL as shown in figure 5.5. This demonstrates the applicability of the PANI-NWs FET sensors for the monitoring of BNP in real serum samples on a regular basis, which requires the detection of blood BNP at levels below normal conditions (20 pg/mL).

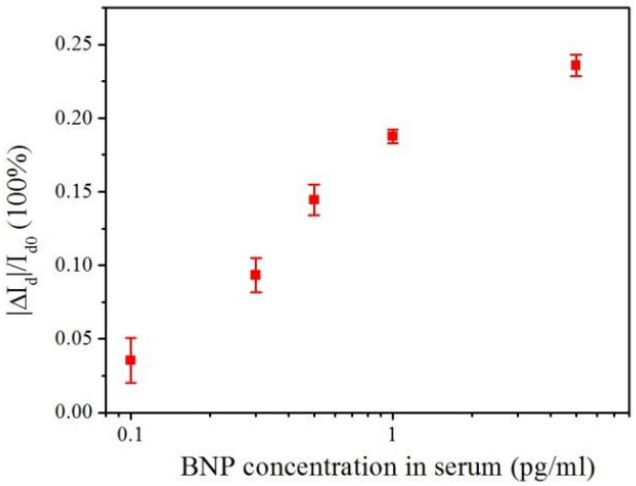

Figure 5.5. Normalized drain current change of the NW FET sensors as a function of BNP concentration with respect to the baseline in PBS solution.

For further study, the BNP purchased from Sigma-Aldrich was spiked in normal human blood. The normal human blood was provided by the UPMC Cardiovascular Institute. The same setup and method used in the BNP detection in PBS solution were also employed for these tests except the applied drain and gate voltages were altered. The I_d-V_g curves of the PANI-NW FET sensors responding to whole blood samples are shown in figure 5.6a and b. It is clearly shown in the figures that the I_d of the NWwas decreased (~-18.5%) after the addition of a whole blood.

This is due to the high viscosity and ionic concentrations in whole blood. When a BNP (100 pg/mL) whole blood sample was added onto the sensor, it showed an increased I_d (~22.3%). The negative effect on the NW caused by the whole blood was counteracted by the addition of BNP because the binding of negatively charged BNP resulted in positive current changes in the NW.

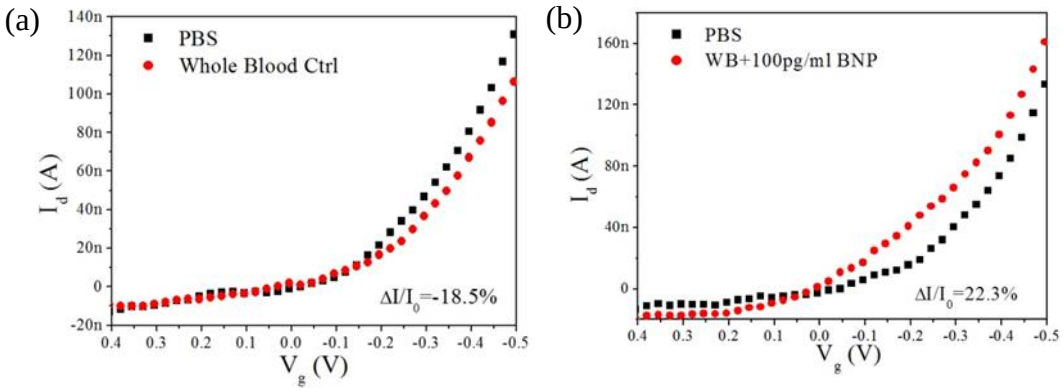

Figure 5.6. I_d-V_g curves of PANI NW FET sensors responding to health whole blood control sample (a) and whole blood sample (b) containing 100 pg/mL BNP.

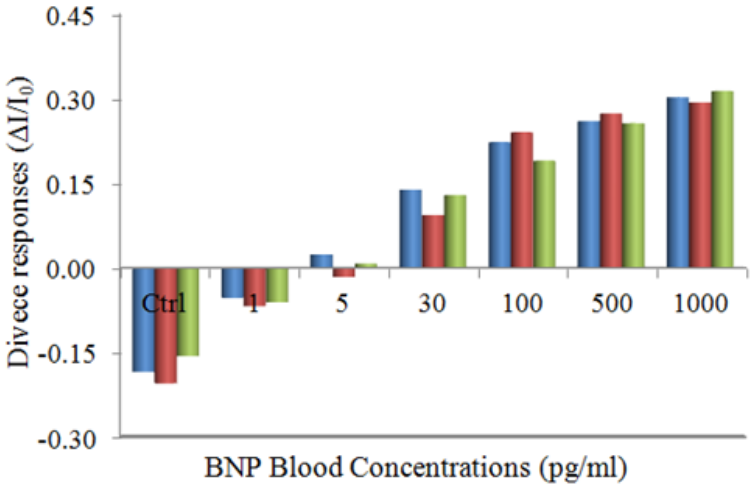

Figure 5.7. Normalized drain current change of the NW FET sensors as a function of BNP blood concentration referring to the baseline in PBS solution.

The change in the normalized drain current of the PANI-NW FET sensors as a function of BNP blood concentration is given in figure 5.7. As shown in the graph, a positive response of the NW was shown when the BNP concentration was higher than 5 pg/mL. More positive current changes can be observed as the BNP concentration is increased from 5 pg/mL to 1 ng/mL. These results indicate the feasibility of using the PANI NW FET biosensor to detect BNP biomarkers in whole blood.

5.3.3 FET Sensing Mechanism

The mechanism behind change in current upon binding of target molecules can be explained by the gating effect of surface charges carried by the target molecules. Because the isoelectric point (pI) of BNP used in this experiment is ~5.4, the BNP molecules are negatively charged in PBS solution that has a pH of 7.20. Therefore, the negative surface charges introduced by the specific binding between BNP and its receptor would lead to the carrier accumulation in PANI-NWs, causing an increase in drain current. According to this principle, the drain current of the PANI-NWs would decrease if positively charged target molecules are captured by the aptamers on the surface of PANI-NWs.

To verify this, a PBS solution with a pH of 4.75 containing 1 pg/mL BNP was added to the PANI-NWs FET sensor. As shown in figure 5.8, a decrease in I_d is observed upon the addition of this PBS solution, in which the BNP molecules are positively charged. Hence the current response is believed to be attributed to the surface charge gating effect introduced by the specific binding. Interestingly, compared with the current change (~28%) of 1 pg/mL BNP in pH 7.20 PBS solution, the PANI-NWs showed a ~10% change in I_d when the pH of PBS solution decreased to 4.75. The possible reason is that the number of charges carried by a BNP molecule

in pH 7.20 PBS solutions is more than that in pH 4.75 PBS solution due to the larger difference between the pH and the pI of BNP in former solution than that in the latter one.

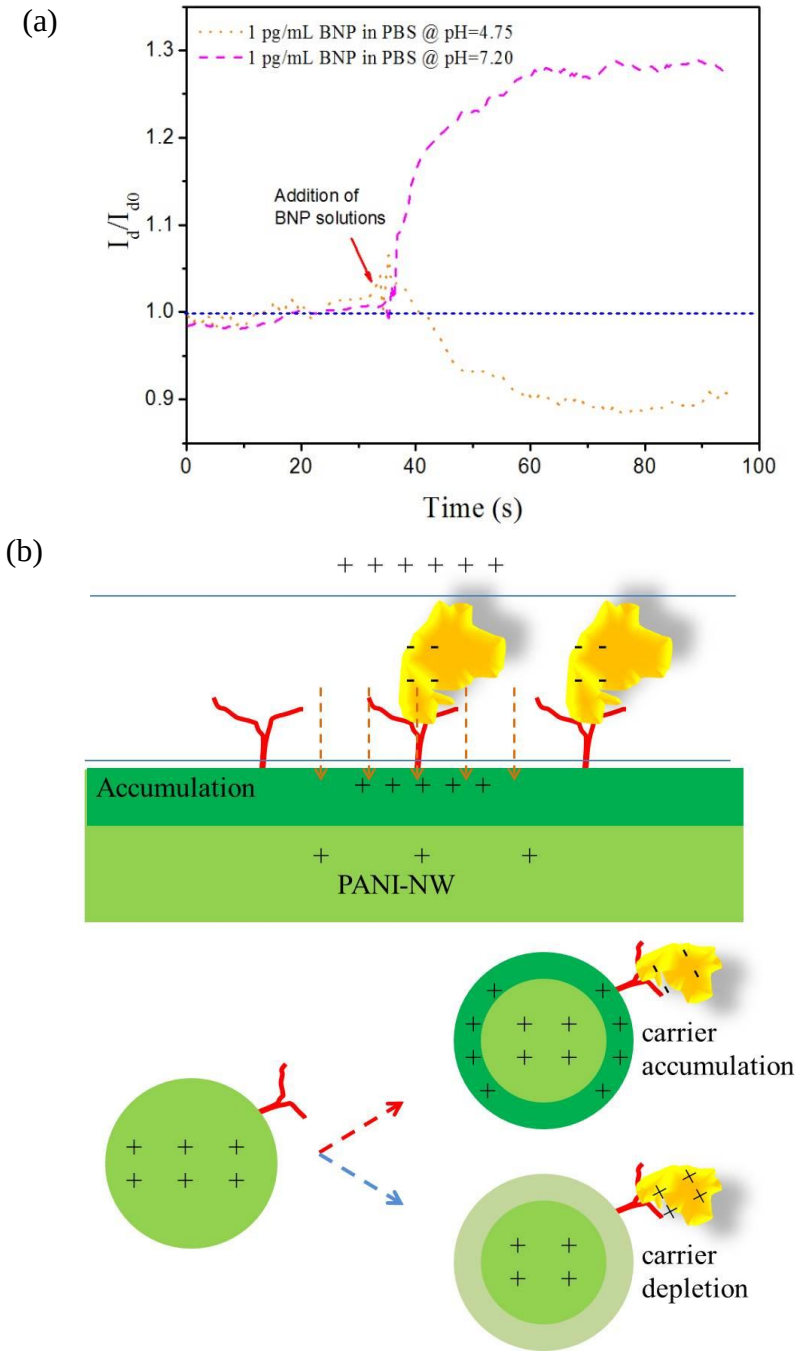

Figure 5.8. (a) The detection of BNP in PBS solutions with different pH and (b) the biosensing mechanism.

5.3.4 Debye-Length Investigation

Traditional conductometric nanowire biosensors that only use two electrodes to measure the nanowire conductance/resistance changes have a poor sensitivity and high detection limit when compared to the nanowire field effect transistor (NW-FET) biosensors because the additional gate modulation in NW-FETs can amplify detection signals. Specifically the charges introduced by the captured molecules on the surface of NW-FETs can induce a gating effect on the NW,[128, 155] resulting in the accumulation or depletion of carriers in the NW. While in ionic solution, the electrical double layer formed by the ions can reduce the effective charges of the bound molecules.[156] This effect has a significant impact on the sensing performance of the biosensor and it is known as Debye screening and is shown in figure 5.9, termed as the Debye length (λ_D).[156, 157] For aqueous solutions at room temperature, this length is given by

$$\lambda_D = \frac{1}{\sqrt{4\pi l_B \sum_i \rho_i Z_i}}$$

where l_B is the Bjerrum length, and ρ_i and Z_i are the density and the valence of the *i*-th ionic species. The solution Debye length strongly affects the gating effect for NW-FET biosensors. The study of Debye screening and Debye length engineering thus is critical to improve the NW-FET sensors' performance.

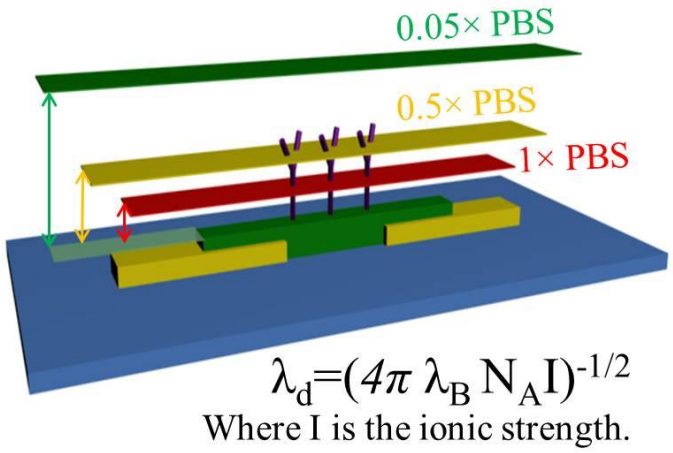

Figure 5.9. Illustration of the Debye screening length in solution. Within shorter Debye length, more of the charges carried by the target molecules will be screened by counter-ion.

At the same time, the Debye length of semiconductors (figure 5.10) also has a very significant influence on the FET sensor behavior too. The Debye length of semiconductors is also known as the Thomas-Fermi screening length. The electrical field generated by the surface charges can penetrate the semiconductor surface up to a distance that is equal to the Thomas-Femi screening length. Hence only a portion of the semiconductor is affected by the surface charges when the Thomas-Fermi screening length of the semiconductor is shorter than the radius of a cylinder semiconductor. This implies that the Thomas-Fermi screening length of a semiconductor can strongly impact the FET sensor performance. The Thomas-Fermi screening length of semiconductors is given by:

$$\lambda d = \sqrt{\frac{\varepsilon K_B T}{q^2 N_d}}$$

Where ε is the dielectric constant, K_B is the Boltzmann's constant, T is the absolute temperature in kelvin, q is the elementary charge, and N_d is the density of dopants (either donors or acceptors).

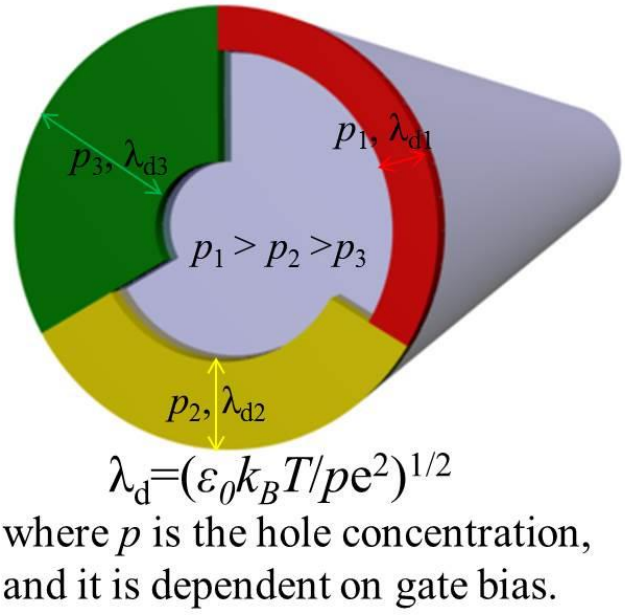

Figure 5.10. Illustration of the Thomas-Fermi screening length of a nanowire, which is dependent on the carrier concentration in the NW.

To study the impact of the solution Debye length to the sensor performance, five PBS dilutions were tested for the BNP detection. For a typical measurement, the I_d of the sensor versus the drain voltage (V_d) in PBS dilutions (pH=7.4) was established first. Then the same PBS solution containing 10 pg/mL BNP was added to the sensor. The binding of BNP, a negatively charged peptide with an isoelectric point (pI) of ~5.42,[158] to the sensor resulted in an increased I_d of the p-type device. Multiple tests were performed on the sensor using different PBS dilutions. As shown in figure 5.11a, larger I_d changes can be observed in 0.05x PBS than that in 0.5x PBS. For instance, the I_d changes of the NW-FET sensor in 0.05x and 0.5x PBS were 15.7 nA and 10.9 nA at V_d=0.7 V. The ionic strengths of 0.05x and 0.5x PBS solutions yielded Debye lengths of 3.3 nm and 1.04 nm, respectively. Because of the larger λ_D in 0.05x PBS, more charges carried by the BNP molecules were effective in altering the conductivity of the NW, resulting in a larger I_d changes. Figure 5.11b shows the I_d changes of the NW versus the solution Debye

length at V_d=0.7 V and V_g=-0.25 V. An exponential increase in I_d can be observed as the Debye screen length increases. The theoretical nonlinear fit of the device I_d corresponds to the Debye length which is also shown (dash line). The estimated maximum I_d change is ~20 nA, and the average distance of the bound charges to the NW surface is ~1.4 nm.

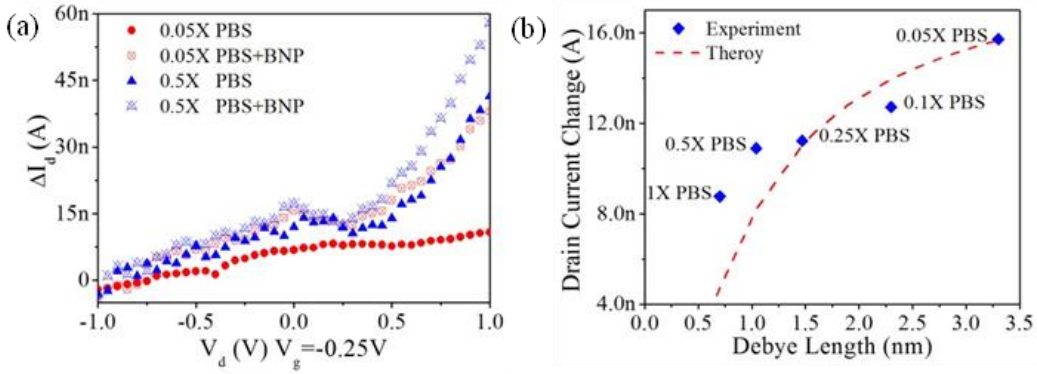

Figure 5.11. (a) I_d-V_d curves of a NW-FET sensor in different PBS dilutions. (b) Drain current change as a function of solution Debye length, and the theoretical fit of current change versus Debye length. Within shorter Debye length, more of the charges carried by the target molecules will be screened by counterions.

Our previous investigation indicates that the Debye screening had a strong impact on the sensing performance of our FET biosensors. Our experimental data matches the theoretical fit very well. Hence the Debye length should be engineered to obtain optimal performance for the NW-FET biosensor. Although the NW-FET biosensor can be utilized to detect BNP in normal blood or patients' serum as demonstrated previously, the tests were not performed with an optimized solution Debye length either in normal blood or patients' serum due to their high salts concentrations. Hence the engineering of Debye length in untreated blood or serum samples that contain high ions concentration still poses challenges.

In general, the performance of NW-FET sensors are impacted and determined by three major factors: (1) the ions concentrations in blood/serum, (2) the net charges carried by the target molecules, and (3) the carrier concentration in the NW. The ion concentration in blood/serum

determines the solution Debye length, beyond which the gating effect from the bound charges to the NW would be screened out. The net charge carried by the target molecules is dependent on its pI and the blood/serum pH, which determines the accumulation or depletion of carriers on the NW surface. The carrier concentration in the NW can be controlled by the gate bias, which has a great impact on the amount of current change.

Our previous studies on the solution Debye length reveal that the solution Debye length has a significant impact on the NW-FET sensor performance. By diluting the buffer solution, which reduces the solution ionic strength, larger solution Debye lengths can be obtained. Those large Debye lengths could increase the effectiveness of charges that are bound to the NW, generating more current changes. However, ion concentrations are high (> 100 mM) and the pH in blood/serum is fixed, giving a short solution Debye length (<0.7 nm) and defined net charges of the target molecules. As a result, the direct detection of biomolecules in untreated blood/serum is severely hampered by the Debye screening effects.

Recent studies have demonstrated that the sensing performance of NW-FET sensors can be exponentially enhanced in the sub-threshold regime because the reduced screening of carriers in the NW promises the most effective gating effect from the charges bound on the NW surface.[128] For NW-FET sensors, it is more meaningful to characterize the sensor by the dimensionless parameter, $\Delta I/I_0$, which relates the volume of the NW gated by surface charges (represented by ΔI) to volume of the whole NW (represented by I_0). Therefore, $\Delta I/I_0$ should reach maximum when the NW is fully utilized, which happens when the sensor is near carrier depletion.[128] This finding thus inspires us to engineer the Debye length of the NW to improve its sensing performance.

As introduced before, the Debye length of the NW (Thomas-Fermi screening length) is determined by the carrier concentration in the NW. For high carrier concentration in NW, the screening length is shorter. Thus, the charged molecules bound on surface can only gate the NW within a thin surface layer, producing small current changes in the NW. To achieve large current changes, a long Debye length (low carrier concentration) is required, which can be obtained at the sub-threshold region of the NW. The sub-threshold region is where the minority carriers present under the gate when the gate voltage is less than the threshold voltage. These carriers cannot be totally neglected, and play an important role in device and circuit performance. The current originated from these carriers can be addressed using a capacitor model. An illustration of the model is shown in figure 5.12.

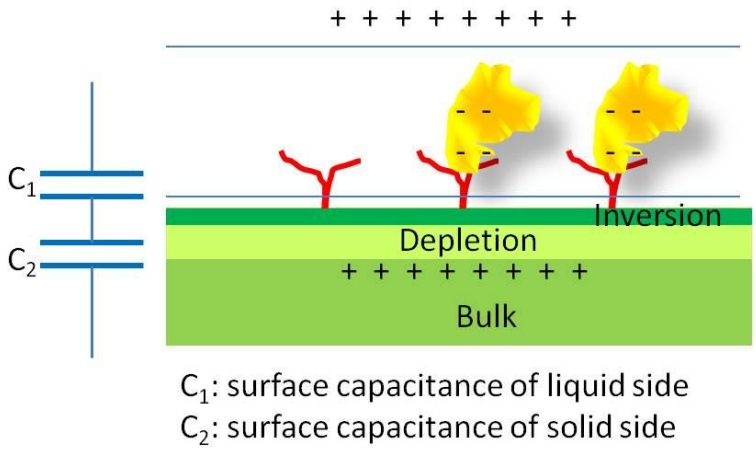

Figure 5.12. An illustration of the capacitor model for the sub-threshold region current.

According to the model,

$C_2 = \frac{\partial Q_b}{\partial \Phi_s} = \frac{\gamma C_1}{\phi_s^{1/2}}$, where γ is the body effect parameter

$\Phi_s - 2\Phi_b = (V_g - V_b)/\eta$, where η is the capacitive coupling

$$\eta = 1 - \frac{C_2}{C_1} = 1 + \frac{2\gamma}{2(2\Phi_b)^{1/2}}$$

$$I_d = I_{pf} e^{\frac{q(V_g - V_t)}{\eta KT}} (1 - e^{\frac{qV_b}{KT}})$$

$$\text{where, } I_{pf} = \beta(1-\eta)(KT/q)^2$$

Hence the signal change is:

$$\frac{I_{d1} - I_{d0}}{I_{d0}} = \frac{I_{d1}}{I_{d0}} - 1 = \frac{e^{\frac{q(\Phi_{s1} - 2\Phi_b)}{KT}}}{e^{\frac{q(\Phi_{s0} - 2\Phi_b)}{KT}}} - 1 = e^{\frac{q\Delta\phi}{KT}} - 1 \cdots\cdots\cdots\cdots\cdots\cdots (1)$$

While in the linear region, the drain current can be expressed as:

$$I_d = \beta \left[(V_g - V_t) - \frac{V_d}{2} \right] \cdot V_d$$

$$V_t = V_{fb} + 2\phi_b - \frac{Q_b}{C_{ox}}$$

$$V_{fb} = V_{ref} - \chi^{sol} - \frac{\Phi_s}{q} - \phi_s = Const. - \phi_s$$

Where V_{ref} represent the contribution of reference electrode

χ^{sol} is the surface dipole potential of the solvent

Φ_s is the semiconductor work function.

Therefore,

$$V_t = Const. - \phi_s + 2\phi_b - \frac{Q_b}{C_{ox}}$$

Upon binding of biomarkers, the surface potential ϕ_s changes

$$V_{t1} = Const. - \phi_{s1} + 2\phi_b - \frac{Q_b}{C_{ox}}$$

$$\frac{I_{d1} - I_{d0}}{I_{d0}} = \frac{\beta(\phi_{s1} - \phi_s) \cdot V_d}{\beta \left[(V_g - V_t) - \frac{V_d}{2} \right] \cdot V_d} = \frac{\Delta\phi_s}{(V_g - V_t) - \frac{V_d}{2}} \cdots\cdots\cdots\cdots\cdots\cdots (2)$$

From equation (1) and (2), the current change in the sub-threshold region increases exponentially, relative to the surface potential changes, while in linear region. Therefore, the largest change can be achieved in the sub-threshold region.

The sub-threshold regime of the NW can be observed from its I_d-V_g characterization. Then the optimum gate bias can be found from the BNP measurements in blood/serum. The optimal Debye length in the NW can then be engineered with this optimum gate bias, and the highest volume ratio between the part of the NW gated by surface charges and the whole body of the NW could be obtained. This setup with the engineered NW Debye length is expected to achieve the highest current change and lowest detection limit of the sensor in blood/serum.

Determining the sub-threshold region from a typical I_d-V_g curve is simple and straightforward. As shown in figure 5.13, the sub-threshold is in the region where the gate voltage is less than the threshold voltage. In this region an exponential increasing current can be observed. *The* I_d-V_g curves of a PANI-NW are shown in figure 5.13b for normal (blue) and logarithmic (red) scales. The drain current was off until the gate voltage was less than -0.6 V, after which the current increased exponentially. When the gate voltage was less than -0.7 V, the drain current followed a linear change. Where the drain current showed an exponential change in the region is described as the sub-threshold region. In this *I-V* curve, the sub-threshold region for the PANI-NW was found in between 0.6-0.7 V.

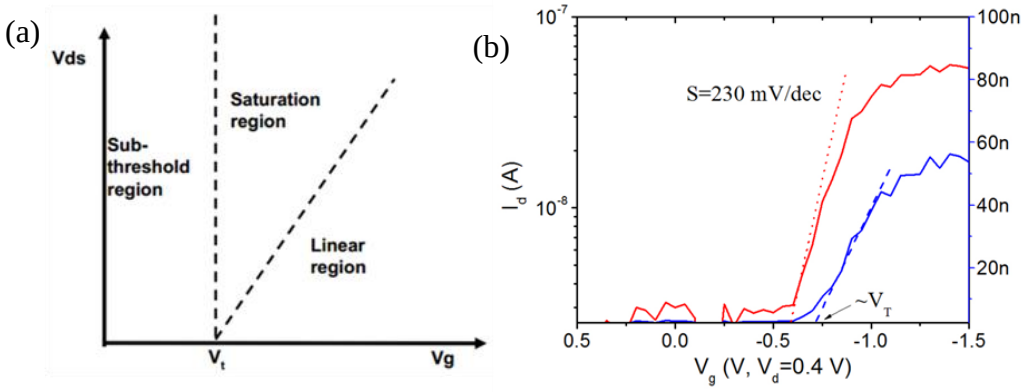

Figure 5.13. The sub-threshold region of FET devices. (a) Definition of sub-threshold region. (b) Plot of the I-V curve of PANI-NW, in which the sub-threshold region was found within 0.6-0.7 V.

The tests of BNP modified PANI-NWs with an optimized gate bias were performed to achieve the optimal sensing response. Similar tests method for BNP detection was used and the gate bias was swept from 0.5 to -1.5 V. Serum with no BNP was used as the blank background and reference. The responses of the PANI-NWs in drain currents to BNP solutions were gradually increased as the BNP concentration increased from 0.5 to 5 pg/mL. The drain current changes of the sensor were calculated at the PANI-NW sub-threshold region (V_g=-0.6 V) and the saturation region (V_g=-1.5 V), and the comparison of the responses from the NW is given in the table. The current change of the sensor to 0.5 pg/mL BNP was ~73.3% at its sub-threshold region, which is about 5 times greater than that at its saturation region (~15.9%). The same phenomena were observed for higher BNP concentration and the results are shown in figure 5.14. These results clearly showed that the sub-threshold region of the sensor was more sensitive than the liner or saturation region of the sensor, which matches the sub-threshold theory.

(a)

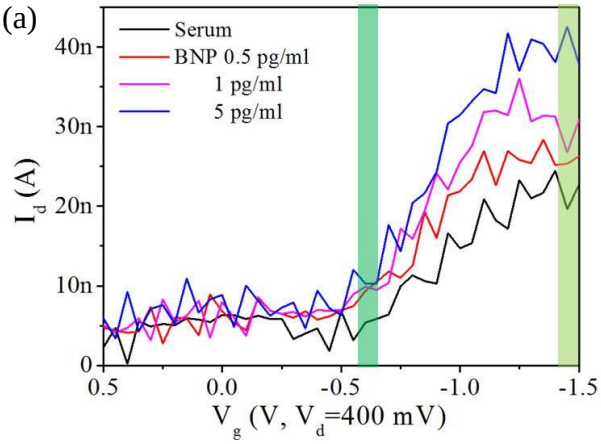

(b)

ΔI/I	Vg=-0.6 V	Vg=-1.5 V
0.5 pg/ml	73.3%	15.9%
1 pg/ml	84.5%	36.1%
5 pg/ml	92.2%	66.5%

Figure 5.14. (a) I_d-V_g curves of BNP modified PANI-NW responding to BNP targets. In the sub-threshold region, the NW showed greater changes than that in linear and saturation region. (b) Comparison of the changes in sub-threshold region and saturation region.

5.3.5 Biosensor System

In order to build a biosensor platform with convenient interconnects for data acquisition, the sensor chip connectors were redesigned. Two different sockets were anchored on a PCB board so that the connectors are compatible to two different sensor chip layouts. One kind of layout requires wire-bonding to connect the sensor device to the measuring instrument. The other device layout does not require any wire-bonding steps, and the device can be directly inserted into the socket to connect to the measuring instrument (figure 5.15). The pads on a sensor chip were connected to an outlet socket, thus only few copper wires were needed to switch the sensors during measurements.

The microfluidic component contained a syringe pump, a multi-inlet microfluidic chip, and the microfluidic channel for sensors. The fluidic flow rate was controlled by the syringe pump with both withdraw and inject modes. The multiple-inlet microfluidic chip was employed

because multiple solutions were expected to flow into the microfluidic channel. The chip has five inlets for five different solutions at each test. The PDMS microfluidic replica was attached to the sensor chip so that the microfluidic channels covered the PANI-NW sensors. The outlet of the channel was connected to the syringe pump so that the solution could be withdrawn from the solution container, passing through the multiple-inlet chip and flow through the sensing area during the measurements.

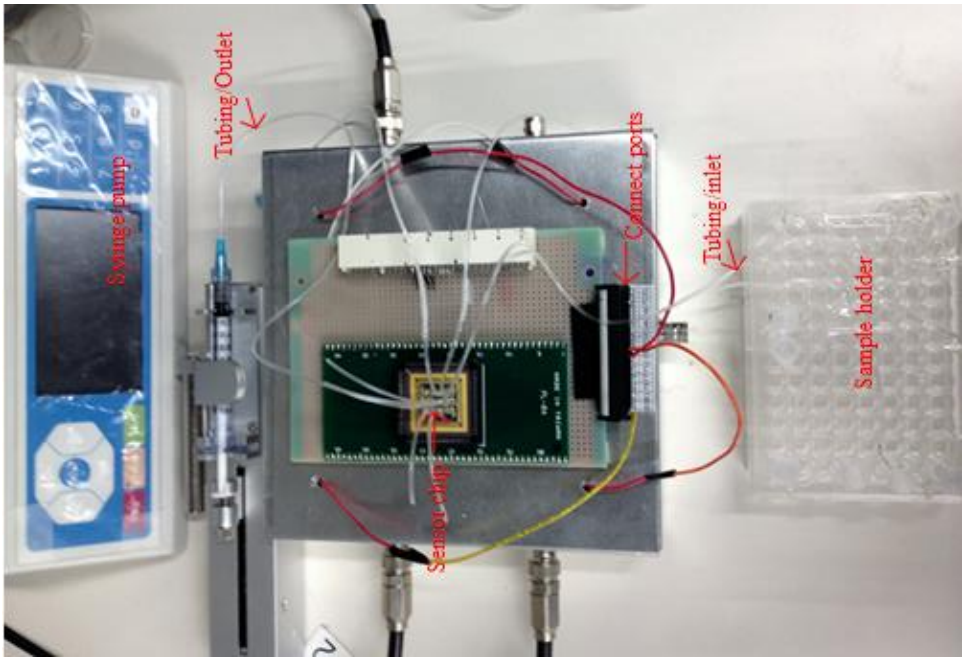

Figure 5.15. The redesigned sensor measurement system including multiple sample inlets, syringe pump, and chip sockets board that compatible to two different chip layouts. The whole system simplified the component assembly steps.

The BNP detection tests were also performed using the redesigned sensor system. The biosensor chip integrated with the microfluidic channel was placed in a socket and connected to the PCB board. For the measurements, the gate bias was swept from 1 V to -1.2 V at a constant drain voltage of 0.4 V. The solutions were sequentially flowed into the microfluidic channel and the data were shown in figure 5.16. No notable responses were observed in the PANI-NW for the

nonspecific targets when compared to the base response obtained with PBS. However, significant changes in drain current were seen for BNP solutions. This preliminary result demonstrated that the biosensor system has the capability to perform ultrasensitive biomolecule detections.

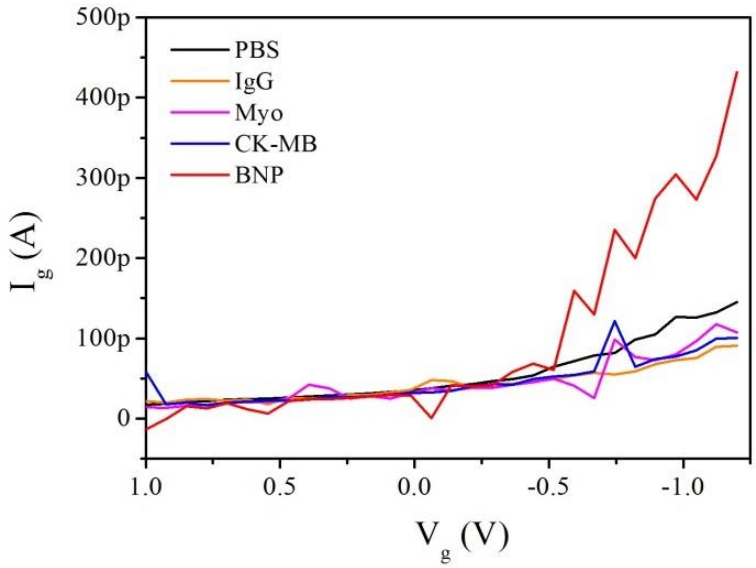

Figure 5.16. Several tests for a PANI-NW using the rebuilt measurement system.

To establish a portable biosensor platform, the previous design was adapted to be compatible with a potentiostat. There are many portable potentiostat instruments available in the market, thus the demonstration of this potentiostat based biosensor platform would suggest the potential for the future development of a portable biosensor system. The circuit and microfluidic design were kept the same, but an additional power supply was added to provide the gate bias. In order to control the power supply by a desktop, a bias control software user interface was built using Labview. The whole system is shown in figure 5.17. A very important improvement for this system is that the sensor chip was redesigned so that the chip could be inserted into the socket directly and no wire-bonding steps are required. This feature ensures good contact between the socket and the chip and reduces the process steps for wire-bonding.

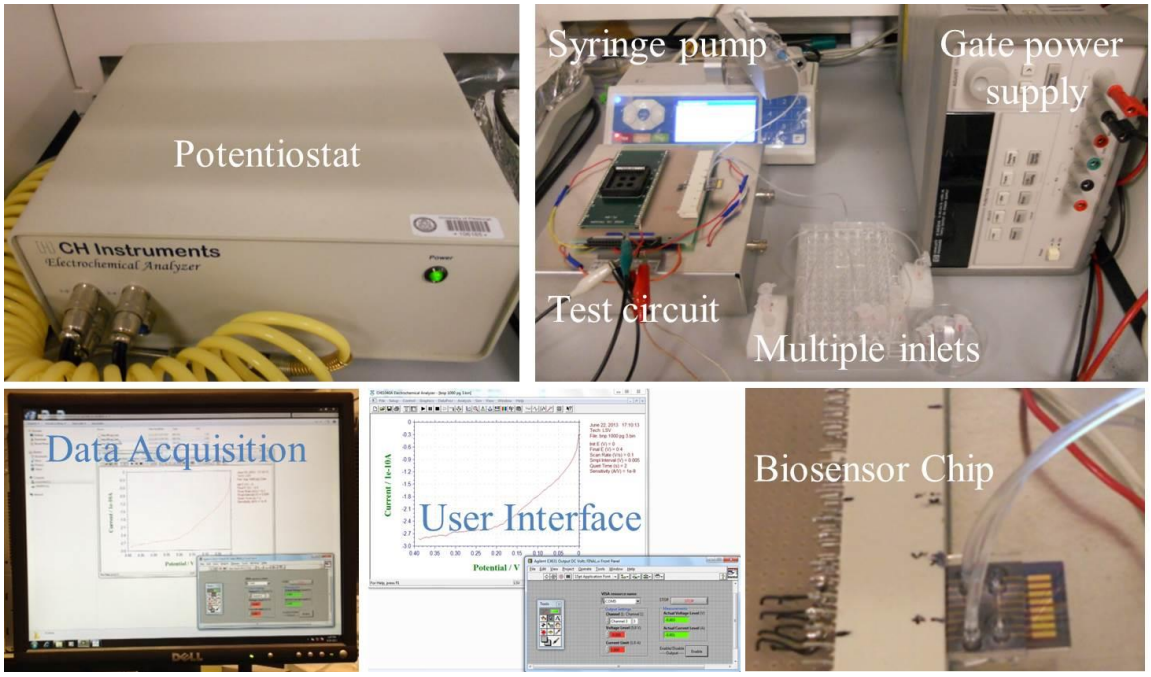

Figure 5.17. The latest sensor measurement system adapted from the previous system including multiple sample inlets, a syringe pump, and a chip sockets, a gate bias power supply, a potentiostat, and a data acquisition system. The whole system illustrated the potential for a portable biosensor system.

5.3.6 Biosensor System Evaluations

To find out the optimal parameters for the test, the effect of the drain voltage sweeping rate, and the applied gate bias were investigated. In electrochemistry, the peak current is proportional to the square root of the sweep rate, thus it is expected that different drain voltage sweeping rates would lead to different drain currents. The drain voltage sweeping tests were carried out using the biosensor system built previously at four different sweeping rates (0.01, 0.05, 0.1, 0.5 V/s). The results are shown in figure 5.18.

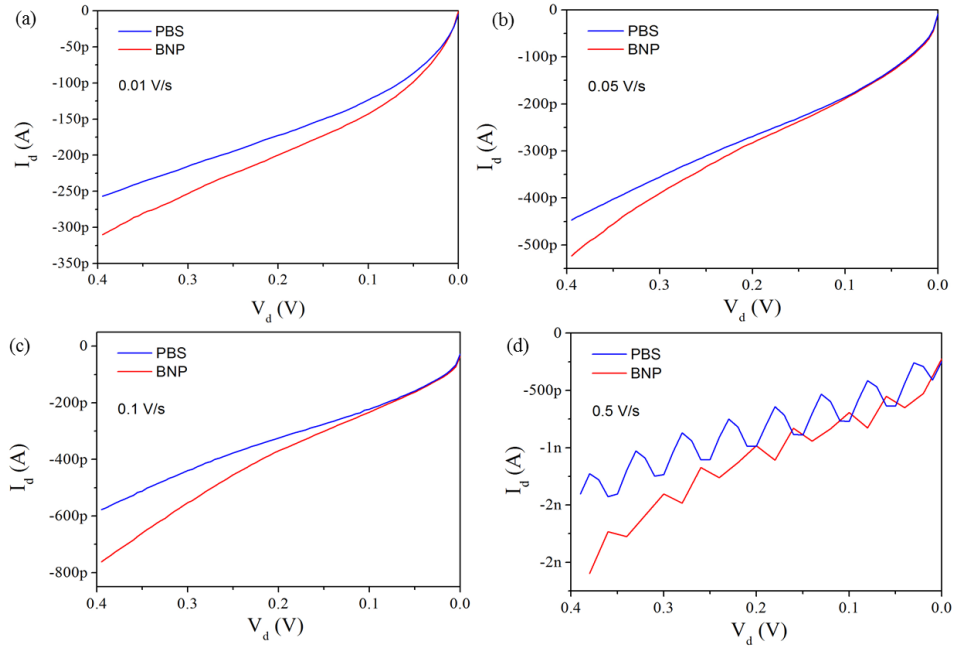

Figure 5.18. The drain voltage sweeping rate for the measurements: (a) 0.01 V/s, (b) 0.05 V/s, (c) 0.1 V/s, (a) 0.5 V/s.

As mentioned before, the peak current is proportional to the square root of the sweeping rate. The drain current for the sweeping rate at 0.05 and 0.10 V/s were about 440 pA and 600 pA when the drain potential was 0.4 V in PBS. The ratio between these two current was about 1.4, which is the square root of the sweeping ratio. In addition, small drain current was observed for slow sweeping rate and larger currents were found for fast sweeping. While for the 0.5 V/s sweeping rate, it had limited sampling points, thus the *I-V* curve was not smooth. For the other three sweeping rate, the *I-V* curves were very smooth. For a very fast detection, the sweeping rate of 0.1 V/s only required 4s for a measurement, therefore the drain potential sweeping rate were set as 0.1 V/s for the rest tests.

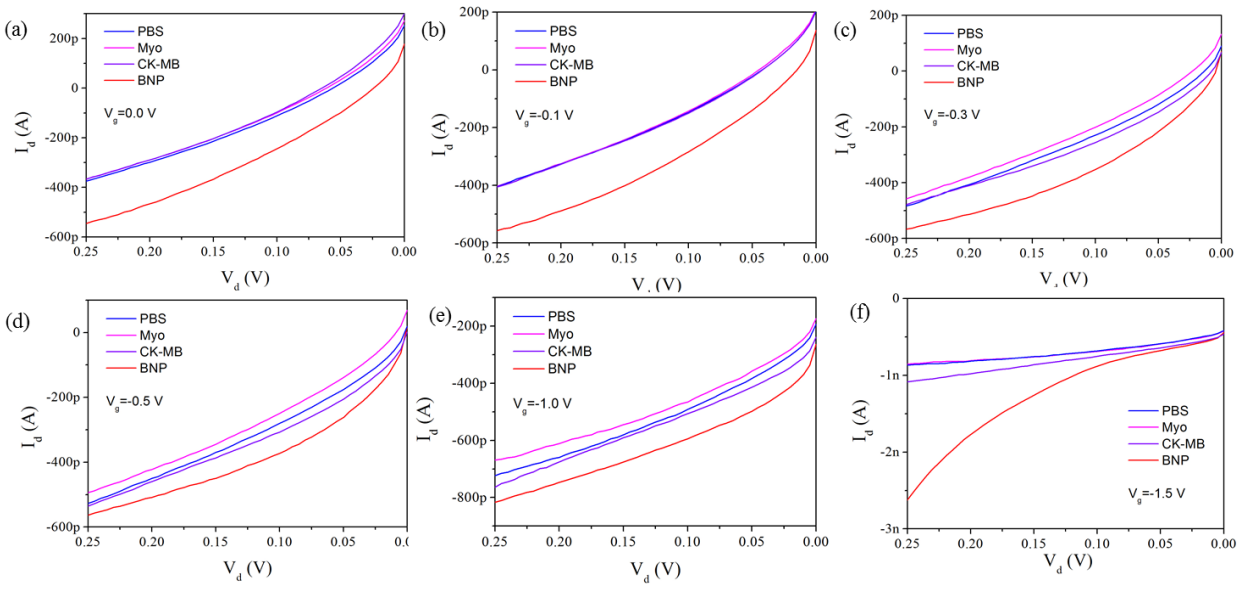

Figure 5.19. Different gate bias (a) 0, (b) -0.1, (c) -0.3, (d) -0.5, (e) -1.0, and (f) -1.5 were applied to find out the optiaml gate bias conditions for the sensing test.

The gate bias also has very crucial impact on the measured responses. To find out the optimal gate bias for the potentiostat biosensor system, several gate biases were used for the measurements. The sweeping of the gate bias for the tests was not applicable due to that the power supply can only generate fixed output. In this study, six gate biases 0, -0.1, -0.3, -0.5, -1.0, -1.5 V were tested, and the results are shown in figure 5.19. Since the PANI nanobelts are typical p-type material in PBS solution, as the gate bias went to more negative, higher drain currents were obtained. For example, the source-drain current at 0 V gate bias was ~-700 pA for the target, and the current for -1.5 V gate bias was ~-6 nA. But in the meanwhile, the current for the background and the non-specific cardiac biomarkers (Myo, CK-MB) were also amplified, leading to relatively less sensitive and specific responses for the PANI nanobelts to the target BNP molecules. According to these results, the gate bias of 0 V was selected for the rest tests.

In previous study, the optimal measuring conditions were found for the tests. Then the tests of BNP biomarker concentrations versus the drain current changes with the optimized

conditions were performed for the further evaluation of this potentiostat based biosensor system. The specificity of the biosensor was examined using the system, and the results are shown in figure 5.20. For non-specific cardiac biomarkers, e.g. Myo, cTni, and CK-MB, the BNP sensor showed nearly non-response referring to the background in PBS solution despite that the concentration of these non-specific biomarkers were very high. However, when the BNP biomarker was added to the sensor, an obvious drain current increase was observed. This result revealed that the biosensor was able to specifically recognize the target. More importantly, as the BNP concentration increased from 50 pg/mL to 1000 pg/mL, the drain current increased accordingly as shown in figure 5.20b. Since the test results would be influenced by many factors both by the sensor itself and the test environments, hence to gain results with high confidence, 20 devices were tested. These devices were tested with all the five BNP concentrations and the results are given in table 2. The response changes were calculated referring to the device responses in PBS background. These results showed large range variations, therefore, a statistic data processing method was used to reduce the variations and errors.

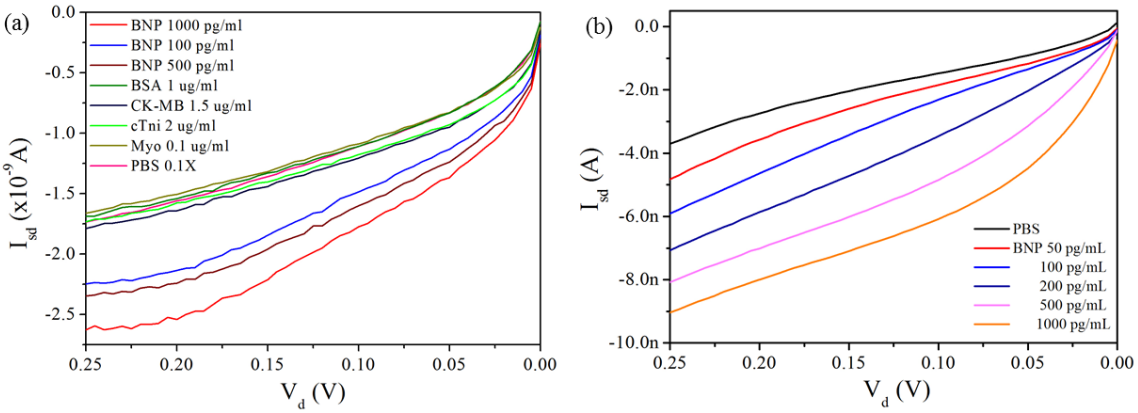

Figure 5.20. (a) Specificity tests of the sensor device using the potentiostat biosensor system. (b) A example of the sensor responses to different BNP concentrations.

Table 5.1. Test data of 20 sensor devices response to different BNP concentrations.

Device #	BNP Concentration (pg/mL)				
	50	100	200	500	1000
1	11%	21%	62%	97%	140%
2	13%	18%	37%	80%	102%
3	16%	49%	70%	84%	90%
4	17%	34%	83%	120%	138%
5	17%	40%	76%	95%	110%
6	19%	50%	82%	101%	112%
7	21%	32%	38%	60%	77%
8	24%	33%	38%	61%	78%
9	25%	54%	81%	84%	118%
10	25%	28%	70%	116%	139%
11	25%	34%	46%	63%	81%
12	25%	29%	34%	61%	71%
13	25%	43%	74%	86%	93%
14	27%	41%	56%	70%	74%
15	28%	45%	63%	74%	81%
16	29%	48%	61%	78%	82%
17	31%	60%	91%	118%	131%
18	33%	36%	57%	67%	79%
19	34%	52%	83%	105%	133%
20	39%	75%	94%	122%	130%
Summary					
Mean	24%	41%	65%	87%	103%
Sigma	7%	14%	19%	21%	25%

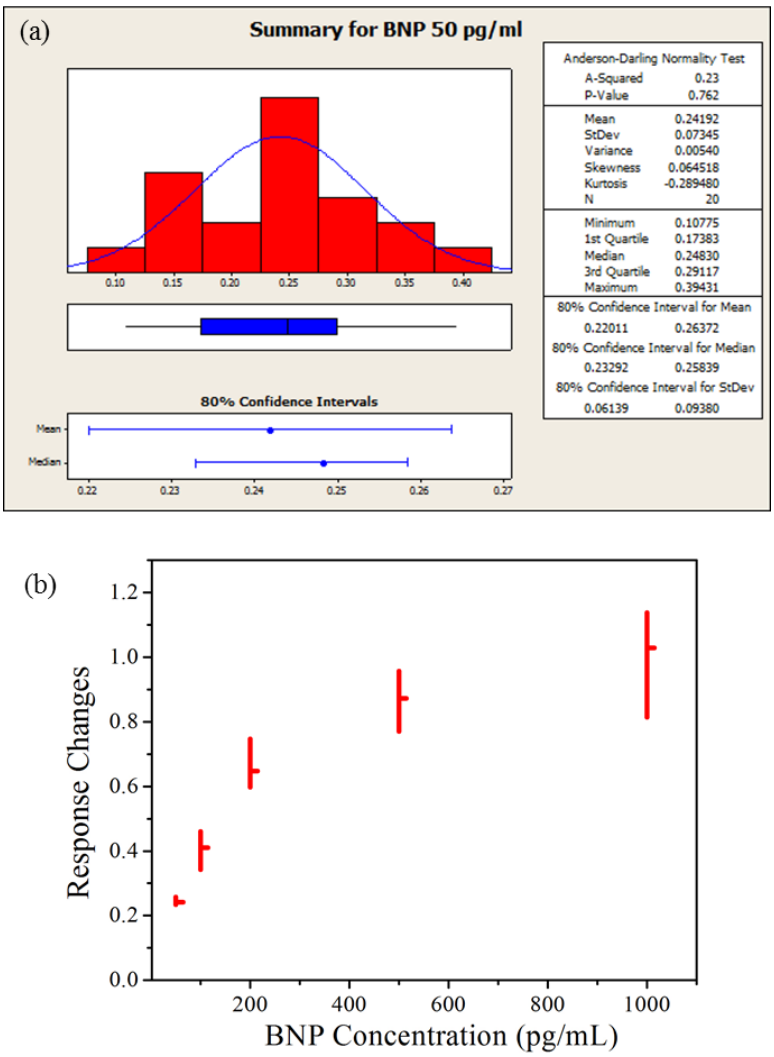

Figure 5.21. (a) An example of statistic data analysis of the data obtained from 20 sensor devices for 50 pg/mL BNP. The figure showed the results distribution, the mean, the standard deviation, and 80% confidence interval. (b) Statistic results of the 20 sensor devices test results.

Table 5.2. The statistic data calculated from 20 devices for different BNP concentrations.

BNP Conc. (pg/mL)	Mean	Sigma	80% Confidence Interval	
			Lower	Upper
50	24.2%	7.3%	23.3%	25.8%
100	41.1%	13.6%	34.2%	46.1%
200	64.8%	19.0%	59.7%	74.8%
500	87.2%	21.1%	76.9%	95.8%
1000	102.9%	25.2%	81.4%	113.8%

The test data of 20 samples were statistically processed to eliminate errors from the tests. For example, in figure 5.21 the normal distribution plot of the data for 50 pg/mL BNP showed the distribution of the data from the minimum to the maximum test results. It also calculated the mean and standard derivation for the tests, and the 80% confidence intervals for both mean and median. All the data for different BNP concentrations were statistically analyzed and the results were plot in figure 5.21b. The horizontal bars are the mean of each point and the vertical bars show the response ranges for each point with 80% confidence. It can be clearly observed from the figure, the sensors had a linear detection range from 50 to 200 pg/mL. And the sensors became saturated for higher concentrations, e.g. 1000 pg/mL. The detailed drain current changes and the corresponding 80% confidence intervals for these concentrations are listed in table 5.2. This test results are comparable with the results obtained from the PANI-NWs.

The shelf-life of the functionalized biosensor is an important parameter for the device. In fact, the device shelf-life is mainly determined by the biomolecules modified on the surface of the PANI nanobelts. Typically, the antibodies are very sensitive to the environmental change, and the degradation or deactivation of the antibodies can be caused by temperature, the atmosphere, and the salt concentration. Hence to maintain the bioactivity of the antibodies, the functionalized devices were kept in 4 ℃ for the tests. For the same device, the response at day 1 was ~33% to 100 ng/mL BNP in PBS solution, and the response decreased to ~20% and ~14% at day 7 and 14 (figure 5.22). This response reduce was believed due to the deactivation of the antibodies modified on the PANI surface as the increasing storage time.

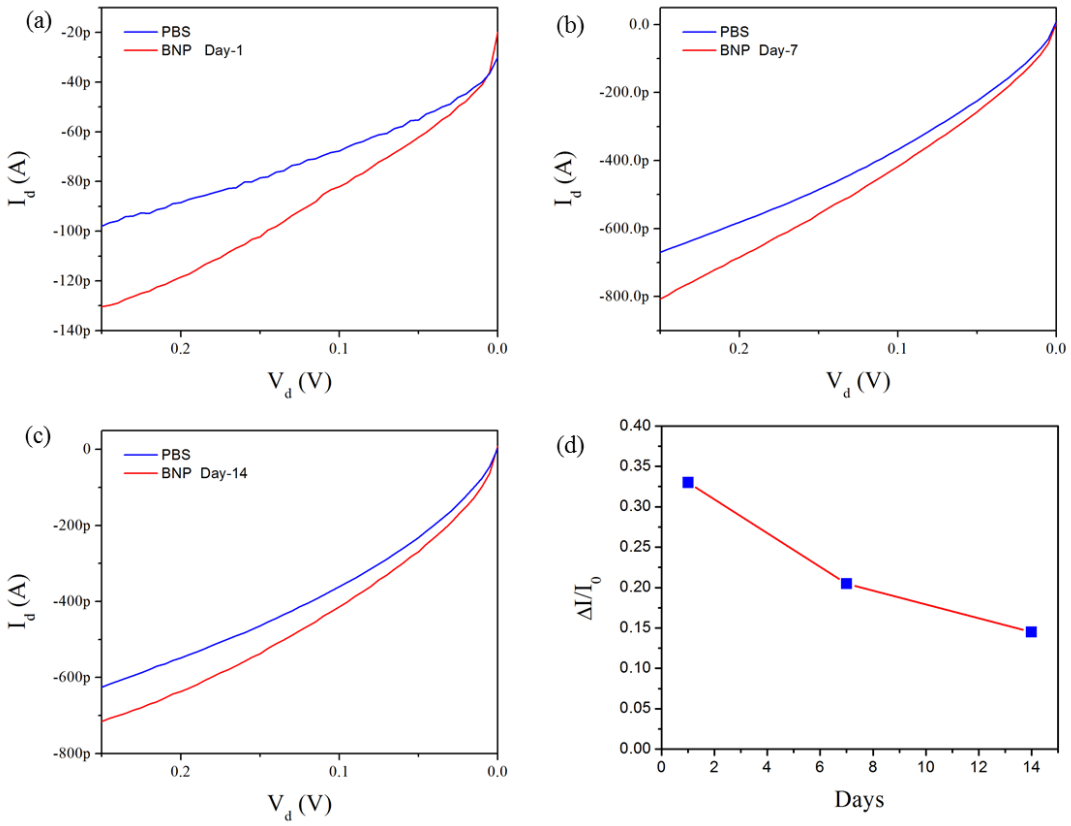

Figure 5.22. The reliability tests for the BNP sensors for two weeks. The sensor responses decreased about 50% in 14 days.

The test of BNP in buffer solution confirmed that the biosensor system has very sensitive responses to the target. While it is highly desired to monitor the BNP in the human bloods or serums, hence the blind tests of blood samples with unknown BNP concentrations were carried out using the biosensor system with 2D PANI nanobelts. The measurement parameters were set the same as that used in previous tests. The serum samples were collected from different patient with different health conditions. For example, as shown in figure 5.23, different serum samples from human and pig were tested with different devices. From the tests results in figure 5.23a, the normal sample always showed the lowest responses, the SE sample showed the biggest responses.

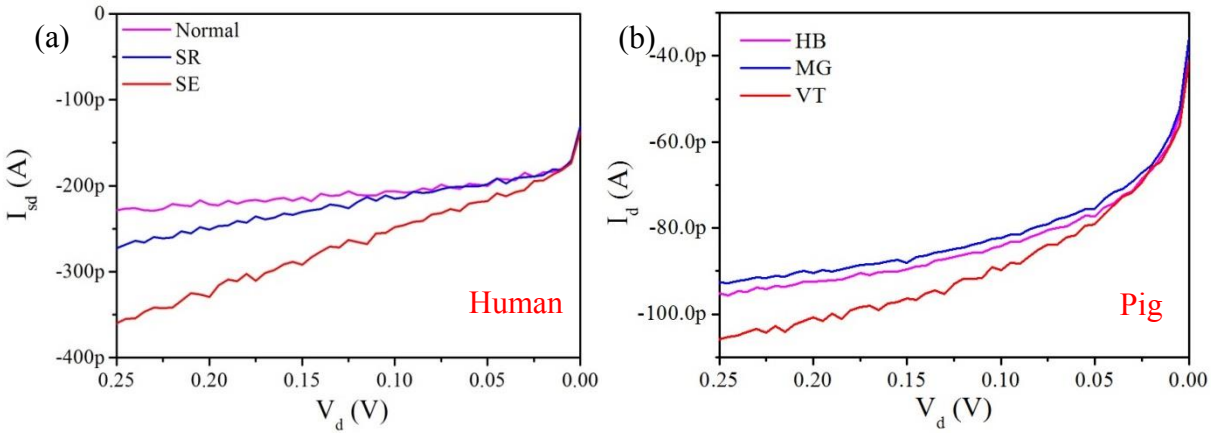

Figure 5.23. The blind tests for blood samples (a) human and (b) pig using the 2D PANI nanobelts FET sensors. The biosensor system is capable of detecting biomarkers in serum samples.

According to these results, the normal sample has the lowest BNP concentration. Comparing to the normal sample, the SE samples showed about 58.7% higher responses in average from three different devices. This is confirmed by ELISA test results of that the BNP concentration was ~126 pg/mL for SE sample. The normal sample has normal BNP level. For the pig serum, the tests results were opposite to that from the ELISA tests. However it showed different responses to different pig BNP levels. Studies on the pig BNP molecule structure and the using it specific BNP antibody would possibly address this issue. In short, these preliminary test results indicate that this sensor system has the ability to test real samples, and reliable results can be obtained with statistics analysis from more tests.

5.4 CONCLUSIONS

The PANI-NWs FET biosensors were found very sensitive to the BNP target in buffer solution. When the BNP concentration was progressively increased to 100 fg/mL, 500 fg/mL, 1 pg/mL,

and 5 pg/mL, the sensors showed consistent increases in I_d of ~17%, ~22%, ~28%, and ~32% respectively. These sensors also exhibited a wide dynamic sensing range from 25 fg/mL to 5pg/mL. The lowest detectable BNP concentration of 25 fg/mL is much lower than that obtained by surface plasma resonance sensor (5 pg/mL). The performance of this FET biosensor for serum samples were studies as well. The PANI-NWs FET sensors showed ~4% increase in I_d at the BNP concentration of 100 fg/mL in serum. Despite the reduced sensitivity compared to that obtained in PBS solution due to the high salt concentration in serum, distinguishable changes in the FET sensors were observed over a wide range from 100 fg/mL to 5 pg/mL. The test results found in whole blood still showed that this FET biosensor is capable of detecting BNP in whole blood although the signals were not as good as that in buffer or serum solution. The study of the detection mechanism reveals that the signal changes of this FET biosenor is due to the gating effect introduced by the net charges on target molecules.

The improvement on the PANI-NWs patterning using bi-layer photoresist process achieved better PANI-NW shape uniformity and better insulation among electrodes, thus allowed better sensor performance. Significantly, the investigation on the Debye length opened an approach to further improve the sensitivity of the biosensor. An optimal Debye length of the wire can be obtained by tuning the gate bias. Within the sub-threshold region of the NW, the sensor showed about 4 times increase in the response comparing to that in the linear region of the wire.

In order to further reduce the cost for the sensor fabrication, instead of using E-beam lithography, photolithography was used to pattern PANI nanobelts on the sensor chip. A biosensor system was as built for sensor tests, which contains a sensor component, a microfluidic part, a potentiostat, and a data acquisition sub-unit. The study regarding to the potential sweeping rate and gate bias reveals that the optimal sweeping rate was 0.1 V/s and the gate bias was 0 V

for the system. The statistical analysis of the test results from 20 sensor device using the biosensor system demonstrated that the sensors have a linear dynamic response range for BNP from 50 to 200 pg/mL. Those findings verified that the 2D PANI nanobelts possess comparable sensing performance with PANI-NWs. The demonstration of BNP test in serum samples using this system showed that the sensor devices can clearly determine different BNP concentration levels. These results suggested a great potential of this BNP sensing system for clinical use in future.

6.0 SUMMARY AND FUTURE WORK

The work present here includes significant advances in the understanding and developing of ultra-sensitive field-effect transistor biosensors for the monitoring and diagnosis of biomarkers. The understanding of the FET biosensor behaviors in fundamental helped to achieve optimal sensor performances in terms of sensitivity and detection limit. The sensor uniformity and reliability were greatly improved by introducing a well-controlled sensor fabrication method. These improvements facilitate the realization of an improved biosensor system incorporated with the sensor component, microfluidic unit, and data acquisition sub-system.

The incorporation of functionalized nanowires with a microfluidic unit was challenging since the typically microfluidic integration requires O_2 plasma treatment that potentially would deactivate the surface modified nanowires. To address this, a shadow mask was introduced to protect the nanowire sensors when perform the plasma treatments. The work concentrated on this aspect confirmed that the shadow mask was capable of preventing damages to the nanowires, hence ensured the bioactivity of the sensors after incorporated with microfluidics.

This research work provides an alternative polymer sensors fabrication method that combined with micro-fabrication techniques and chemical synthesis approach to prepare sensors with high uniformity and high yield on wafer scale. This promised the improvement on the reliability of the sensor tests. A three electrodes field effect transistor biosensor configuration with a liquid gate was studied for the monitoring of biomarkers in both buffer and serum

samples. The findings in this study verified that the nanowire sensors were capable of detecting the target even its concentration was very low. The investigation on the fundamental of the Debye length of semiconductor and sub-threshold region revealed that a great improvement of the sensor performance can be achieved with optimal test conditions. This study allowed the development of ultra-sensitive biosensors. In addition, to reduce the cost for sensor fabrication, a photolithography technique was introduced to replace the E-beam lithography process. This change allowed a great deal of reduction in time and cost. The 2D PANI nanobelts were found having comparable sensing performance with the 1D PANI NWs.

A sophisticated biosensor system was built in this research for the monitoring of a cardiovascular biomarker, BNP, based on the biosensors and microfluidics. The system was utilized to measure BNP in both buffer solution and serum samples. The results suggested that the system can be potentially applied for clinic use and adapted into a portable biosensor system in future.

Since the biosensor system was designed for real use to measure low concentrated biomarkers in human body fluid like blood, the future works for this study would be focused on more tests of patient blood samples and further improvement on the tests reliability. It is challenging because the complicated compositions and the high salt concentration in human blood. These difficulties would lead to unsuccessful detection and diagnosis of BNP level in these samples. To reduce these effects from human blood, the sensor measuring parameters need to be optimized so that the sensor can be operated at the optimal conditions. Such as the further optimize the gate bias for the sensors to achieve long Debye length in the semiconductor, which can lead to very sensitive responses to the target and reduce the noise from non-specific targets. Furthermore, the tests in this work were done in a steady environment. It is of interest that to test

the sensor in a dynamic environment and monitor the response over time. Such tests can provide the kinetic information of the binding event, which can be utilized for the quantitation of BNP level. These investigations would finally lead to the development of biosensor system for patient to use it at home on a regular basis in future.

6.1 PUBLICATIONS

[1]. **Jiyong Huang**, Innam Lee, Xiliang Luo, Xinyan Tracy Cui, Minhee Yun, Bio-shielding Mask for Nanomaterial-Based Biosensor Incorporated with Microfluidic Device, ***Biomed. Microdevices*** 2013, 3, 531-537.

[2]. **Jiyong Huang**, Xiliang Luo, Innam Lee, Yushi Hu, Xinyan Tracy Cui, Minhee Yun, Rapid real-time electrical detection of proteins using single conducting polymer nanowire-based microfluidic aptasensor, ***Biosens. Bioelectron.*** 2011, 30, 306.

[3]. Xiliang Luo, Innam Lee, **Jiyong Huang**, Minhee Yun, Xinyan Tracy Cui, Ultrasensitive protein detection using an aptamer-functionalized single polyaniline nanowire, ***Chem. Commun.*** 2011, 47, 6368.

[4]. Innam Lee, Xiliang Luo, **Jiyong Huang**, Xinyan Tracy Cui, Minhee Yun, Detection of Cardiac Biomarkers Using Single Polyaniline Nanowire-Based Conductometric Biosensors, ***Biosensors*** 2012, 2, 205.

[5]. Yushi Hu, **Jiyong Huang**, Innam Lee, Xiliang Luo, Xinyan Tracy Cui, and Minhee Yun, Single Metal and Conducting Polymer Nanowires Used as Chemical/Biomolecular Sensors, Proceedings of 10th IEEE International Conference on Nanotechnology Joint Symposium with Nano Korea 2010, pp 708-711, 2010.

[6]. **Jiyong Huang,** Minhee Yun, Patterned Fabrication of Highly Uniform Polyaniline Nanowires, *In Preparation.*

[7]. **Jiyong Huang,** Minhee Yun, 2D Polyaniline Nanobelts Filed-effect Transistors for Ultrasensitive Detection of Cardiac Marker, *In Preparation.*

BIBLIOGRAPHY

[1]. Thevenot, D. R.; Toth, K.; Durst, R. A., et al., Electrochemical biosensors: recommended definitions and classification, Biosens. Bioelectron., **2001**, 16, 121.

[2]. Liu, J. W.; Cao, Z. H.; Lu, Y., Functional Nucleic Acid Sensors, Chem. Rev., **2009**, 109, 1948.

[3]. Rosi, N. L.; Mirkin, C. A., Nanostructures in biodiagnostics, Chem. Rev., **2005**, 105, 1547.

[4]. Kong, J.; Franklin, N. R.; Zhou, C. W., et al., Nanotube molecular wires as chemical sensors, Science, **2000**, 287, 622.

[5]. Star, A.; Tu, E.; Niemann, J., et al., Label-free detection of DNA hybridization using carbon nanotube network field-effect transistors, Proc. Natl. Acad. Sci. U. S. A., **2006**, 103, 921.

[6]. Mulvaney, S. P., BIOSENSORS Magnets tackle kinetic questions, Nat. Nanotechnol., **2011**, 6, 266.

[7]. Endo, T.; Kerman, K.; Nagatani, N., et al., Multiple label-free detection of antigen-antibody reaction using localized surface plasmon resonance-based core-shell structured nanoparticle layer nanochip, Anal. Chem., **2006**, 78, 6465.

[8]. Anker, J. N.; Hall, W. P.; Lyandres, O., et al., Biosensing with plasmonic nanosensors, Nat. Mater., **2008**, 7, 442.

[9]. Cheng, M. M. C.; Cuda, G.; Bunimovich, Y. L., et al., Nanotechnologies for biomolecular detection and medical diagnostics, Curr. Opin. Chem. Biol., **2006**, 10, 11.

[10]. LaHaye, M. D.; Buu, O.; Camarota, B., et al., Approaching the quantum limit of a nanomechanical resonator, Science, **2004**, 304, 74.

[11]. Cai, D.; Ren, L.; Zhao, H. Z., et al., A molecular-imprint nanosensor for ultrasensitive detection of proteins, Nat. Nanotechnol., **2010**, 5, 597.

[12]. Stern, E.; Vacic, A.; Rajan, N. K., et al., Label-free biomarker detection from whole blood, Nat. Nanotechnol., **2010**, 5, 138.

[13]. Forzani, E. S.; Zhang, H. Q.; Nagahara, L. A., et al., A conducting polymer nanojunction sensor for glucose detection, Nano Lett., **2004**, 4, 1785.

[14]. Ramanathan, K.; Bangar, M. A.; Yun, M., et al., Bioaffinity sensing using biologically functionalized conducting-polymer nanowire, J. Am. Chem. Soc., **2005**, 127, 496.

[15]. Bangar, M. A.; Shirale, D. J.; Chen, W., et al., Single Conducting Polymer Nanowire Chemiresistive Label-Free Immunosensor for Cancer Biomarker, Anal. Chem., **2009**, 81, 2168.

[16]. Hernandez, R. M.; Richter, L.; Semancik, S., et al., Template fabrication of protein-functionalized gold-polypyrrole-gold segmented nanowires, Chem. Mat., **2004**, 16, 3431.

[17]. Martin, C. R., Nanomaterials - A menbrane-based synthetic appraoch, Science, **1994**, 266, 1961.

[18]. Li, J.; Lin, X. Q., Glucose biosensor based on immobilization of glucose oxidase in poly(o-aminophenol) film on polypyrrole-Pt nanocomposite modified glassy carbon electrode, Biosens. Bioelectron., **2007**, 22, 2898.

[19]. Huang, L. M.; Wang, Z. B.; Wang, H. T., et al., Polyaniline nanowires by electropolymerization from liquid crystalline phases, J. Mater. Chem., **2002**, 12, 388.

[20]. Haeberle, S.; Zengerle, R., Microfluidic platforms for lab-on-a-chip applications, Lab Chip, **2007**, 7, 1094.

[21]. Choi, S.; Chae, J., A regenerative biosensing surface in microfluidics using electrochemical desorption of short-chain self-assembled monolayer, Microfluid. Nanofluid., **2009**, 7, 819.

[22]. Etzioni, R.; Urban, N.; Ramsey, S., et al., The case for early detection, Nat. Rev. Cancer, **2003**, 3, 243.

[23]. Willets, K. A.; Van Duyne, R. P., Localized surface plasmon resonance spectroscopy and sensing. In Annual Review of Physical Chemistry, Annual Reviews: Palo Alto, 2007, 58, 267.

[24]. Nie, S. M.; Emery, S. R., Probing single molecules and single nanoparticles by surface-enhanced Raman scattering, Science, **1997**, 275, 1102.

[25]. Qian, X. M.; Nie, S. M., Single-molecule and single-nanoparticle SERS: from fundamental mechanisms to biomedical applications, Chem. Soc. Rev., **2008**, 37, 912.

[26]. Qian, X. M.; Peng, X. H.; Ansari, D. O., et al., In vivo tumor targeting and spectroscopic detection with surface-enhanced Raman nanoparticle tags, Nat. Biotechnol., **2008**, 26, 83.

[27]. Yang, Y. T.; Callegari, C.; Feng, X. L., et al., Zeptogram-scale nanomechanical mass sensing, Nano Lett., **2006**, 6, 583.

[28]. Burg, T. P.; Godin, M.; Knudsen, S. M., et al., Weighing of biomolecules, single cells and single nanoparticles in fluid, Nature, **2007**, 446, 1066.

[29]. Elfstrom, N.; Karlstrom, A. E.; Linnrost, J., Silicon nanoribbons for electrical detection of biomolecules, Nano Lett., **2008**, 8, 945.

[30]. Cui, Y.; Wei, Q. Q.; Park, H. K., et al., Nanowire nanosensors for highly sensitive and selective detection of biological and chemical species, Science, **2001**, 293, 1289.

[31]. Patolsky, F.; Zheng, G. F.; Hayden, O., et al., Electrical detection of single viruses, Proc. Natl. Acad. Sci. U. S. A., **2004**, 101, 14017.

[32]. Zheng, G. F.; Patolsky, F.; Cui, Y., et al., Multiplexed electrical detection of cancer markers with nanowire sensor arrays, Nat. Biotechnol., **2005**, 23, 1294.

[33]. Whitesides, G. M.; Ostuni, E.; Takayama, S., et al., Soft lithography in biology and biochemistry, Annu. Rev. Biomed. Eng., **2001**, 3, 335.

[34]. Guo, L. J., Nanoimprint lithography: Methods and material requirements, Adv. Mater., **2007**, 19, 495.

[35]. Chou, S. Y.; Krauss, P. R.; Renstrom, P. J., Imprint of sub-25 nm vias and trenches in polymers, Appl. Phys. Lett., **1995**, 67, 3114.

[36]. Gates, B. D.; Xu, Q. B.; Stewart, M., et al., New approaches to nanofabrication: Molding, printing, and other techniques, Chem. Rev., **2005**, 105, 1171.

[37]. Ruiz, S. A.; Chen, C. S., Microcontact printing: A tool to pattern, Soft Matter, **2007**, 3, 168.

[38]. Shir, D. J.; Jeon, S.; Liao, H., et al., Three-dimensional nanofabrication with elastomeric phase masks, J. Phys. Chem. B, **2007**, 111, 12945.

[39]. Stewart, M. D.; Johnson, S. C.; Sreenivasan, S. V., et al., Nanofabrication with step and flash imprint lithography, J. Microlithogr. Microfabr. Microsyst., **2005**, 4, 6.

[40]. Heath, J. R., Superlattice Nanowire Pattern Transfer (SNAP), Accounts Chem. Res., **2008**, 41, 1609.

[41]. Xu, Q. B.; Rioux, R. M.; Dickey, M. D., et al., Nanoskiving: A New Method To Produce Arrays of Nanostructures, Accounts Chem. Res., **2008**, 41, 1566.

[42]. Xia, Y. N.; Whitesides, G. M., Soft lithography, Angew. Chem.-Int. Edit., **1998**, 37, 551.

[43]. Richter, K., Cutting artifacts on ultrathin cryosections of biological bulk speciments, Micron, **1994**, 25, 297.

[44]. Menke, E. J.; Thompson, M. A.; Xiang, C., et al., Lithographically patterned nanowire electrodeposition, Nat. Mater., **2006**, 5, 914.

[45]. Xiang, C. X.; Kung, S. C.; Taggart, D. K., et al., Lithographically patterned nanowire electrodeposition: A method for patterning electrically continuous metal nanowires on dielectrics, ACS Nano, **2008**, 2, 1939.

[46]. Park, S.; Lee, D. H.; Xu, J., et al., Macroscopic 10-Terabit-per-Square- Inch Arrays from Block Copolymers with Lateral Order, Science, **2009**, 323, 1030.

[47]. Park, M. H.; Duan, X. X.; Ofir, Y., et al., Chemically Directed Immobilization of Nanoparticles onto Gold Substrates for Orthogonal Assembly Using Dithiocarbamate Bond Formation, ACS Appl. Mater. Interfaces, **2010**, 2, 795.

[48]. Welander, A. M.; Kang, H. M.; Stuen, K. O., et al., Rapid directed assembly of block copolymer films at elevated temperatures, Macromolecules, **2008**, 41, 2759.

[49]. Jung, Y. S.; Chang, J. B.; Verploegen, E., et al., A Path to Ultranarrow Patterns Using Self-Assembled Lithography, Nano Lett., **2010**, 10, 1000.

[50]. Knoll, A.; Magerle, R.; Krausch, G., Phase behavior in thin films of cylinder-forming ABA block copolymers: Experiments, J. Chem. Phys., **2004**, 120, 1105.

[51]. Wu, N. L. Y.; Zhang, X. J.; Murphy, J. N., et al., Density Doubling of Block Copolymer Templated Features, Nano Lett., **2012**, 12, 264.

[52]. Yun, M. H.; Myung, N. V.; Vasquez, R. P., et al., Electrochemically grown wires for individually addressable sensor arrays, Nano Lett., **2004**, 4, 419.

[53]. Hu, Y.; To, A. C.; Yun, M., The controlled growth of single metallic and conducting polymer nanowires via gate-assisted electrochemical deposition, Nanotechnology, **2009**, 20, 8.

[54]. Clark, L. C.; Lyons, C., Electrode systems for continuous monitoring in cardiovascular surgery, Ann.NY Acad.Sci., **1962**, 102, 29.

[55]. Shirakawa, H.; Louis, E. J.; Macdiarmid, A. G., et al., Synthesis of electrically conducting organic polymer - halogen derivatives of polyacetylene, (CH)X, J. Chem. Soc.-Chem. Commun., **1977**, 578.

[56]. Cosnier, S., Affinity biosensors based on electropolymerized films, Electroanalysis, **2005**, 17, 1701.

[57]. Sree, U.; Yamamoto, Y.; Deore, B., et al., Characterisation of polypyrrole nano-films for membrane-based sensors, Synth. Met., **2002**, 131, 161.

[58]. Guimard, N. K.; Gomez, N.; Schmidt, C. E., Conducting polymers in biomedical engineering, Prog. Polym. Sci., **2007**, 32, 876.

[59]. Bakker, E.; Telting-Diaz, M., Electrochemical sensors, Anal. Chem., **2002**, 74, 2781.

[60]. Lange, U.; Roznyatouskaya, N. V.; Mirsky, V. M., Conducting polymers in chemical sensors and arrays, Anal. Chim. Acta, **2008**, 614, 1.

[61]. Ekanayake, E.; Preethichandra, D. M. G.; Kaneto, K., Polypyrrole nanotube array sensor for enhanced adsorption of glucose oxidase in glucose biosensors, Biosens. Bioelectron., **2007**, 23, 107.

[62]. Liu, C., Recent developments in polymer MEMS, Adv. Mater., **2007**, 19, 3783.

[63]. Trojanowicz, M., Application of conducting polymers in chemical analysis, Microchim. Acta, **2003**, 143, 75.

[64]. Rajesh; Ahuja, T.; Kumar, D., Recent progress in the development of nano-structured conducting polymers/nanocomposites for sensor applications, Sens. Actuator B-Chem., **2009**, 136, 275.

[65]. Luong, J. H. T.; Male, K. B.; Glennon, J. D., Biosensor technology: Technology push versus market pull, Biotechnol. Adv., **2008**, 26, 492.

[66]. Schasfoort, R. B. M., Proteomics-on-a-chip: the challenge to couple lab-on-a-chip unit operations, Expert Rev. Proteomics, **2004**, 1, 123.

[67]. Teles, F. R. R.; Fonseca, L. R., Trends in DNA biosensors, Talanta, **2008**, 77, 606.

[68]. Wang, J., Electrochemical biosensors: Towards point-of-care cancer diagnostics, Biosens. Bioelectron., **2006**, 21, 1887.

[69]. Aran, K.; Fok, A.; Sasso, L. A., et al., Microfiltration platform for continuous blood plasma protein extraction from whole blood during cardiac surgery, Lab Chip, **2011**, 11, 2858.

[70]. Dimov, I. K.; Basabe-Desmonts, L.; Garcia-Cordero, J. L., et al., Stand-alone self-powered integrated microfluidic blood analysis system (SIMBAS), Lab Chip, **2011**, 11, 845.

[71]. Haeberle, S.; Brenner, T.; Zengerle, R., et al., Centrifugal extraction of plasma from whole blood on a rotating disk, Lab Chip, **2006**, 6, 776.

[72]. Yang, S.; Undar, A.; Zahn, J. D., A microfluidic device for continuous, real time blood plasma separation, Lab Chip, **2006**, 6, 871.

[73]. Matsuura, H.; Sato, Y.; Niwa, O., et al., Electrochemical enzyme immunoassay of a peptide hormone at picomolar levels, Anal. Chem., **2005**, 77, 4235.

[74]. Kurita, R.; Yokota, Y.; Sato, Y., et al., On-chip enzyme immunoassay of a cardiac marker using a microfluidic device combined with a portable surface plasmon resonance system, Anal. Chem., **2006**, 78, 5525.

[75]. Mizutani, F., Biosensors utilizing monolayers on electrode surfaces, Sens. Actuator B-Chem., **2008**, 130, 14.

[76]. Prasad, S.; Selvam, A. P.; Reddy, R. K., et al., Silicon Nanosensor for Diagnosis of Cardiovascular Proteomic Markers, Jala, **2012**, 18, 143.

[77]. Yoon, H.; Lee, S. H.; Kwon, O. S., et al., Polypyrrole Nanotubes Conjugated with Human Olfactory Receptors: High-Performance Transducers for FET-Type Bioelectronic Noses, Angew. Chem.-Int. Edit., **2009**, 48, 2755.

[78]. Wang, W. U.; Chen, C.; Lin, K. H., et al., Label-free detection of small-molecule-protein interactions by using nanowire nanosensors, Proc. Natl. Acad. Sci. U. S. A., **2005**, 102, 3208.

[79]. Lee, H. S.; Kim, K. S.; Kim, C. J., et al., Electrical detection of VEGFs for cancer diagnoses using anti-vascular endotherial growth factor aptamer-modified Si nanowire FETs, Biosens. Bioelectron., **2009**, 24, 1801.

[80]. Chen, R. J.; Bangsaruntip, S.; Drouvalakis, K. A., et al., Noncovalent functionalization of carbon nanotubes for highly specific electronic biosensors, Proc. Natl. Acad. Sci. U. S. A., **2003**, 100, 4984.

[81]. Star, A.; Gabriel, J. C. P.; Bradley, K., et al., Electronic detection of specific protein binding using nanotube FET devices, Nano Lett., **2003**, 3, 459.

[82]. So, H. M.; Won, K.; Kim, Y. H., et al., Single-walled carbon nanotube biosensors using aptamers as molecular recognition elements, J. Am. Chem. Soc., **2005**, 127, 11906.

[83]. Kwakye, S.; Baeumner, A., A microfluidic biosensor based on nucleic acid sequence recognition, Anal. Bioanal. Chem., **2003**, 376, 1062.

[84]. Zaytseva, N. V.; Goral, V. N.; Montagna, R. A., et al., Development of a microfluidic biosensor module for pathogen detection, Lab. Chip., **2005**, 5, 805.

[85]. McDonald, J. C.; Chabinyc, M. L.; Metallo, S. J., et al., Prototyping of Microfluidic Devices Using Solid-Object Printing, Anal. Chem., **2002**, 74, 1537.

[86]. Li, C.; Curreli, M.; Lin, H., et al., Complementary detection of prostate-specific antigen using ln(2)O(3) nanowires and carbon nanotubes, J. Am. Chem. Soc., **2005**, 127, 12484.

[87]. Huang, N. P.; Voros, J.; De Paul, S. M., et al., Biotin-derivatized poly(L-lysine)-g-poly(ethylene glycol): A novel polymeric interface for bioaffinity sensing, Langmuir, **2002**, 18, 220.

[88]. Hermann, T.; Patel, D. J., Biochemistry - Adaptive recognition by nucleic acid aptamers, Science, **2000**, 287, 820.

[89]. Liao, W.; Randall, B. A.; Alba, N. A., et al., Conducting polymer-based impedimetric aptamer biosensor for in situ detection, Anal. Bioanal. Chem., **2008**, 392, 861.

[90]. Maeshima, A.; Miyagi, A.; Hirai, T., et al., Mucin-producing adenocarcinoma of the lung, with special reference to goblet cell type adenocarcinoma: Immunohistochemical observation and Ki-ras gene mutation, Pathol. Int., **1997**, 47, 454.

[91]. Zhang, S. L.; Zhang, H. S.; Reuter, V. E., et al., Expression of potential target antigens for immunotherapy on primary and metastatic prostate cancers, Clin. Cancer Res., **1998**, 4, 295.

[92]. Perey, L.; Hayes, D. F.; Maimonis, P., et al., Tumor selective reactivity of a monoclonal-antibody prepared against a recombinant peptide derived from the DF3 human breast caarcinoma-associated antigen, Cancer Res., **1992**, 52, 2563.

[93]. Hough, C. D.; Sherman-Baust, C. A.; Pizer, E. S., et al., Large-scale serial analysis of gene expression reveals genes differentially expressed in ovarian cancer, Cancer Res., **2000**, 60, 6281.

[94]. Croce, M. V.; Isla-Larrain, M. T.; Demichelis, S. O., et al., Tissue and serum MUC1 mucin detection in breast cancer patients, Breast Cancer Res. Treat., **2003**, 81, 195.

[95]. McDonald, J. C.; Whitesides, G. M., Poly(dimethylsiloxane) as a material for fabricating microfluidic devices, Accounts Chem. Res., **2002**, 35, 491.

[96]. Kim, Y. H.; Kim, J. P.; Han, S. J., et al., Aptamer biosensor for lable-free detection of human immunoglobulin E based on surface plasmon resonance, Sens. Actuator B-Chem., **2009**, 139, 471.

[97]. Yao, C. Y.; Qi, Y. Z.; Zhao, Y. H., et al., Aptamer-based piezoelectric quartz crystal microbalance biosensor array for the quantification of IgE, Biosens. Bioelectron., **2009**, 24, 2499.

[98]. Cheng, A. K. H.; Su, H. P.; Wang, A., et al., Aptamer-Based Detection of Epithelial Tumor Marker Mucin 1 with Quantum Dot-Based Fluorescence Readout, Anal. Chem., **2009**, 81, 6130.

[99]. Liss, M.; Petersen, B.; Wolf, H., et al., An aptamer-based quartz crystal protein biosensor, Anal. Chem., **2002**, 74, 4488.

[100]. Liu, W. T.; Zhu, L.; Qin, Q. W., et al., Microfluidic device as a new platform for immunofluorescent detection of viruses, Lab Chip, **2005**, 5, 1327.

[101]. Soper, S. A.; Brown, K.; Ellington, A., et al., Point-of-care biosensor systems for cancer diagnostics/prognostics, Biosens. Bioelectron., **2006**, 21, 1932.

[102]. Bange, A.; Halsall, H. B.; Heineman, W. R., Microfluidic immunosensor systems, Biosens. Bioelectron., **2005**, 20, 2488.

[103]. Goral, V. N.; Zaytseva, N. V.; Baeumner, A. J., Electrochemical microfluidic biosensor for the detection of nucleic acid sequences, Lab Chip, **2006**, 6, 414.

[104]. Zaytseva, N. V.; Goral, V. N.; Montagna, R. A., et al., Development of a microfluidic biosensor module for pathogen detection, Lab Chip, **2005**, 5, 805.

[105]. Liao, W. Y.; Weng, C. H.; Lee, G. B., et al., Development and characterization of an all-solid-state potentiometric biosensor array microfluidic device for multiple ion analysis, Lab Chip, **2006**, 6, 1362.

[106]. Pregibon, D. C.; Toner, M.; Doyle, P. S., Multifunctional encoded particles for high-throughput biomolecule analysis, Science, **2007**, 315, 1393.

[107]. Chan, E. Y.; Goncalves, N. M.; Haeusler, R. A., et al., DNA mapping using microfluidic stretching and single-molecule detection of fluorescent site-specific tags, Genome Res., **2004**, 14, 1137.

[108]. Psaltis, D.; Quake, S. R.; Yang, C. H., Developing optofluidic technology through the fusion of microfluidics and optics, Nature, **2006**, 442, 381.

[109]. Kanda, V.; Kariuki, J. K.; Harrison, D. J., et al., Label-free reading of microarray-based immunoassays with surface plasmon resonance imaging, Anal. Chem., **2004**, 76, 7257.

[110]. Gijs, M. A. M.; Lacharme, F.; Lehmann, U., Microfluidic Applications of Magnetic Particles for Biological Analysis and Catalysis, Chem. Rev., **2010**, 110, 1518.

[111]. Arora, A.; Simone, G.; Salieb-Beugelaar, G. B., et al., Latest Developments in Micro Total Analysis Systems, Anal. Chem., **2010**, 82, 4830.

[112]. Dittrich, P. S.; Tachikawa, K.; Manz, A., Micro total analysis systems. Latest advancements and trends, Anal. Chem., **2006**, 78, 3887.

[113]. Jo, B. H.; Van Lerberghe, L. M.; Motsegood, K. M., et al., Three-dimensional micro-channel fabrication in polydimethylsiloxane (PDMS) elastomer, J. Microelectromech. Syst., **2000**, 9, 76.

[114]. McDonald, J. C.; Duffy, D. C.; Anderson, J. R., et al., Fabrication of microfluidic systems in poly(dimethylsiloxane), Electrophoresis, **2000**, 21, 27.

[115]. Egger, S.; Ilie, A.; Fu, Y. T., et al., Dynamic shadow mask technique: A universal tool for nanoscience, Nano Letters, **2005**, 5, 15.

[116]. Luthi, R.; Schlittler, R. R.; Brugger, J., et al., Parallel nanodevice fabrication using a combination of shadow mask and scanning probe methods, Appl. Phys. Lett., **1999**, 75, 1314.

[117]. Zhao, Y.; Jiang, L., Hollow Micro/Nanomaterials with Multilevel Interior Structures, Adv. Mater., **2009**, 21, 3621.

[118]. Zang, L.; Che, Y. K.; Moore, J. S., One-Dimensional Self-Assembly of Planar pi-Conjugated Molecules: Adaptable Building Blocks for Organic Nanodevices, Accounts Chem. Res., **2008**, 41, 1596.

[119]. Lu, X. F.; Wang, C.; Wei, Y., One-Dimensional Composite Nanomaterials: Synthesis by Electrospinning and Their Applications, Small, **2009**, 5, 2349.

[120]. Yang, N. L.; Zhai, J.; Wang, D., et al., Two-Dimensional Graphene Bridges Enhanced Photoinduced Charge Transport in Dye-Sensitized Solar Cells, ACS Nano, **2010**, 4, 887.

[121]. Liu, X. H.; Zhang, J.; Wang, L. W., et al., 3D hierarchically porous ZnO structures and their functionalization by Au nanoparticles for gas sensors, J. Mater. Chem., **2011**, 21, 349.

[122]. Arico, A. S.; Bruce, P.; Scrosati, B., et al., Nanostructured materials for advanced energy conversion and storage devices, Nat. Mater., **2005**, 4, 366.

[123]. Biswas, C.; Lee, Y. H., Graphene Versus Carbon Nanotubes in Electronic Devices, Adv. Funct. Mater., **2011**, 21, 3806.

[124]. Yun, Y. H.; Dong, Z. Y.; Shanov, V., et al., Nanotube electrodes and biosensors, Nano Today, **2007**, 2, 30.

[125]. Chen, J. H.; Jang, C.; Xiao, S. D., et al., Intrinsic and extrinsic performance limits of graphene devices on SiO2, Nat. Nanotechnol., **2008**, 3, 206.

[126]. Pumera, M., Graphene in biosensing, Mater. Today, **2011**, 14, 308.

[127]. Chen, K. I.; Li, B. R.; Chen, Y. T., Silicon nanowire field-effect transistor-based biosensors for biomedical diagnosis and cellular recording investigation, Nano Today, **2011**, 6, 131.

[128]. Gao, X. P. A.; Zheng, G. F.; Lieber, C. M., Subthreshold Regime has the Optimal Sensitivity for Nanowire FET Biosensors, Nano Lett., **2010**, 10, 547.

[129]. Goncalves, D.; Prazeres, D. M. F.; Chu, V., et al., Detection of DNA and proteins using amorphous silicon ion-sensitive thin-film field effect transistors, Biosens. Bioelectron., **2008**, 24, 545.

[130]. Yeh, P. H.; Li, Z.; Wang, Z. L., Schottky-Gated Probe-Free ZnO Nanowire Biosensor, Adv. Mater., **2009**, 21, 4975.

[131]. Batra, N.; Tomar, M.; Gupta, V., Realization of an efficient cholesterol biosensor using ZnO nanostructured thin film, Analyst, **2012**, 137, 5854.

[132]. Das, M.; Sumana, G.; Nagarajan, R., et al., Application of nanostructured ZnO films for electrochemical DNA biosensor, Thin Solid Films, **2010**, 519, 1196.

[133]. Wang, C. W.; Pan, C. Y.; Wu, H. C., et al., In situ detection of chromogranin a released from living neurons with a single-walled carbon-nanotube field-effect transistor, Small, **2007**, 3, 1350.

[134]. Lo, Y. S.; Nam, D. H.; So, H. M., et al., Oriented Immobilization of Antibody Fragments on Ni-Decorated Single-Walled Carbon Nanotube Devices, ACS Nano, **2009**, 3, 3649.

[135]. Kang, X. H.; Wang, J.; Wu, H., et al., Glucose Oxidase-graphene-chitosan modified electrode for direct electrochemistry and glucose sensing, Biosens. Bioelectron., **2009**, 25, 901.

[136]. Dey, R. S.; Raj, C. R., Development of an Amperometric Cholesterol Biosensor Based on Graphene-Pt Nanoparticle Hybrid Material, J. Phys. Chem. C, **2010**, 114, 21427.

[137]. Bishnoi, S. W.; Lin, Y. J.; Tibudan, M., et al., SERS Biodetection Using Gold-Silica Nanoshells and Nitrocellulose Membranes, Anal. Chem., **2011**, 83, 4053.

[138]. Chang, H. X.; Yuan, Y.; Shi, N. L., et al., Electrochemical DNA biosensor based on conducting polyaniline nanotube array, Anal. Chem., **2007**, 79, 5111.

[139]. Fan, Y.; Chen, X. T.; Trigg, A. D., et al., Detection of microRNAs using target-guided formation of conducting polymer nanowires in nanogaps, J. Am. Chem. Soc., **2007**, 129, 5437.

[140]. Rahman, M. A.; Kwon, N. H.; Won, M. S., et al., Functionalized conducting polymer as an enzyme-immobilizing substrate: An amperometric glutamate microbiosensor for in vivo measurements, Anal. Chem., **2005**, 77, 4854.

[141]. Chiou, N. R.; Lui, C. M.; Guan, J. J., et al., Growth and alignment of polyaniline nanofibres with superhydrophobic, superhydrophilic and other properties, Nat. Nanotechnol., **2007**, 2, 354.

[142]. Xu, J. J.; Wang, K.; Zu, S. Z., et al., Hierarchical Nanocomposites of Polyaniline Nanowire Arrays on Graphene Oxide Sheets with Synergistic Effect for Energy Storage, ACS Nano, **2010**, 4, 5019.

[143]. Liang, L.; Liu, J.; Windisch, C. F., et al., Direct assembly of large arrays of oriented conducting polymer nanowires, Angew. Chem.-Int. Edit., **2002**, 41, 3665.

[144]. Liu, J.; Lin, Y. H.; Liang, L., et al., Templateless assembly of molecularly aligned conductive polymer nanowires: A new approach for oriented nanostructures, Chem.-Eur. J., **2003**, 9, 605.

[145]. Huang, J. X.; Virji, S.; Weiller, B. H., et al., Polyaniline nanofibers: Facile synthesis and chemical sensors, J. Am. Chem. Soc., **2003**, 125, 314.

[146]. Zhang, X. Y.; Kolla, H. S.; Wang, X. H., et al., Fibrillar growth in polyaniline, Adv. Funct. Mater., **2006**, 16, 1145.

[147]. Wang, J.; Bunimovich, Y. L.; Sui, G. D., et al., Electrochemical fabrication of conducting polymer nanowires in an integrated microfluidic system, Chem. Commun., **2006**, 3075.

[148]. Alam, M. M.; Wang, J.; Guo, Y. Y., et al., Electrolyte-gated transistors based on conducting polymer nanowire junction arrays, J. Phys. Chem. B, **2005**, 109, 12777.

[149]. Lee, S. Y.; Choi, G. R.; Lim, H., et al., Electronic transport characteristics of electrolyte-gated conducting polyaniline nanowire field-effect transistors, Appl. Phys. Lett., **2009**, 95, 3.

[150]. Kim, W. J.; Kim, B. K.; Kim, A., et al., Response to Cardiac Markers in Human Serum Analyzed by Guided-Mode Resonance Biosensor, Anal. Chem., **2010**, 82, 9686.

[151]. Luo, X. L.; Lee, I.; Huang, J. Y., et al., Ultrasensitive protein detection using an aptamer-functionalized single polyaniline nanowire, Chem. Commun., **2011**, 47, 6368.

[152]. Ishikawa, F. N.; Chang, H. K.; Curreli, M., et al., Label-Free, Electrical Detection of the SARS Virus N-Protein with Nanowire Biosensors Utilizing Antibody Mimics as Capture Probes, ACS Nano, **2009**, 3, 1219.

[153]. Lee, J.; Choi, Y. S.; Lee, Y., et al., Sensitive and Simultaneous Detection of Cardiac Markers in Human Serum Using Surface Acoustic Wave Immunosensor, Anal. Chem., **2011**, 83, 8629.

[154]. Dao, Q.; Krishnaswamy, P.; Kazanegra, R., et al., Utility of B-type natriuretic peptide in the diagnosis of congestive heart failure in an urgent-care setting, J. Am. Coll. Cardiol., **2001**, 37, 379.

[155]. Stern, E.; Klemic, J. F.; Routenberg, D. A., et al., Label-free immunodetection with CMOS-compatible semiconducting nanowires, Nature, **2007**, 445, 519.

[156]. Vacic, A.; Criscione, J. M.; Rajan, N. K., et al., Determination of Molecular Configuration by Debye Length Modulation, J. Am. Chem. Soc., **2011**, 133, 13886.

[157]. Sorgenfrei, S.; Chiu, C. Y.; Johnston, M., et al., Debye Screening in Single-Molecule Carbon Nanotube Field-Effect Sensors, Nano Lett., **2011**, 11, 3739.

[158]. Gundry, R. L.; Van Eyk, J. E., Unraveling the complexity of circulating forms of brain natriuretic peptide, Clin. Chem., **2007**, 53, 1181.